

How does stellar convection impact the detection of small planets at high radial velocity precision?

Dissertation
for the award of the degree
“Doctor rerum naturalium”
of the Georg-August-Universität Göttingen

within the doctoral program PROPHYS
of the Georg-August University School of Science (GAUSS)

submitted by
Florian Liebing
from Seesen

Göttingen, 2022

Thesis Committee

Prof. Dr. Ansgar Reiners, Institut für Astrophysik, Georg-August-Universität Göttingen, Germany

Until November 2020: Dr. Sandra Jeffers, Solar and Stellar Interiors, Max-Planck-Institute for Solar System Research, Göttingen, Germany

From November 2020: Dr. Mathias Zechmeister, Institut für Astrophysik, Georg-August-Universität Göttingen, Germany

Prof. Dr. Stefan Dreizler, Institut für Astrophysik, Georg-August-Universität Göttingen, Germany

Members of the Examination Board

Reviewer: Prof. Dr. Ansgar Reiners
Institut für Astrophysik, Georg-August-Universität Göttingen, Germany

Second Reviewer: Prof. Dr. Stefan Dreizler
Institut für Astrophysik, Georg-August-Universität Göttingen, Germany

Further members of the Examination Board:

Prof. Dr. Laurent Gizon
Department Solar and Stellar Interiors, Max-Planck-Institute for Solar System Research, Göttingen, Germany

Prof. Dr. Saskia Hekker
Group Theory and Observations of Stars, Heidelberg Institute for Theoretical Studies, Heidelberg, Germany

Prof. Dr. Laura Covi
Institute for theoretical Physics, Georg-August-Universität Göttingen, Germany

Prof. Dr. Andreas Tilgner
Institute of Geophysics, Georg-August-Universität Göttingen, Germany

Date of the oral examination: May 11, 2022

Abstract

One of the big driving forces behind exoplanet research is the search for an Earth-twin to answer the old question of whether or not humanity is alone in the universe. According to simple logic as well as our current understanding of planet formation, planet Earth should have a twin somewhere within a few hundred lightyears. A planet of similar mass, composed primarily of rock and orbiting within the habitable zone around a star similar in age and temperature to our Sun. Yet, after nearly three decades of active searches for planets around other stars, we have not managed to find one. For the first twenty years this was expected as Earth is a rather small planet compared to even the giants in our Solar System, while our Sun is well above average in terms of stellar mass, leading to only a very weak signal and requiring an instrumental precision far in excess of what was available at the time. Over the last decade, instrumentation has reached the point where detecting an Earth twin would become possible, if it was not for variable signals intrinsic to the stars themselves that can hide and even mimic the signals of small exoplanets. Overcoming the challenge of these variable stellar signals by finding ways to mitigate their effects on, and disentangle them from, observations is a major part of contemporary exoplanet research. To this end, three main contributions to stellar variability and their interplay were investigated: (i) Acoustic oscillations of the entire star, excited by turbulent motion. (ii) Starspots and rotationally modulated phenomena related to magnetically active regions. (iii) Convective blueshift, its suppression through magnetic activity, and how it can be robustly determined. The scaling of acoustic oscillations with stellar mass along the main sequence and with age along the red giant phase were explored as well as how mitigating oscillatory radial velocity variations through well chosen integration times could be possible. Starspot covering maps for a range of stellar effective temperatures and activity levels were created and its effect through rotation on observed line profiles and radial velocities simulated. An empirical, data-driven, model-independent way to determine convective blueshift strengths was developed and its efficacy analyzed. The basis is an ultra-high quality solar template that was created and limits for the applicability of the technique in signal-to-noise, instrumental resolution and stellar rotation were determined. The technique was applied to determine convective blueshift strengths along the main sequence for 810 stars between 3500 K and 6200 K and for 241 post-main sequence stars spanning from subgiant to asymptotic giant stars. A strict scaling relation of convective blueshift along the main sequence to the third power of the effective temperature was found together with a plateau for K-type dwarfs. M dwarfs showed no discernible convective shift. Post-main sequence stars show stronger convective shifts compared to main sequence stars of similar temperature but vary a lot less overall with increasing age. A small minimum was found for the earliest red giants, just after the subgiant transition, while convective

blueshift strengths determined in this way were found to increasingly decouple past that point from expectations from analytical models, macroturbulent dispersion and 3D MHD derived velocities, likely due to changes in the large-scale convective structure.

Contents

1. Introduction	1
1.1. Extrasolar planets	3
1.2. Methods of exoplanet detection	5
1.2.1. Transit Method	8
1.2.2. Radial Velocity	11
1.3. Problems of the current methods	15
1.4. Sources of stellar variability	16
1.4.1. Acoustic oscillations	18
1.4.2. Starspots and rotation	22
1.4.3. Convective motion and granulation	29
1.5. Measuring Convective Blueshift	32
2. [Paper] Convective blueshift strengths of 810 F to M solar-type stars	35
2.1. Abstract	39
2.2. Introduction	39
2.3. Convective line shift	41
2.3.1. Flux asymmetries from granulation	41
2.3.2. Impact on line shape	42
2.3.3. Blueshift measuring techniques	42
2.3.3.1. High-resolution techniques: Line bisectors	42
2.3.3.2. Low-resolution techniques: Third-signature scaling	43
2.4. Data	45
2.4.1. HARPS stellar data	45
2.4.2. IAG solar data	47
2.5. HARPS data processing	47
2.5.1. Boundary fit	47
2.5.2. Line selection	48
2.5.3. Telluric contamination	49
2.5.4. Initial radial velocity	49
2.5.5. Measuring line positions	50
2.5.6. Refining radial velocity	50
2.6. Modeling the solar third signature	51
2.7. Third-signature fit for the HARPS sample	53
2.7.1. F, G, and K stars	55
2.7.2. M stars	56

2.8.	Discussion	57
2.8.1.	Line list effective temperature selection	58
2.8.2.	Influence of stellar activity	58
2.8.3.	Influence of excitation potential	59
2.8.4.	Comparison to other works	60
2.8.5.	Extending the data set	62
2.9.	Conclusion	62
2.10.	Appendix	64
3.	[Paper] Convective Blueshift among evolved stars	77
3.1.	Abstract	81
3.2.	Introduction	81
3.3.	Data and processing	83
3.3.1.	Observations	84
3.3.2.	Data filtering	86
3.3.3.	Stellar evolution phase	86
3.4.	Technique	87
3.5.	Results	89
3.5.1.	Temperature dependence of post-MS CBS strengths	89
3.5.2.	Surface gravity dependence of post-MS CBS strengths	91
3.5.3.	Comparison with literature results	92
3.5.4.	Comparison with analytical models	93
3.5.5.	Relation to macroturbulence velocities	94
3.5.6.	Convection velocities from 3D MHD	96
3.6.	Summary and Conclusion	97
3.7.	Appendix	98
4.	Summary and Conclusion	105
4.1.	A solar template for stellar convection	105
4.2.	Convection along the main sequence	106
4.3.	Convection among evolved stars	108
4.4.	Using directly measured convective blueshift for activity mitigation	108
4.5.	Outlook	111
	Bibliography	113

List of Figures

1.1. Distribution of confirmed exoplanets	5
1.2. Theoretical transit lightcurve	8
1.3. Model light curves at different wavelengths	9
1.4. Illustration of the radial velocity method	11
1.5. Example RV curves	12
1.6. Solar oscillation model power spectrum and ZAMS amplitudes and frequencies	18
1.7. Oscillation parameters for red giants	20
1.8. Schematic formation of a starspot	22
1.9. Schematic illustration of rotational broadening	23
1.10. Effects of a rotating, equatorial starspot	24
1.11. Starspot maps for a range of filling factors from 10^{-4} to 1	25
1.12. Contributions of the flux and CBS suppression effects of a rotating starspot	27
1.13. Illustration of the formation of convective granules and intergranular lanes	29
1.14. Differences in energy transport for stars of different masses	30
1.15. CBS signature from a model and solar Fe 1 line profiles	32
1.16. Solar third signature of granulation	33
2.1. Comparison of a solar and a model spectral line bisector	44
2.2. HR diagram of the HARPS MS sample	45
2.3. S/N, temperature and spectral type overview for the HARPS MS sample	46
2.4. Third signature of granulation extracted from the IAG solar flux atlas	52
2.5. Third-signature plots from HARPS MS and broadened solar FTS data	54
2.6. Solar relative scale factors from the HARPS MS sample vs. temperature	55
2.7. Scale factors vs. temperature with color-coded $\log R'_{HK}$	58
2.8. Fit of the signed residuals of the scale factor fit and the activity indicator	59
2.9. Comparison to Meunier et al. (2017c) results	61
2.10. Initial line utilization; number of stars per line over wavelength	64
2.11. Initial line numbers; number of lines per star over T_{eff}	64
2.12. Percentile-based line list vetting	65
2.13. Remaining line utilization; number of stars per line over wavelength	66
2.14. Remaining line numbers; number of lines per star over T_{eff}	66
2.15. Distribution of line absorption depth with central wavelength	67
2.16. Two approaches to the wavelength dependence of CBS	68
2.17. Wavelength dependent third signature model	69
2.18. Accuracy of determined line centers	69

2.19. Accuracy of determined line depths	70
2.20. Comparing VALD and measured HARPS line depths	70
2.21. Effect of resolving power, R , on the determined solar scale factor	71
2.22. Effect of signal-to-noise ratio on the determined solar scale factor	71
2.23. Example for the continuum normalization	73
2.24. Third-signature scale vs. temperature, markers scaled with χ^2	73
3.1. HR diagram of HARPS MS and post-MS sample stars	84
3.2. S/N, temperature and evolution phase overview for the HARPS post-MS sample	85
3.3. Solar template third signature	88
3.4. Comparison of MS and post-MS third signatures	90
3.5. Scale factor vs. effective temperature for the HARPS post-MS stars	91
3.6. Scale factor vs. surface gravity for the HARPS post-MS stars	92
3.7. Comparison with analytical scaling relations	93
3.8. Comparison with macroturbulence dispersion	96
3.9. Comparison of horizontally averaged, peak vertical velocities	96
3.10. HR diagram of the PEPSI sample	99
3.11. Scale factor vs. temperature results for the PEPSI sample	99
3.12. Scale factor vs. effective temperature for the HARPS MS sample with alternate line list	100
3.13. Comparison with the Gray (2009) results	100

List of Tables

1.1. Confirmed exoplanet detections by method	5
2.1. Parameters used for the VALD extract stellar query	49
2.2. Coefficients for the $S(T_{\text{eff}})$ polynomial fit	56
2.3. Coefficients for the wavelength dependent, solar third-signature model . .	67
2.4. MS scale factor cheat sheet	74
2.5. List of all MS stars with their parameters	75
3.1. Post-MS scale factor cheat sheet	102
3.2. Partial list of the post-MS stars with their parameters	103

1. Introduction

"Can we cross that valley?". "What is behind that ocean?". "Where do we come from?". "Are we alone?". These, and many similar questions have been weighing on the mind of researchers and explorers of the past couple thousand years. At their core lies the overarching search for humanities, our, place in the world and the larger universe. A search for purpose that has been filled with setbacks, disappointments and an overall trend towards complexity and insignificance.

From Pythagoras' postulate in 600 BCE to Eratosthenes first measurements 300 BCE, humanity lost its place at the center of a flat world in favor of a finite, spherical planet where no spot is intrinsically more significant than any other. The re-discovery of already human inhabited continents behind the great oceans, first by Leif Erikson around 1000 CE and later by Christopher Columbus and Giovanni Caboto in the late 15th century as well as Ferdinand Magellan's first oceanic circumnavigation a few years later, firmly cemented that fact. Similarly, proposed as far back as the 5th century BCE by Philolaus and Hicetas, and formulated in the 16th century by Nicolaus Copernicus, the heliocentric model removed Earth from the center of the universe and placed it into an orbit around the Sun. The model was proven a century later mathematically by Johannes Kepler and observationally by Galileo Gallilei.

After loosing the certainty of spatial significance not just on our home planet but in the entire universe, the mid 19th century brought with it the Darwinian revolution. Named after Charles Darwin, though formulated nearly simultaneously by Alfred Russel Wallace and going back to ideas from pre-Socratic times from such as Anaximander and Empedocles, the newly coined Theory of Evolution eliminated the exceptionalism projected onto the human species. From the declared pinnacle of existence, homo sapiens became merely the most recent iteration of a billion year spanning, massively parallel running process of biological optimization guided by a fight where only the fittest may survive.

The early 20th century brought with it several revolutions in short succession. Ever since Galilei managed to observe in 1612 that the band of the Milky way could be resolved into uncountable numbers of individual stars it was commonly believed that our galaxy was all there is to the universe. Following the Great Debate in 1920, [Hubble \(1925\)](#) showed that the Milky way did not contain all stars in the universe after all, by determining the distance to the Andromeda galaxy (M31) and finding it far in excess of what was believed possible at the time. Instead, the Milky way was discovered to be just one of many galaxies filling the universe, each consisting of billions of stars. All the previously believed "spiral nebulae" suddenly became mirrors of our own galaxy leading to the obvious question: Do they

also contain mirrors of our Sun? Our Solar System? Earth? Or is at least the Milky Way in some way special? The latter was disproven quickly, when [Hubble \(1929\)](#) discovered his famous law, linking a galaxies distance with its recession velocity. This discovery confirmed derivations by [Friedmann \(1922\)](#) and [Lemaître \(1927\)](#), based on Einsteins newly formulated General Theory of relativity ([Einstein 1915](#)), of an expanding universe which predicted isotropic recession of distant objects with a velocity proportional to that distance. This cosmological expansion, when inverted and traced back in time, gave rise to the Big Bang theory on the origin of the universe. The theory was originally heavily contested as it was seen as "reintroducing concepts of creationism into science", and only gained traction after the discovery of the predicted cosmic microwave background by [Penzias & Wilson \(1965\)](#), the "afterglow of the Big bang".

At this point it had become clear that neither humanity, our Sun or even our entire galaxy was in any way special beyond a long chain of lucky happenstances. The only two questions remaining unanswered during the middle of the 20th century were: Do other stars also feature systems of planets like our Sun? And if they do, are any of them habitable, bearing life like ours, pondering the big question if at least their existence makes them the exception from the rule. Or if maybe even that is nothing unusual in the grand scheme. It took another three decades to find the beginnings of an answer to the first part when, in 1992, the first extrasolar planet was confirmed to have been discovered ([Wolszczan & Frail 1992](#)).

1.1. Extrasolar planets

The Copernican principle dictates that, in the absence of evidence to the contrary, humans are not privileged in their observations. Therefore our Solar System, as it is observed by humans, should be representative of other stellar systems, otherwise we would be privileged in our location. Before the discovery of the first extrasolar planets (exoplanets), it was therefore assumed that not only should other stars host a plethora of planets, their structure should also resemble what was known for the bodies of the Solar System. It was thought that close to the star, where volatiles are scarce from the higher temperature and radiation pressure, only small, rocky planets would be able to form. These would be equivalents to Mercury, Venus, Earth itself and Mars. Further out, lower temperatures allow for the existence of more volatile compounds expected to facilitate the rapid formation of rocky cores. Lower radiation pressure and the increased surface area of the orbital annulus should give rise to run-away gas accretion and the formation of the gas giants of our Solar System, Jupiter and Saturn. Beyond the snow-line, the radial distance where temperatures are low enough so ices of water, ammonia and other volatiles can re-sublime, ice giants would be expected following the templates of Uranus and Neptune. The logic was considered sound, the formation history thought to be understood. What was missing was data on actual exoplanets.

The first confirmed detection of exoplanets was by [Wolszczan & Frail \(1992\)](#) around the star PSR B1257+12, later named Lich. The companions PSR B1257+12 c and d (now called Poltergeist and Phobos) are super-Earth mass planets with 4.3 and 3.9 M_{\oplus} (Earth masses) respectively and their discovery was a surprise in multiple ways. For one, our Solar System does not contain an equivalent for planets of these masses, the closest being Earth itself and Uranus at 14.5 M_{\oplus} . Secondly, PSR B1257+12 is a pulsar, a rapidly spinning neutron star with an off-axis pointing magnetic field that channels radiation into a tight beam that periodically sweeps over a circular region of the sky. It was the timing of these sweeps, the observed, name-giving pulses, that showed periodic anomalies which could only be explained by the presence of orbiting bodies. The gravity of these bodies caused the star to move back and forth by a small amount, causing the pulses to be delayed by the increased light travel time. The enormous precision of the pulses, on the order of modern atomic clocks, allowed for these tiny variations to be measured and the planets orbital solutions to be recovered. Unfortunately, this discovery was as far from the prediction of the Copernican principle as you could get with a dead star that, along with its companions, was much heavier than anything found in our own Solar System.

It took another three years for the first exoplanet around a main-sequence star, one that is still in the main phase of its life and burning Hydrogen in its core like our Sun, to be discovered by [Mayor & Queloz \(1995\)](#). 51 Pegasi b orbits a host that is only 11% heavier than our Sun, giving it a slightly earlier spectral type and higher temperature and weighs around 0.5 Jupiter masses. While still without a Solar System equivalent for that weight, the bigger problem was that this planet went to become the archetype for the class of

hot-Jupiter planets. This class counts gas giant planets that, unlike the giants from our Solar System, don't orbit at intermediate distances, but rather very close to their host well inside the boundary at which their formation was considered impossible.

At this point, the Copernican principle appeared very much questionable and has not recovered since. Not only have planetary systems resembling ours yet to be found, as have Earth-like planets in general, it also appears that the planets of our Solar System are very much not representative for the "planetary zoo" (see also Figure [1.1](#)) with hot-Jupiters and mini-Neptunes making up a significant portion of discoveries without existing in our Solar System. Whether this is wholly due to biases in the employed detection methods (Section [1.2](#)) or a real breach of the Copernican principle has, in the absence of true Earth-twin detections, remained unsolved.

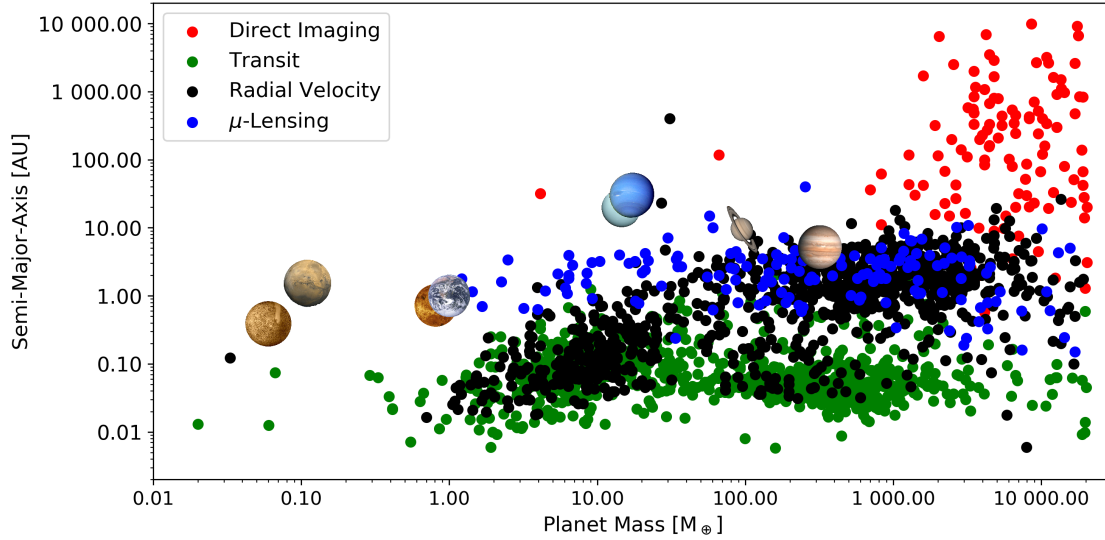


Figure 1.1.: Distribution of confirmed exoplanets, color coded for the detection method, with the planets of the Solar System indicated¹. Each method shows a distinct region where it is most sensitive in terms of planetary mass and orbital distance. In the case of the RV method, the projected mass $M \sin i$ is shown. Not all detections of the respective methods can be shown due to unknown parameters.²

1.2. Methods of exoplanet detection

Over the decades a large number of methods to detect exoplanets have been developed and used to varying grades of success. The pulsar timing variation method used to detect the first exoplanets was employed several more times and expanded to utilize other periodicities, such as stellar pulsations and eclipsing binaries. The most successful techniques however were the transit method, well known from the Kepler and TESS space missions, the radial velocity (RV) method, gravitational micro-lensing (μ -lensing), and direct imaging. The first two methods, as they are by far the most successful and synergistic, are explained in detail in Sections 1.2.1 and 1.2.2.

Method	Detections ²
Timing	45
Transit	3484
Radial Velocity	987
μ -Lensing	167
Direct Imaging	162
All	4912

Table 1.1.: Numbers of confirmed exoplanet detections for the most common methods.

The gravitational microlensing technique takes advantage of the prediction from Einsteins theory of general relativity (GR) that a massive object, though its gravity, can bend and focus light similar to a lens. Perhaps better known from observations by the Hubble space telescope of galactic clusters, where the lensing strength

¹Images of the 8 planets are from the public domain, downloaded from https://de.wikipedia.org/wiki/Liste_der_Planeten_des_Sonnensystems, Jan. 31st, 2022

²Data taken from exoplanet.eu; Jan. 12th, 2022

was used to infer the presence of dark matter, the effect is also observable on a stellar scale, such as the original proof of GR during a solar eclipse, where the solar gravity made stars appear next to the eclipse that should be located behind the solar disk under Newtonian physics. Planetary lenses, especially in other stellar systems however, are too weak to be detectable on their own. Instead, under the right geometry, they can interact with the lensing properties of their host to form a caustic. At these moments, the magnification of the combined lens far exceeds the individual components. If the lensing system happens to pass in front of another star, as viewed from the observer, the background stars apparent brightness will spike strongly in a way that can be modeled and inverted to recover the properties of the lensing system, especially the planets.

The final common technique is aptly called direct imaging and corresponds to a variety of ways that utilize telescopic observations to obtain actual image data of exoplanets, rather than indirectly inferring their presence. The multitude of techniques falling under the terminology of direct imaging is a result of the necessity to compensate for the very low brightness of planets in comparison to their host while somehow avoiding the host stars brightness to outshine and hide their companions. This is usually done by employing a coronagraph that blocks the light from the star, similar to how the moon blocks the Sun during an eclipse, and combining multiple exposures to increase the planetary signal. At longer wavelengths, interferometry is also very commonly employed to increase the angular resolution of the combined observation.

Each of the methods has its own strong points, areas where it is especially sensitive, and synergies with other methods where individual downsides can be compensated. The most prominent example for this being the RV and transit techniques that are explored in more detail in the following sections. Figure 1.1 shows the currently confirmed exoplanets with known semi-major axis and mass to illustrate the characteristics of each method.

Direct imaging, to no surprise, favors planets at large separations that makes distinguishing them from the stellar glare easier, and with a very high mass. The correspondingly large radius increases visibility but more importantly, as radius does not significantly increase past one Jupiter mass, the thermal emissions become stronger. This is due to the increased gravitational binding energy, injected during formation from the additional accreted material and released as heat during gravitational contraction. Imaging also lacks a way to directly infer planetary mass, it must be modeled using formation scenarios to match observed brightness levels and radius. The upside is that this technique is sensitive in a region that would otherwise be unpopulated because for the other approaches mentioned here sensitivity decreases with orbital separation.

μ -lensing, as stated before, is very sensitive to the lensing systems architecture, as the lensed starlight must pass through one of the caustic regions. This limits the planet detections to intermediate separations of 1-10 AU. In turn, planet masses potentially as low as that of Mars are detectable with an overall mass bias much weaker than for other techniques. The massive downside of μ -lensing is that it relies on chance. A system with a planet must pass in front of another star right the instant a telescope is pointed at it. If the event is missed for any reason like weather or instrumental defects, there are no repeats.

Transit photometry relies on a planetary system to be aligned with the observer such that the planet visually passes over the stellar disk. The volume over which this is possible forms a cone between the stellar disk and the observer, resulting in a bias towards close in planets. Instrumental limitations further bias detections towards large planetary radii *relative to the host star*. The observed loss in brightness depends on the relative area of the stellar surface that is blocked. As such, a larger star requires a larger planet for the same effect than a smaller one. On the other hand, this allows for the detection of significantly smaller planets if one focuses on late type stars. The periodic nature of transits are also a big advantage over μ -lensing as it allows repeating missed observations, combining multiple periods and synergizes with the timing approach. Variations in the mid-transit times are indicative of unseen companions, similar to binary-eclipse variations. As a photometric technique it is however impossible to independently determine an individual planets mass. That requires either an assumption on the interior structure, measurements from one of the mass sensitive techniques or the measurable presence of additional planets which cause the previously mentioned transit timing variations (TTV). Modeling the TTV then allows to recover the planet masses.

Radial velocity, like the original pulsar timing, relies on the gravitational effect an orbiting planet has on the host star. In the absence of periodic signals intrinsic to the host, the technique uses measurements of the minute shifts in a stars projected velocity along the line of sight that varies in tandem with the planets orbit. Since this relies on the planets gravitational impact, the technique is heavily biased towards massive planets. Gravity's distance dependence also biases detections towards close-in planets, leading to an overlap with the transit method, though an increase in planetary mass can compensate at intermediate distances. Unlike the transit methods boolean cutoff, either a planet transits or it does not, RV measurements can reveal planets at significantly higher inclination angles. This decreases the projected velocity for increasing inclinations and limits all measurements to become lower bounds as planetary mass and inclination angle are degenerate parameters. It requires an independent determination of the angle to resolve, commonly from transit photometry, which further completes the picture with the planetary radius.

1.2.1. Transit Method

Among all the techniques employed over the last three decades, the transit photometry approach has been the most successful by far, accounting for nearly 70% of all confirmed exoplanets. With over 2700 confirmations (NASA Exoplanet Archive⁴), again about 70% of those have been discovered by the Kepler space telescope with the Transiting Exoplanet Survey Satellite (TESS) expected to at least match that number during its mission life time. The dominance of the transit method is not surprising, as it is not just one of the most intuitive but also the easiest method to employ large scale. All it takes, in principle, is a telescope that keeps pointing at the same area of the sky, taking an image every few minutes and one can extract and analyze the lightcurves of many thousands of stars at once. Compared to the second most successful method, radial velocity, which can at most observe a few stars at a time due to the necessity of a high-resolution spectrograph, this is a massive advantage.

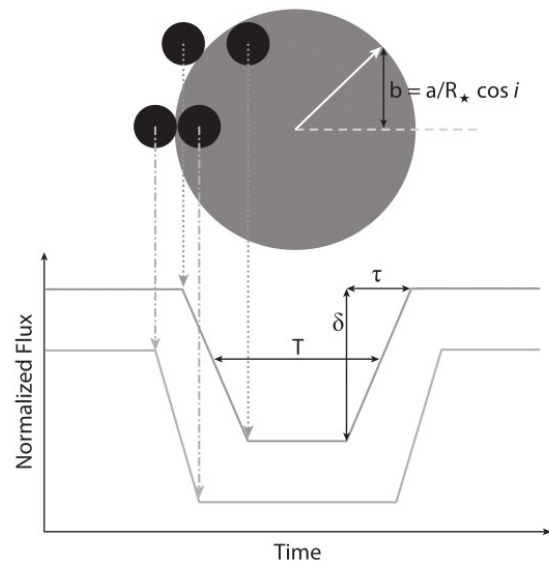


Figure 1.2.: Theoretical transit lightcurve, demonstrating transit depth δ , transit duration T and ingress/egress duration τ .³

As briefly explained in Section 1.2, the transit method relies on the observation of the short decrease in observed brightness of a star while its companion passes between it and the observer. This temporarily blocks a small fraction, typically 1-2% for massive planets, of the stars light from reaching the observer. Figure 1.2 shows a simplified model of the process where a planet passes at two different inclinations over the stellar disk. In this simplified model, the transit lightcurve itself is characterized by three parameters (Winn 2010) while continued observations also allow to determine the orbital period P from measuring consecutive transits:

The transit depth δ , which captures the loss of brightness during the transit relative the the stars brightness out of transit. This quantity corresponds to the relative visible size of planet and star and is dictated by the planet-to-star radius ratio squared $\delta = k^2 = \left(\frac{R_p}{R_*}\right)^2$, as it is the cross-sectional area that defines the quantity of light that gets blocked. This allows for an easy determination of the planet radius if the star has been previously determined through independent means.

³© John Asher Johnson, CC-BY; copied from https://en.wikipedia.org/wiki/File:Theoretical_Transiting_Exoplanet_Light_Curve.jpg

⁴https://exoplanetarchive.ipac.caltech.edu/docs/counts_detail.html

The transit duration T , which captures the time it takes the planet to cross the stellar disk. It is usually defined as the time between the second and third contact, when the planet is in front of the star in its entirety and excludes the ingress and egress times. Assuming a circular orbit with low inclination, the impact parameter b (see Figure 1.2) can be recovered from the transit duration, as $T \approx T_0 \sqrt{1 - b^2}$. The factor T_0 denotes a characteristic timescale for the system as $T_0 = \frac{R_* P}{\pi a}$. This can either be calculated if the mass of the star is known by employing Kepler's third law to obtain the semi-major axis a from the orbital period or by also solving for the ingress/egress duration.

The ingress/egress duration τ describes the time it takes the planet to move in front of or off of the stellar disk with its entire area (first to second or third to fourth contact). Like the transit duration T , it can be used to infer the impact parameter b though it also depends on the radius-ratio k . If the host star is not well characterized or an independent determination is desired, τ can be solved simultaneously with T to obtain the characteristic timescale T_0 in addition to the impact parameter.

If the orbit is not circular, correction factors can be applied to take into account the eccentricity e and argument of periastron ω . Theoretically, these values can be obtained from minute differences of the ingress and egress times of individual transits but are commonly inferred either from Doppler spectroscopy through the radial velocity method or by fitting the parametric model to the lightcurve, including the timing of the secondary eclipse where the planet passes behind the star, rather than analytically inverting the measurements. The

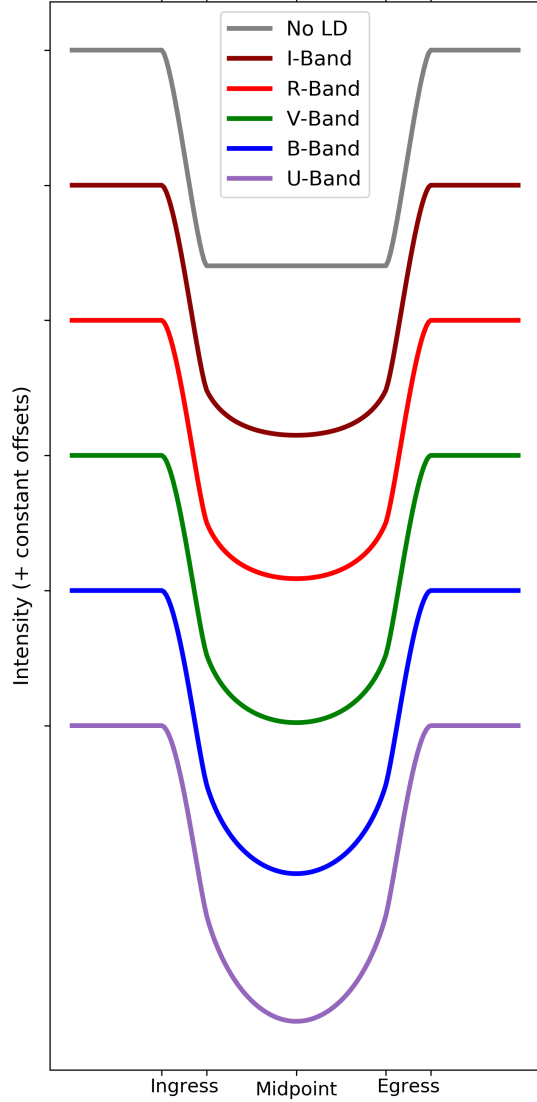


Figure 1.3.: Model light curves at different wavelengths. The decreasing effect of limb darkening on the shape of the lightcurve with increasing wavelength is apparent when compared to the model without limb darkening. The curves were modeled with a quadratic limb darkening law (Claret & Bloemen 2011) and interpolated coefficients from the EXOFAST web applet⁵(Eastman et al. 2013).

⁵<https://astrutils.astronomy.osu.edu/exofast/limbdark.shtml>

later is the preferred option as only a small fraction of observed stars have corresponding RV observations and observed lightcurves deviate in significant ways from this toy model. Figure 1.3 illustrates the most significant deviation; wavelength dependent limb-darkening of the host star that curves the ingress/egress flank and the bottom of the lightcurve. Limb darkening describes the observed decrease in brightness from the center towards the limbs of a stellar disk. The effect is easily visible on images of the Sun and is caused by the decreasing viewing angle towards the stellar limb. Under a lower angle, the line of sight travels a longer path through the upper stellar atmosphere at lower temperatures and can't penetrate into the deeper, hotter and brighter layers until it is blocked by the cumulative opacity. Since the limb of the star appears darker, the amount of starlight blocked during a transit is also less than in the toy model until the planet reaches the transit mid-point, smoothing the shape of the lightcurve. The optical opacity of the stellar atmosphere that determines the shape of the limb darkening law further depends on wavelength, becoming weaker for longer wavelengths. This causes additional changes to the lightcurve depending on the bandpass of the camera with shorter wavelengths effectively lacking the flat bottom of the transit that would be expected between second and third contact for the toy model (see Figure 1.3).

By itself, transit photometry can reveal the planet-star radius ratio and, as long as the observation baseline is sufficiently long, the orbital period. Basic knowledge of the host reveals the actual planet radius, its inclination and semi-major axis. A detailed analysis of the lightcurve further allows for the inference of an extended atmosphere if the shape of the flanks can not be explained by limb-darkening alone and, during the secondary eclipse when the planet passes behind the star, the planets albedo and even dayside temperature. The methodological ease, together with the simple simultaneous observability of thousands of stars is tempered by the small probability that a planet actually transits its host, the fact that a planets presence is only detectable during the brief time it actually transits and the inability to determine any mass or composition related values of the planet. For this, as well as to obtain the stellar parameters required, spectroscopy is much better suited and synergizes very well with the transit method which can compensate the shortcomings of the RV method.

1.2.2. Radial Velocity

The second most successful planet hunting technique, the radial velocity (RV) method, relies on directly measuring the movement of host stars along the observers line of sight in response to the companions orbital motion. This reflex motion always mirrors the motion of the planet in accordance with Kepler's laws of planetary motion which dictate, unlike the common phrasing, that it is not just the planet orbiting the star but in fact both orbiting the stationary, common center of mass in tandem (see schematic in Figure 1.4). The much larger mass of the star means that the center of mass is deep inside its interior and the reflex motion much weaker and slower

than the orbital motion of the planet. Solving the equations behind Kepler's laws, one can obtain the orbital geometry of a given system but not easily the motion of the bodies in time. That requires solving what is called Kepler's equation: $M = E - e \sin E$. It relates the mean anomaly M , which describes the angular movement of a body in time as if it were on a circular orbit of the same period, with the eccentric anomaly E , which is the actual angle between periastron, the center of the orbit and the bodies position along the orbit. For circular orbits the two are identical while non-zero eccentricities e cause the eccentric anomaly to grow non-linearly in time, unlike the mean anomaly which always grows uniformly.

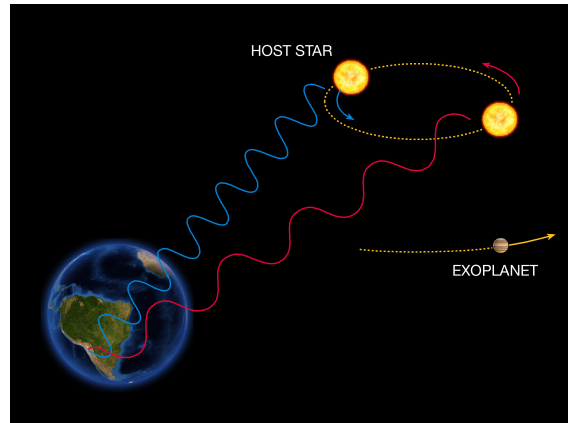


Figure 1.4.: Illustration of the radial velocity method.⁶

Actually solving the Kepler equation is not trivial however, as it is a transcendental equation and does not have an analytic solution. It requires numeric root finding to solve and to obtain velocity curves in time⁷ (see Fig. 1.5 for examples). Global, time-independent orbital parameters like the velocity amplitude, or semi-amplitude K as is more commonly used, of the stellar reflex motion does not require this though and can be derived as follows from Kepler's laws:

⁶© European Southern Observatory (ESO), CC-BY; Copied from <https://www.eso.org/public/images/eso0722e/>

⁷A great simulation tool is available from the University of Nebraska-Lincoln as part of their ClassAction program package. It can be downloaded under <https://astro.unl.edu/nativeapps/> for windows and MacOS. The simulator is called the "Radial Velocity Simulator (NAAP)" and found under the Animations tab on the main window.

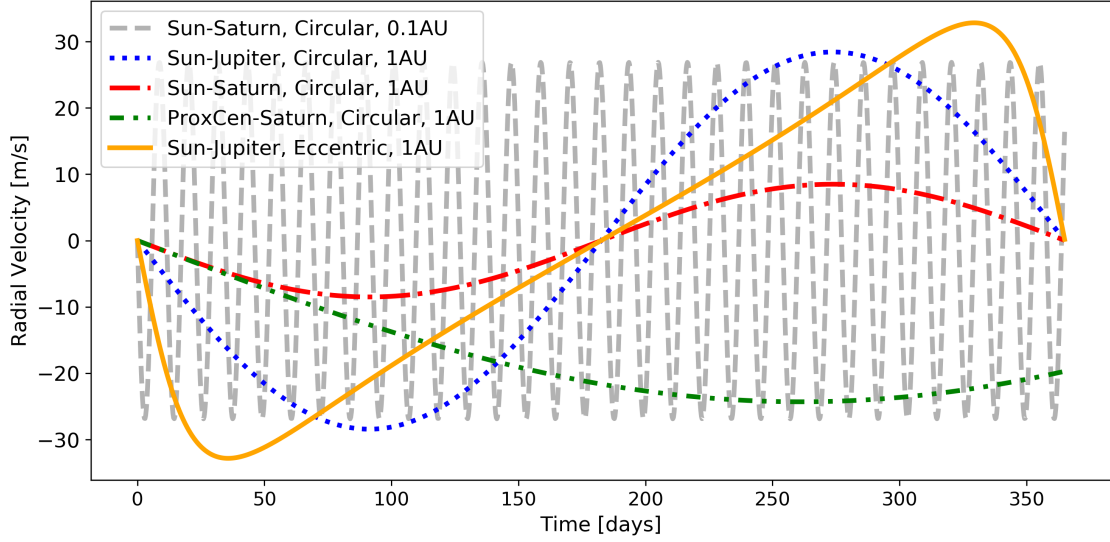


Figure 1.5.: Example RV curves for different combinations of star- and planet mass, eccentricity and semi-major axis (see legend).

$$K = \frac{m_p}{m_\star^{2/3}} \left(\frac{2\pi G}{P} \right)^{1/3} \frac{\sin i}{\sqrt{1-e^2}} \quad (1.1)$$

$$= \frac{1}{1 + \frac{m_\star}{m_p}} \frac{2\pi a}{P} \frac{\sin i}{\sqrt{1-e^2}} \quad (1.2)$$

Here, m_p is the mass of the planet, m_\star the host mass, G the gravitational constant, P the orbital period, i the inclination of the orbit and e again the eccentricity. Unsurprisingly, the planet to star mass ratio defines the amplitude, with a heavier planet or a smaller star increasing the velocity (see Figure 1.5, the Sun-Jupiter, Sun-Saturn and Proxima Centauri-Saturn lines), although the dependence on the stellar mass is slightly weaker as seen by the smaller than unity exponent. Using Kepler's third law, it is also possible to express K as a function of the pure mass ratio (see Equation 1.2), though this introduces the semi-major axis as an additional parameter that needs to be determined first and which is not independent of the period and masses. In the case of a smaller star the orbital period also increases, since the total mass, which is approximately equal to the stellar mass due to the comparatively very small size of most planets, decreases, weakening the gravitational binding between star and planet. This relates to Kepler's third law, which states that the square of the orbital period is proportional to the cube of the semi-major axis of the orbit. Therefore a longer period serves to decrease the velocity amplitude because it means, all else being equal, that the planet orbits further away from the star and the gravitational influence becomes weaker, requiring lower velocities to remain in orbit (compare Figure 1.5, Sun-Saturn lines at 1.0 and 0.1 AU). As mentioned in Section 1.2, the inclination angle projects the space velocity of the star along the line of sight

and can not be derived only from RV data. As such, all quantities derived from the velocity, like planetary mass, retain the inclination as an uncertain parameter. The semi-major axis on the other hand can be derived exactly. Finally, the RV method is much more sensitive to orbital eccentricity than the transit method, which generally requires an additionally observed secondary eclipse, as it can record the entire orbit rather than just a small portion, even allowing to determine the argument of periastron. This is the angle between the planets ascending node, where it passes upwards through the orbital plane, and the periastron, where the planet is closest to its host, and defines part of the orientation of the orbit in space. Compared to a circular orbit of the same period, a not unrealistic eccentricity of 0.5 increases the semi-amplitude by an easily measurable 15% (see Figure 1.5, Sun-Jupiter lines for different eccentricities; also Equation 1.1).

There are a number of ways that the radial velocity of a star can be determined, though all of them rely on spectroscopic measurements and the interpretation of spectral line shifts. These shifts are caused by the Doppler effect, which shifts wavelengths to the blue if an emitting object moves towards the observer and to the red if it is moving away. As the star moves around the barycenter the Doppler shift varies with the orbital period between the two, depending on the current phase. Due to the small velocities involved, a few hundred m s^{-1} for the most massive, ultra-hot Jupiters and down to $\sim 9 \text{ cm s}^{-1}$ for the Earth around the Sun (see Equation 1.1), the spectra need to be recorded with extreme precision and the first instruments theoretically capable of detecting Earth-twins have only recently come online (ESPRESSO, [Pepe et al. 2010](#); EXPRESS, [Jurgenson et al. 2016](#)). Actually extracting the velocity from the stellar spectrum can be done in principle by simply measuring each individual lines position, comparing to laboratory wavelengths and then averaging the results. Incomplete and not perfectly accurate reference data makes that approach a lot more difficult than it sounds though, together with effects intrinsic to the stars that affect the shape and positioning of individual spectral lines (see Section 1.4). Alternatively, one can cross-correlate the observed spectrum with a binary mask ([Baranne et al. 1996](#); [Brahm et al. 2017](#)), in practice a series of narrow box functions that correspond to a number of well characterized spectral lines either derived empirically from reference stellar spectra or constructed from line list. It is also common to cross-correlate directly with a reference spectrum, either empirical or synthetic ([Husser et al. 2016](#)), to avoid issues with uncertain laboratory measurements or unaccounted stellar influences. Lastly, auto-correlating the observed spectral time series, potentially involving a coadded template spectrum where all recorded spectra are averaged, is very effective in determining velocity variations though, on its own, not absolute velocity as it all depends on the template ([Anglada-Escudé & Butler 2012](#); [Zechmeister et al. 2018](#)).

The RV time series itself, like a series of transit measurements, allows to determine the orbital period. The velocity semi-amplitude K can then be used to analytically infer a minimum planet-star mass ratio under the assumption of a circular orbit. Again similar to the transit method, knowledge of the host star is required to derive the actual planets minimum mass and orbital semi-major axis. The eccentricity and periastron argument of the orbit can be determined by fitting a parametric Keplerian signal to the data, which also gives a more realistic value for the planet-star mass ratio than the derivation from K

alone. If this is attempted, the residual of the fit can also be analyzed to the same end as the reflex motion due to the combined presence of multiple planets is additive, allowing to confirm the presence of multiple at once. The big downside of the RV method, besides the $\sin i$ degeneracy, is that it relies only on the gravitational influence of the planet on its host. As such anything related to the size of a planet is unobservable. This can be solved if the RV observed planet happens to also be transiting, allowing to obtain the inclination to resolve the mass degeneracy and combine size and mass measurements to define a planets density or correct for stellar effects that affect one method but not the other (see Section 1.4 or 4.4). A transiting planet observed spectroscopically also allows for atmospheric transmission spectroscopy, where the minuscule portion of starlight that passes through a planets atmosphere is extracted and analyzed to determine the atmospheric structure and composition. Similarly, when the host star spectrum is removed from the observations, it is possible to analyze the starlight reflected off of the planet, even when it is not transiting or does not have an atmosphere (Kreidberg 2018). Either way further allows for the orbital velocity of the planet to be determined from the shift of the reflected stellar spectrum, lifting the $\sin i$ degeneracy since the planetary velocity depends on the same parameters as the stellar one but can be determined independently this way.

In difference to the transit method the RV method can not easily be applied to a massive number of stars at once since a single spectrograph is rarely capable of processing many spectra simultaneously (integral field spectrographs notwithstanding, though they generally only have lower resolutions) unlike a photometric CCD which can capture as many stars at once as its field of view and resolution allows. Fortunately, the timescales of RV variations are much longer than the lengths of observation windows for transits or microlensing events. At only a few minutes to hours the later are easy to miss, while the former generally operates on the order of at least days even for short period planets. That makes it possible to cycle through the stars on a schedule and only take one spectrum per night or less, although the Nyquist criterion requiring at least two data points per period should still be observed. As a continuous, periodic process it is further possible to fill missing data from one orbital period with observations from the next by phase folding the time series once the period has been determined.

1.3. Problems of the current methods

The transit photometry and radial velocity techniques have been very successful in detecting exoplanets, as was detailed in the previous parts of this chapter. They also provide very strong synergy that has allowed for the characterization of exoplanets to an incredible level, revealing planet types that were completely unknown from our own Solar System, such as hot Jupiters, mini Neptunes and super Earths. Their incredible success in unveiling the abundance of planets around the stars of our galaxy has left us with a lot of questions however. Unlike the initial expectation from the Copernican principle, planets similar to those of our Solar System are fairly uncommon or even non-existent among the currently discovered exoplanets (see Figure 1.1), primarily due to both methods heavily favoring planets that are large in mass or radius relative to their hosts and on short period, close-in orbits. The problem with the orbital period is compounded by the fact that the confirmation of a planet requires observational baselines on the order of the orbital period. This would exclude analogues of the Solar Systems outer planets except Jupiter for example, which could be picked up after a decade of observations. Exceptions are possible for sufficiently massive planets where a partial RV curve or a single transit provide a strong enough signal to extrapolate the remaining orbit.

Observational biases and baseline issues can be solved however by statistically modeling the bias and with the passage of time required to extend the baseline. The bigger issues until the last couple years was instrumental noise and the inherent limitation in the extreme precision required. Last generation RV spectrographs like CARMENES (Quirrenbach et al. 2016) and HARPS (Mayor et al. 2003) were designed with a stability at the 1 m s^{-1} level whereas an Earth-mass planet at 1 AU around a solar-mass star, an Earth-twin, induces a reflex motion around 9 cm s^{-1} . Only the most recent generation of instrumentation, after more than 30 years of targeted development, is finally capable of reaching those levels of precision in their observations. That means that, in theory, we would expect the first detection of an Earth-twin as soon as the respective instruments have achieved the necessary baseline of observations. Unfortunately it has become clear over the last few years, even before this new generation of instruments had its debut, that reality is not that easy.

As already mentioned in Sections 1.2.1 and 1.2.2, stars are no fixed, boring canvas that can be used as a static background for exoplanetary observations. Instead, there are a number of effects intrinsic to the stars themselves that makes detecting low-mass exoplanets much more of a challenge than just instrumental precision. Stellar variability, a collective term for a wide range of effects taking place on and inside stars, introduces spurious signals that can serve to hide and even mimic the signals from exoplanets. More details on that will be given in Section 1.4. Alternative techniques like microlensing or direct observations are a lot less sensitive to activity of the host star but come with their own downsides, biases and challenges as explained in Section 1.2. As such it is necessary to find approaches to identify and remove stellar effects from observational data before true Earth-twins become detectable.

1.4. Sources of stellar variability

In the literature concerning exoplanet detections and stellar characterization, three terms are very commonly found: stellar variability, stellar activity and stellar jitter. Unfortunately, many authors don't take the time to explain why a specific topic is attributed to one of those terms and may even use them interchangeably, especially the variability and activity descriptors. To prevent misunderstandings and establish a common nomenclature, this chapter will begin with a short definition of those terms, as they are used in this thesis, before some examples that were encountered and covered during this PhD are given.

The term **Stellar Variability** is used as a phenomenological catch-all to describe any stellar observable that varies in time for reasons assumed to be intrinsic to the star and not due to external influences. The exact reasons as well as their number and how they interact to lead to the observed variability are either unknown or expected to not be important in the current context, otherwise the effect in question should be named directly.

In contrast **Stellar Activity** refers to specific processes that cause a star to deviate from a quiescent state, leading to observed variability. Activity processes are the underlying cause behind most observed variability and in general more than one process contributes at once to a specific observed variability feature. The two terms are commonly used interchangeably, particularly when only a single activity process is used to explain the variability but that practice quickly becomes confusing for processes such as granulation (see Section 1.4.3) that are part of the quiescent state of a star, therefore not technically belonging into the activity category, but cause variability nonetheless. A good rule of thumb is that any process related to the stellar dynamo and magnetic field, such as starspots, plages, faculae and many others, are activity processes while processes that do not require specific magnetic phenomena are general variability contributors and should be individually named.

Finally, **Stellar Jitter** derives from a term used in statistical modeling. There, the jitter term is used in, for example, log-likelihood optimization to capture a level of variations that are not explained by the current model (which comprises of the expected signals and uncertainties from the instrument itself) but considered an intrinsic systematic of the observation (as opposed to noise, which is randomly distributed without systematic). In the case of stellar jitter this generally refers to any sources of variability that are unresolved in the observations, be it from insufficient instrumental resolution or a too long stepping between observations, or residuals due to incomplete models. As such, stellar jitter should always be low in amplitude compared to the signals in question and operating on short timescales relative to the current observational capabilities.

It was already stated that stellar activity is generally caused by stellar magnetic effects. Similarly one might state that any non-activity related variabilities derive from stellar convection (see Section 1.4.1). Together, the overarching theory of stellar magneto-convection, derived from the equations of Magneto-Hydrodynamics (MHD), can be seen as the underlying cause of any stellar variability. Unfortunately, solving the equations

of MHD is analytically impossible and truly realistic simulations are beyond our current computational capabilities. In practice one must therefore decide on a subset of effects to focus on that are expected to be the primary contributors for a specific facet of stellar variability. Finding simplified models for each, that are none the less accurate enough and computationally or observationally tractable is the biggest challenge in current exoplanet research. Three of these effects are explained in more detail in the following sections, how they operate, how they can be derived from theory and observation and how their influence on observations might be mitigated.

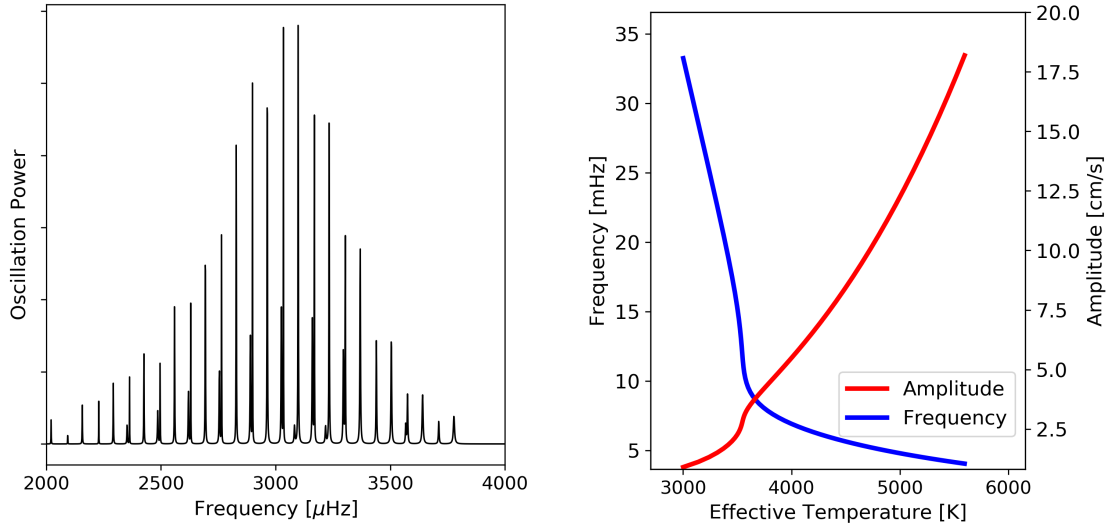


Figure 1.6.: Left: Model power spectrum for solar oscillations, based on the SOHO/VIRGO SPM observed frequencies included in *shocksgo*⁸. Right: Changes of amplitude and frequency of the mode of highest power over the ZAMS.

1.4.1. Acoustic oscillations

Stars, like any other object, have the ability to contain standing waves in their interior, similar to a struck bell. These standing pressure waves cause the star in its entirety to oscillate slightly in radius (or rather shape, depending on the oscillation mode), temperature (from adiabatic compression), and brightness (follows due to the Stefan-Boltzman law), which makes it possible to observe their effects. This can be done either photometrically by recording the brightness changes, which is what the Kepler, TESS and soon PLATO spacecraft were geared to do for thousands of stars, or spectroscopically, as the expanding and contracting motions of the stellar surface applies minute Doppler shifts to the radiation emitted from each location. Since the oscillations are periodic, intrinsic to the star and appear in both of the most common exoplanet detection methods, understanding them and finding paths towards their mitigation is important to avoid either mistaking them for planets (more important for RV, as transits appear clearly different in the lightcurve, and giant stars) or losing planetary signals in oscillation jitter (more important for main-sequence stars). This is particularly troubling because Earth-twins, as previously mentioned, cause Doppler reflex motions on the order of 10 cm s^{-1} , similar to the amplitude of solar radial oscillations.

The underlying cause for the oscillations are the turbulent motions from the stellar convection that stochastically excite the star in its entirety. The power spectrum of the oscillations can be decomposed into spherical harmonics, featuring modes of distinct frequencies and amplitudes that can be inverted to recover information in the otherwise unobserv-

⁸©Brett Morris, MIT license; shocksgo.readthedocs.io

able interior of stars (Christensen-Dalsgaard 2002). Analogous to geophysical seismology this field of study is called helio- or asteroseismology, depending on if it is used to study our Sun or stars in general.

A model example for a solar oscillation power spectrum is shown in the left panel of Figure 1.6. The entire spectrum is bounded by a Gaussian-like envelope with radial (angular degree $l = 0$) and non-radial modes ($l > 0$) appearing as peaks under it. In the case of the Sun, as depicted in the left panel of Figure 1.6, the strongest mode appears at a frequency around 3 mHz, or a period of 5.5 minutes, and has a velocity amplitude of 23.4 cm s^{-1} . This value differs slightly from the right panel, because the Sun is a real, slightly evolved main sequence star while the panel represents a parametric model for younger stars. By applying a window function for a finite integration time, Chaplin et al. (2019) showed that it is possible to smooth out the periodic variations from the oscillations to enable the detection of small exoplanets. Unsurprisingly, they found that matching the integration time to the period of the strongest mode gives the biggest initial reduction in residual amplitude as most of the oscillation power is averaged to zero, with multiples of that successively including more of the weaker modes but increasing the observational effort. In the solar case a 5.5 minutes integration is already sufficient to achieve a reduction to the 10 cm s^{-1} level required for Earth-twin detections. Because the frequencies of the modes are sensitive to the stellar structure, which forms the basis for asteroseismic inversions, the mode of highest power and therefore optimal integration time varies from star to star and needs adjusting on a case-by-case basis for optimal results.

A simple way to take the changes of the oscillation power spectrum between stars into account is to apply scaling relations to the solar values, based on global stellar parameters that can be obtained independently, as derived by Kjeldsen & Bedding (1995).

$$v_{\text{osc}} \propto \frac{L}{M} \propto \frac{R^2 T_{\text{eff}}^4}{M} \propto \frac{T_{\text{eff}}^4}{g} \quad (1.3)$$

$$\nu_{\text{max}} \propto \frac{M}{R^2 \sqrt{T_{\text{eff}}}} \propto \frac{g}{\sqrt{T_{\text{eff}}}} \quad (1.4)$$

$$\Delta\nu_0 \propto \sqrt{\frac{M}{R^3}} \quad (1.5)$$

Here, v_{osc} refers to the velocity amplitude of the strongest mode, ν_{max} to its frequency, and $\Delta\nu_0$ to the large frequency spacing, the spacing between modes of consecutive radial order but unchanged angular degree. Taken together it is possible to transfer a solar power spectrum to other stars that are structurally not too dissimilar to the Sun, meaning they possess a convective envelope around a radiative core.

Using analytic models from Tout et al. (1996) for Zero-age Main-sequence (ZAMS) luminosities as a function of mass and Demircan & Kahraman (1991) for radii, combined with the Stefan-Boltzman-law for temperature, these relations can be used to model the ZAMS oscillation parameters. The right panel of Figure 1.6 demonstrates how this affects ZAMS stars less massive than the Sun in amplitude and frequency. It can be seen that cooler stars

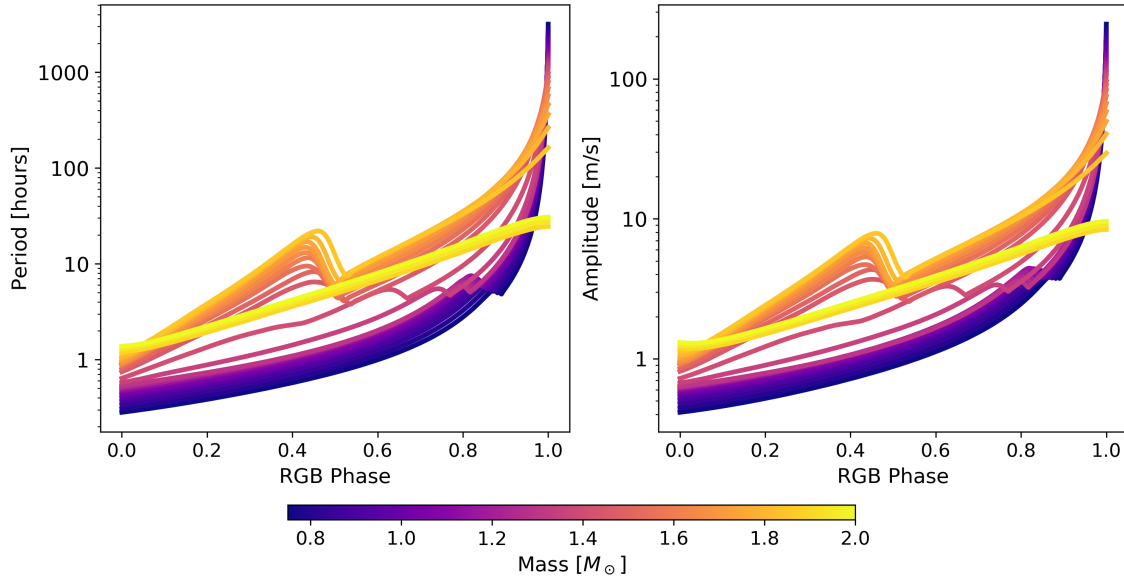


Figure 1.7.: Evolution of oscillation parameters for red giants stars over their time spend on the red giant branch. The phase is the fraction of time the star has spend as a red giant compared to the total time it will spend on the RGB.

oscillate at higher frequencies, requiring shorter integration times, and lower amplitudes, requiring less dampening in the first place. For hotter stars the opposite is true, making them more difficult to handle.

Using PARSEC stellar evolution grids (Bressan et al. 2012), plots matching the right panel of Figure 1.6 can be created for red giant stars of approximately solar composition. For this, a revised scaling relation for the frequency from Kjeldsen & Bedding (2011) was used that they claim better suited to evolved stars. For the amplitude, the formulation by Kjeldsen & Bedding (2011) was used with observationally calibrated exponents by Huber et al. (2011). Figure 1.7 shows that for evolved stars on the red giant branch, both amplitude and period increase dramatically, requiring hours of integration time (see also Figure 5 from Chaplin et al. 2019). This is not just unrealistic in terms of telescope time required but also in actually available observation time per night. Fortunately, coaddition of shorter integration time observations can substitute for this, as can periodogram analysis, since oscillations of this strength have left the region of jitter and are detectable on their own.

Testing whether or not the theoretical reductions through, for example, integration time are representative of what is achievable in actual observations generally requires a realized time series of synthetic RV or photometry to check the recovered system parameters. As an intrinsically stochastic process this means a statistical data generating process is necessary rather than a simple model, hence the terminology of "realized time series" for one draw from the distribution. One common example are Gaussian Processes, using combs of simple harmonic oscillators to model the p-modes as described from the scaling rela-

tions, as implemented in *shocksgo*⁹ and shown in Figure 1.6. Using Gaussian processes further allows the performance of regression analysis on observations to simultaneously fit the parameterized desired signal, together with contaminations like oscillations, characterized through hyperparameters, and even taking into account different observation paths at once (see also Section 4.4). With this approach Morris et al. (2020) were able to detect a simulated Earth-twin with a radius uncertainty of 3.6% under 100 ppm photometric variability from oscillations while the transit depth is only 87 ppm for an Earth-twin.

⁹©Brett Morris, MIT license; shocksgo.readthedocs.io

1.4.2. Starspots and rotation

Starspots, the stellar analogue to sunspots, are the best known example of stellar activity. They appear in regions on the stellar surface, where magnetic field lines are concentrated into tube-like structures that penetrate the surface to form loops above it (see Figure 1.8). The magnetic pressure exerted by these flux tubes partially counteracts the gas pressure in the area, lowering it, while keeping the total pressure constant. This leads to a decrease in gas density and correspondingly an increase in buoyancy relative to the surrounding medium. This increased buoyancy of the affected material, caused by the presence of the flux tube, prevents the hot plasma rising from the deeper layers of the stellar convection zone from immediately replenishing the material within the forming spot, diverting the flow around the affected area. This inhibition of the convective motion also delays the movement of the material within the spot back down into the stellar interior, letting it cool at the surface for a longer time. This cooler material is observable as a dark spot among the hotter and therefore brighter surroundings and always appears in pairs of opposite magnetic polarity, since the spots form as the footpoints of the loop structure from the magnetic flux tubes. The dark core of a sunspot formed this way, called the umbra, is surrounded by a strongly structured area called the penumbra, which is much closer in temperature to the surrounding photosphere. For an in-depth review of sunspots beyond the overview given in this section, see [Solanki \(2003\)](#).

The trapped, cooling gas within the spot can cover areas several times the size of the Earth which, while massive, is still only directly observable for our Sun. Other stars, outside a few interferometric measurements for giant stars, appear as point sources to the observer with only the disk integrated starlight reaching the detector. The observed light can then be imagined as the weighted and projected sum of the contributions of all the surface elements on the stellar hemisphere pointing towards the observer and hiding, to first degree, the specifics of the stellar surface structure, but still showing the influence of the presence starspots. To build a visual for this, one can start with a perfectly quiet, static star without any starspots or other activity features, where the spherical symmetry would then serve to average any center-to-limb deviations, giving constant brightness and symmetric, narrow spectral lines. In the

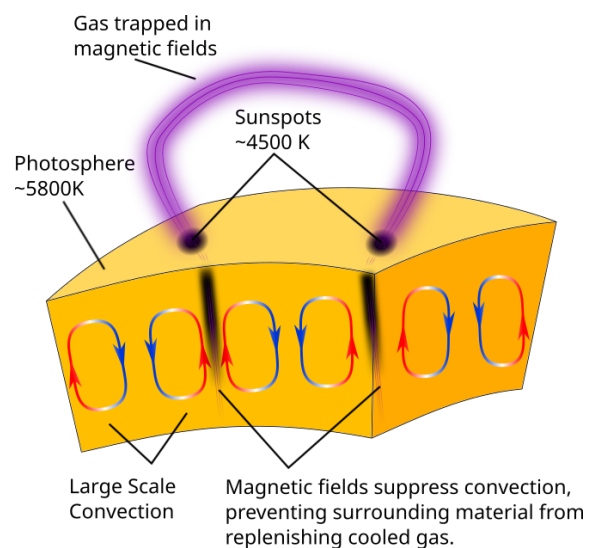


Figure 1.8.: Schematic formation of a starspot through magnetic inhibition of convective motion. ¹⁰

¹⁰Recreated and modified from an illustration © 2006 Pearson Education Inc., publishing as Addison Wesley

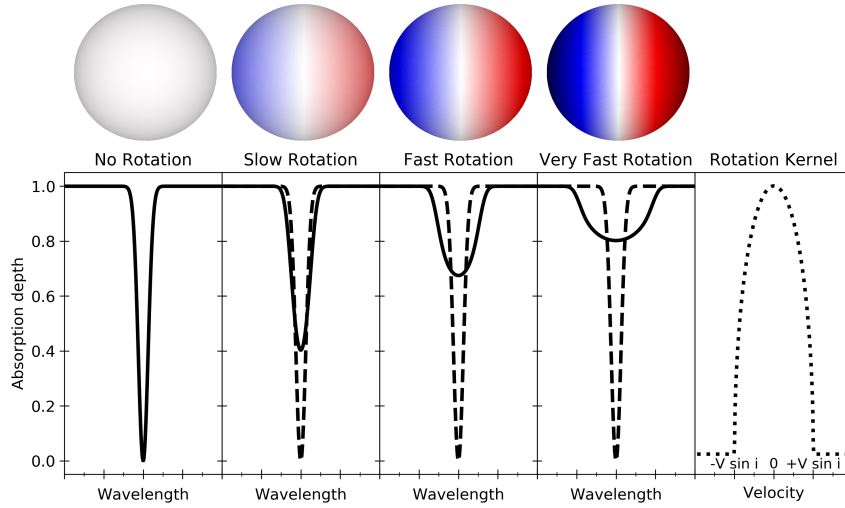


Figure 1.9.: Schematic illustration of rotational broadening from a rigid body model. Top: Doppler velocity map of the visible stellar disk, colored for blue- and redshift. Bottom: Effect of increasing rotational broadening on a Gaussian line profile. The unbroadened profile is plotted in dashed lines. The right panel without a corresponding map shows the rotation kernel¹¹ on a general velocity scale, with which the line profiles are convolved during the broadening process.

case of a pristine but rotating star this leads to a broadening of spectral lines due to the red and blueshifted projected components of the rotational velocity at the limbs, but no overall shift of the spectral line center as the opposite contributions cancel out (see Figure 1.9).

When a starspot is present however, it reduces the flux weighing of the covered surface segments and introduces an asymmetry while it moves over the visible hemisphere. As shown in the top and bottom panels of Figure 1.10, modeled with the DoTS code (Doppler tomography of stellar surfaces, Collier Cameron 1997), the presence of a spot on a stellar limb while rotating into view thereby reduces the local, blueshifted contribution to the overall velocity, resulting in a net redshift that decreases while the spot moves to the center of the disk and inverts as it moves out of view. The modulation of observed RV through rotating starspots is not a simple shift of entire spectral lines though, but a deformation of the profile where the asymmetry shifts the line center. This is illustrated in the middle panel of Figure 1.10 where the missing absorption at the velocity component covered by the spot moves from the blue wing of the line to the red wing while the spot is visible. This breaking of the symmetry in flux and the RV variations it causes, exaggerated here for the purposes of demonstration with an unrealistically large spot, are generally called the flux effect.

By employing a forward model it is then possible to invert the time series of spectral line deformations to recover the surface spot coverage that would cause the observed vari-

¹¹The rotational broadening was simulated using the `fastRotBroad` function from PyAstronomy (Czesla et al. 2019), based on the formulation by Gray (2021).

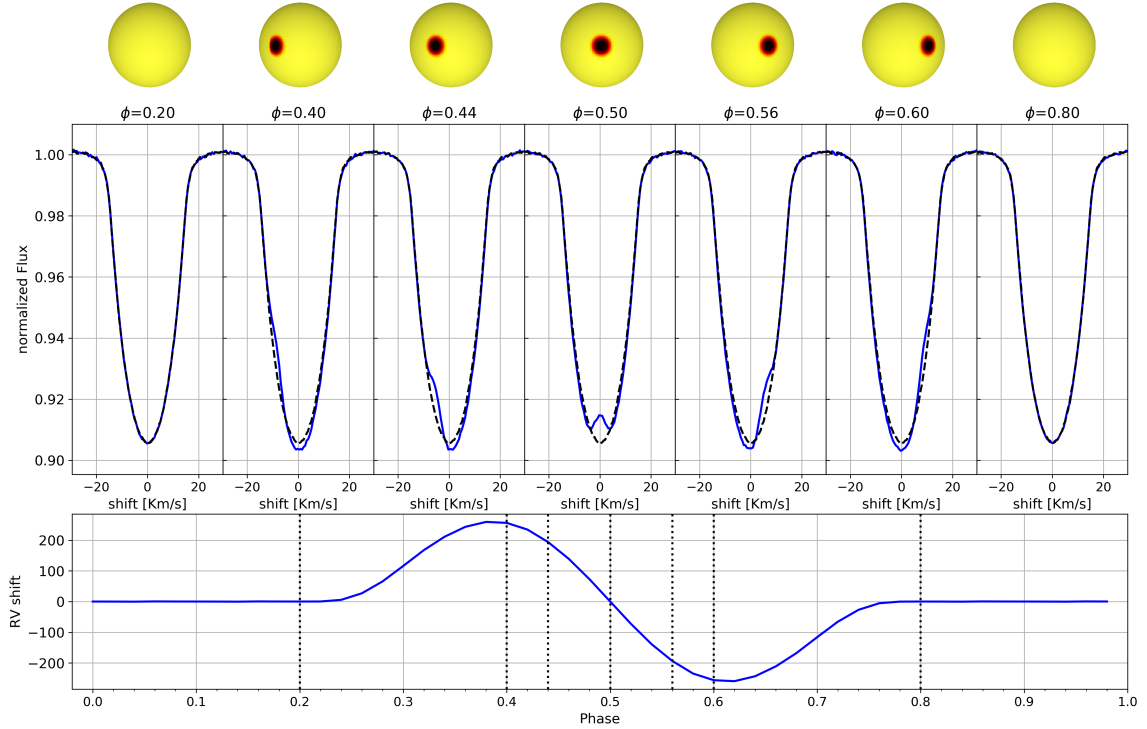


Figure 1.10.: Top: A rotating, equatorial starspot as simulated with DoTS (Doppler tomography of stellar surfaces, [Collier Cameron 1997](#)). Middle: Deformation of a spectral line over one rotation period, caused by the starspot. Bottom: RV deviations caused by the line profile deformation shifting the center of the line.

ations. As this attempts to recover a 2 dimensional map from projected 1 dimensional data, this requires additional assumptions to break the inevitable degeneracies. A common assumption is the maximization of entropy ([Skilling & Bryan 1984](#)) which prefers fewer, larger spots to groups of small ones, both of which would result in the same data. Additionally, if one imagines the surface map decomposed into spherical harmonics, at no loss of generality as they form a base for spherical surfaces, and then integrates each harmonic individually before summing, it becomes apparent that at best half the information of the surface map could ever be recoverable. This is due to the anti-symmetry of spherical harmonics of uneven angular degree. Integrated over the visible stellar surface the contribution of those harmonics averages to zero, similar to how an uneven function like $f(x) = x^3$ vanishes when integrated symmetrically around zero because $f(x) = -f(-x)$. All information contained in harmonics of odd degrees larger than 1 are therefore irrevocably lost in integrated starlight ([Luger et al. 2019](#)).

The biggest implications of rotational modulation of RV from starspots is that, on one hand, it allows to recover the stars rotation period assuming the spot lifetime is longer than one rotation and, on the other hand, that all planet searches have to content with the uncertainty that the signal under investigation might be due to stellar rotation instead of an actual planet. The first point is possible through either photometry, where the flux

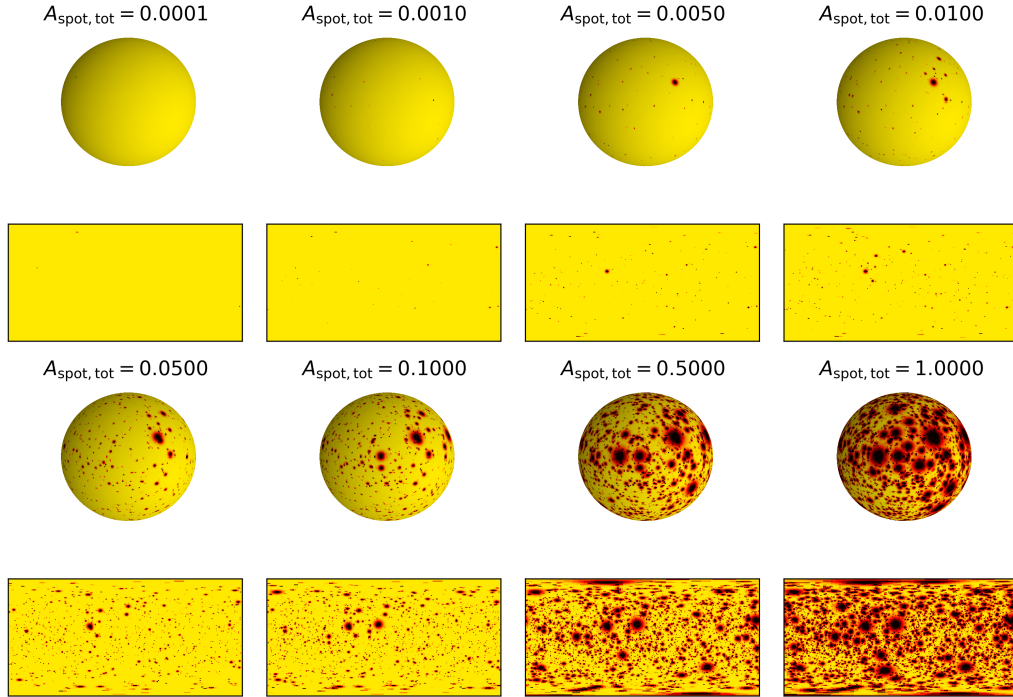


Figure 1.11.: Starspot maps projected on a sphere and as the corresponding equirectangular projection for a range of filling factors from 10^{-4} to 1.

effect is directly affecting the light curve, or spectroscopy, through the described changes in spectral line shape. If one has access to both, it is possible to recover the rotation period through photometry and then exclude that signal from the periodogram analysis of the RV time series, a process called pre-whitening, therefore clearing up the question of whether an observed modulation is a planet or not. Of course, real stars like our Sun and unlike the model from Figure 1.10 don't have singular, massive spots but a distribution of many smaller ones, aggregating into groups and spread over most of the stellar surface. This, combined with their finite lifetime and evolution therein, complicates the actual effects and identification of the stellar rotation period since the signal is now composed of many, overlapping, weaker signals. Periodograms can still, generally, recover the rotation period for stars that are strongly spotted, though more involved techniques like simultaneous or individual fitting of photometric and RV timeseries with Gaussian processes offer more powerful modeling opportunities, taking into account the quasi-periodic, statistical nature of spot occurrences as well as the underlying rotational broadening.

If one were to attempt to model the effects of more realistic starspot distributions than single-spot toy models, there are two main options: Either one starts from solar measurements, where individual spots can be resolved, counted and measured, and extrapolates under reasonable assumptions to other stars, or one takes the in-silico path and performs MHD simulations to do the same for simulated stars. For this thesis, the first path was explored, resulting in Figure 1.11. The figure shows one realization of possible spot coverage maps for a range of activity levels quantified by the spot filling factor. The filling

factor, denoted as $A_{\text{spot,tot}}$, is the fraction of the stellar surface covered by spots. In this work the penumbral area is included in that measure, hence why not the entire star is solid black in the bottom right of Figure 1.11, though this differs in some of the literature. As a simplification it is assumed that spots are randomly distributed over the entire stellar surface, with no active latitudes where spots may appear predominantly. The spot sizes are distributed log-normally, following observations from [Bogdan et al. \(1988\)](#) for the Sun, as shown in Equation 1.6. The number density of spots per spot area $\frac{dN}{dA}$ scales from the peak of the distribution $\left(\frac{dN}{dA}\right)_{\text{max}}$ and depends on the area A of the spot in question, the overall mean spot area $\langle A \rangle$ and the geometric standard deviation of the spot areas σ_A . [Solanki \(1999\)](#) provides a set of parameters for solar minimum and maximum as well as several extrapolations for higher levels of activity. Equations 1.7 and 1.8 are third order polynomial fits to the extrapolated peak covering fraction as a function of the filling factor. The standard deviation of spot sizes can be calculated from the peak value with the linear fit of equation 1.9 to the values from [Solanki \(1999\)](#). The last parameter, the mean spot size, can be obtained by integrating over $S_A = \frac{dN}{dA}A$ (following notation from [Solanki & Unruh 2004](#)), giving the total area covered by sunspots and ensuring it matches the desired covering fraction. To create a spot map one then simply has to numerically invert the cumulative distribution function for the spot size distribution obtained from Equation 1.6, normalized by dividing it by its integral over all areas, and insert uniformly drawn random variables. This has to be repeated until enough spot sizes are drawn to reach the desired total filling factor. Depending on the software solution used, one should again take into account the umbra-penumbra ratio of the spots as the size distribution counts for the entire spot while some modeling programs may assume the given sizes to be the umbra only.

$$\frac{dN}{dA} = \left(\frac{dN}{dA}\right)_{\text{max}} \cdot \exp\left[-\frac{(\ln A - \ln \langle A \rangle)^2}{2 \ln \sigma_A}\right] \quad (1.6)$$

$$\left(\frac{dN}{dA}\right)_{\text{max}} = \exp(0.0025f^3 + 0.0051f^2 + 0.4315f + 6.0446) \quad (1.7)$$

$$f = \ln(A_{\text{spot,tot}} \cdot 10^6) \quad (1.8)$$

$$\sigma_A = \left(\frac{dN}{dA}\right)_{\text{max}} \cdot 0.038 + 4.117 \quad (1.9)$$

Different stars at different activity levels do not differ only in their respective spot filling factors however. They also show different photospheric and spot temperatures that do not vary in tandem. Instead, the temperature contrast between the two is a function expressible in terms of the quiet photospheric temperature as shown in [Berdyugina \(2005\)](#) or [Panja et al. \(2020\)](#). For hotter stars, the temperature contrast between the photosphere and the umbra rises steeply from a few hundred Kelvin for M stars to almost 2000 K for early G types like our Sun. Further, as the spot is still to first order a blackbody radiator, the observed contrast depends on the wavelength under which the spot is observed. For

longer wavelengths the contrast decreases, as was shown by [Chapman & Meyer \(1981\)](#), by more than half from 400 to 1000 nm. This can be understood simply by taking the ratio of the two blackbody spectra corresponding to the umbra and photosphere, although for a real spot the picture is complicated by magnetic effects and the presence of the heavily structured penumbra. This chromaticity allows, in principle and among other things, to distinguish planetary RV from starspot induced variations because Keplerian reflex motion physically affects the entire star and is therefore achromatic. By shifting the observations into the infrared one can also heavily mitigate the effect starspots have on the RV.

One way to quantify this is the chromatic index (CRX), the linear slope of RV against the logarithm of the wavelength ([Zechmeister et al. 2018](#)). For a pure Keplerian signal the CRX should remain zero at all times. A rotating spot would introduce variations in CRX opposite in sign to the RV variations from the interplay of the flux effect with the chromatic contrast. While the spot rotates into view, RV is positive from missing blueshifted light while CRX is negative from the weaker effect at longer wavelengths. Conversely, a spot rotating out of view has negative RV from lack of redshifted light and positive CRX as the net-blueshift is weaker at longer wavelengths (see Figure 3 from [Zechmeister et al. \(2018\)](#) for an illustration).

The CRX has another use in the presence of starspots, as shown by [Baroch et al. \(2020\)](#): It can be used to infer the level of convective blueshift (see Section 1.4.3). Since magnetic activity suppresses convective motion, leading to the formation of the spots, the same is true for the local contribution to convective lineshifts and leads to a net redshift in the stellar spectrum from the lacking blueshift contribution. The effect this has over the stellar rotation period is illustrated in Figure 1.12, following Figure 7 from [Herrero et al. \(2016\)](#), but using DoTS simulated RV for the flux effect and a Gaussian model for the CBS suppression that could not be modeled with DoTS. The spot modeled here is much larger than in [Herrero et al. \(2016\)](#) however, hence the wider RV curve and the earlier onset because the spot starts to appear across the stellar limb earlier. Unlike the flux effect explained at the beginning of this section, which is anti-symmetric in its velocity variation with regards to the spots position relative to the stellar disk center (first rotating towards, then away from the observer), the CBS suppression is symmetric to this point (the suppressed motion is

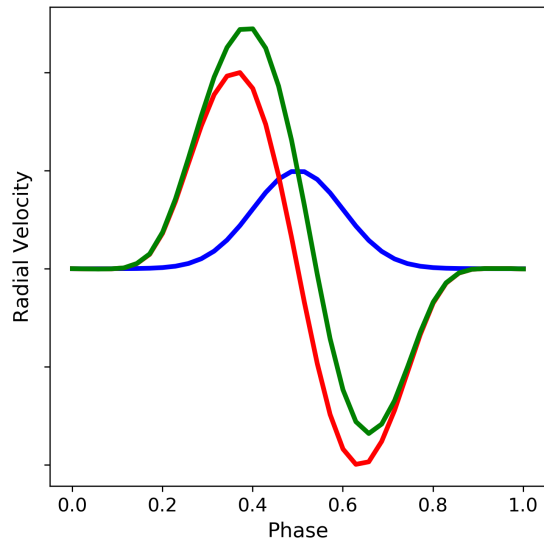


Figure 1.12.: Schematic model for the contribution of the flux (red) and CBS suppression (blue) effect of a rotating starspot and the combined effect (green).

always towards the observer, but projected onto the line of sight, see also Section 1.4.3). Combined into the overall observed RV this results in a phaseshift and asymmetry of the RV sinusoid while the CRX is nearly (see Section 2.10, Wavelength dependence of CBS) insensitive to CBS. If one plots the RV against CRX (Figure 1 in Baroch et al. 2020) for one rotation phase this opens the strict anti-correlation up into a lemniscate-like (shaped like the figure 8) shape, though ovals are also possible for some combinations of filling factor and CBS. The resulting shape is sensitive to CBS, filling factor and temperature contrast, allowing for modeled inversion of observational data to recover the three parameters.

Employing this approach in tandem with Keplerian planet fits to the RV may be a way to avoid the jitter from CBS suppression, especially if photometry is employed to, preemptively or simultaneously, fix the rotation period. Testing the efficacy of this approach however still requires knowledge of stellar CBS in terms of realistic strength and behavior to create the test data and verify the accuracy of the recovered parameters. This is true in particular for the CBS, as Baroch et al. (2020) found for the M-dwarf YZ CMi indications of convective redshift, something that has been speculated for low mass stars but never conclusively proven one way or the other, although in this work (Section 2.7.2 and Figure 2.6) a strong indication was found towards there being no convective red- or blueshift for early M stars.

1.4.3. Convective motion and granulation

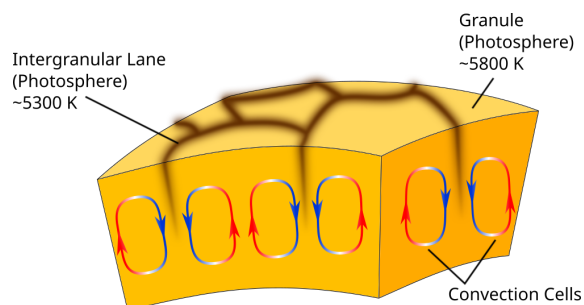


Figure 1.13.: Illustration of the formation of convective granules and intergranular lanes in stellar photospheres.¹²

The surfaces of cool stars like our Sun is characterized by a pattern of large, bright, irregularly formed regions, separated by a network of darker lanes (see Figure 1.13). This pattern is called granulation and is the result of convective energy transport in the upper atmosphere of stars where the tops of convective cells are exposed on the surface. The principle behind this is similar to how a pot of water heated by a stove from the bottom develops plumes of boiling water that rise to the surface and become visible (see chapter 11 of [Carroll & Ostlie 2014](#): "The interior of stars" for a

full, analytical review). In the case of a star, the role of the stove is played by the nuclear fusion reactions in the core releasing energy that needs to be transported to the outer layers so it can be radiated away. This can happen, to first approximation, in one of two ways: radiatively, where energy is transported through thermal radiation, and convectively, where heated material is physically moving the energy: The aforementioned pot of water. The boundary between the two modes is delineated by the Schwarzschild criterion: If the temperature gradient in the medium is steeper than the adiabatic gradient, the medium is unstable against convection. In this case a fluid parcel that is displaced upwards through random movement, will remain hotter than its surroundings after it adiabatically expands to match the surrounding pressure. The displaced parcel then retains a lower density through its higher temperature compared to its surroundings and keeps rising beyond the initial displacement. For sub-adiabatic temperature gradients, the parcel instead gets restored to its original position and energy can only be transported by radiation.

Figure 1.14 illustrates the implications for stars of different masses. At the low end of the mass spectrum, M-dwarfs below half the mass of our Sun are fully convective. The comparatively low temperatures throughout the entire star keep the opacity high, preventing efficient radiative cooling and leading to a high enough temperature gradient to keep the entire star convective. For stars at intermediate masses, up to 1.5 solar masses, this remains true for the envelope but the core temperature gets hot enough to ionize the gas and strongly reduce the opacity. This lowers the temperature gradient, as radiation is no longer trapped as strongly and leads to the formation of a radiative core that grows with mass. Above 1.5 solar masses the radiative core has completely replaced the convective envelope as even the outermost layers are hot enough to be ionized and allow radiation to pass. Instead, a convective core grows due to the increasing contribution of the highly

¹²Recreated and modified from an illustration © 2006 Pearson Education Inc., publishing as Addison Wesley; Following Figure 1.8

temperature sensitive CNO-cycle to the nuclear fusion process. Instead of opacity blocking energy from leaving the region, thereby enhancing the temperature gradient, it is now temperature itself enhancing the production of additional energy to increase the temperature gradient.

The convective granulation pattern observed on the solar surface is therefore expected to be representative to first order for all stars below 1.5 solar masses. The visual appearance is dominated by the large, bright regions called granules, which are formed by the freshly risen, still hot material (see Figure 1.13). As it cools at the surface it becomes darker and moves away from the center of the granule. Cooled material from neighboring granules collects at the boundary, forming the dark intergranular lanes, where it sinks back into the stellar interior to be re-heated. Mass conservation and the lower density of the hotter material leads to the differences in areal coverage. Observationally, because the rising material moves towards the observer on the visible hemisphere, all radiation emitted from within the granules experiences a slight spectral blueshift, called the *convective blueshift* (CBS). Conversely radiation from the intergranular lanes is slightly redshifted. The CBS is the net-dominant effect though, as the granules are both brighter and larger than the lanes and therefore dominate disk-integrated observations, which is all that is available for main-sequence stars beside the Sun, similar to the flux effect from starspots. Spatially resolved solar observations are therefore the only empirical source of information on the size distribution of granules, the structure of the lanes and how the observed velocities behave as one moves towards the stellar limb due to the projection and limb-darkening effects. Sun-as-a-star observations on the other hand allow to take advantage of the Sun's brightness for more detailed studies into the net-CBS effect in order to better understand lower quality observations of other stars with the Sun as a template.

Observing CBS, and granulation in general, over extended periods of time has revealed a big problem however: Just as convection is an intrinsically stochastic process, originating from random movements of fluid parcels, so are its derived effects. The number and size of granules covering a stellar disk is constantly changing, affecting observed brightness and CBS levels on time scales of ~ 10 minutes and, for sub-surface super-granulation, up to \sim days. For stellar observations with their constraints on integration and observation time, this leads to a base level of jitter in RV of up to several meters per second (Meunier et al. 2015), depending on the strength of convection of a star which increases, among others, with stellar age (see Chapters 2 and 3).

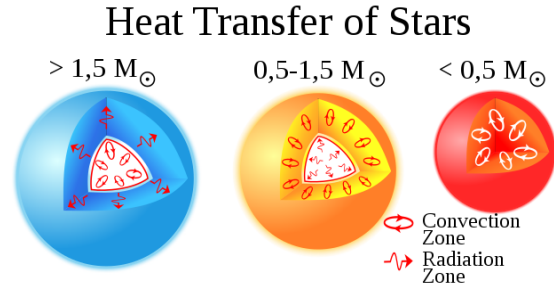


Figure 1.14.: Differences in energy transport for stars of different masses¹³

¹³©CC-0; copied from https://en.wikipedia.org/wiki/File:Heat_Transfer_in_Stars-en.svg

As was already alluded in Section 1.4.2 with Figure 1.8, convection and therefore granulation don't operate independently of stellar activity features. The presence of strong magnetic fields inhibits convective motion, leading to the formation of starspots but also to a local decrease in the CBS contribution. Since, aside from our Sun, stellar observation only capture the disk integrated light, this small decrease in CBS can't be avoided in observations and introduces rotational modulations in RV akin to the flux effect of starspots while the magnetic regions pass the visible stellar disk. Unlike the flux effect of starspots discussed in Section 1.4.2 where they modulate rotational broadening, which is strongest at the limbs, the CBS suppression is strongest at the disk center. This difference is due to the direction of the velocity components that get projected along the line of sight, which are tangential to the surface for rotation and normal for convection. This phase shift between the two was mentioned at the end of Section 1.4.2 with regards to the CRX-RV lemniscate. The situation is complicated by the fact that starspots are not the only magnetically active surface features one might find on a star. Another, in some ways more important, contributor are faculae or plage regions, depending on if they are observed in the photosphere or chromosphere. In difference to starspots, where magnetic activity was strong enough to cause an extended local cooling through suppression of convection, plages and faculae appear brighter than their surroundings though at significantly weaker contrast than spots. For faculae this can be explained by the "hot wall" model (Topka et al. 1997) under which magnetic fieldlines serve to depress the visual surface of the Sun, exposing deeper and thereby hotter layers of the photosphere along the walls of the depression. This also explains the limb brightening of faculae, as a lower viewing angle exposes more of the hot walls with a sharp drop at the extreme limb where the wall facing the observer is hidden behind its counterpart facing away due to the almost horizontal viewing angle. The reasons faculae and plages are considered the bigger problem compared to starspots is their smaller, inverted contrast and larger areal coverage (Meunier et al. 2010). The later was found to result in a bigger impact on the overall observed CBS modulation despite the lower local strength of the suppression, while the former prevents the use of photometry as a proxy for mitigation. Cancellation with the much stronger darkening from spots means faculae are almost invisible to photometry on the rotational timescale, although their effect over entire solar cycles has been found to be the primary contributor to changes in the total solar irradiance.

When it comes to mitigating granulation and CBS suppression jitter it is thereby much more difficult than for oscillations or starspots on their own because granulation is not a periodic process like oscillations but covers a wide range of frequencies. Unlike starspots, granulation is not stable over several observations nor slowly changing, but instead changes rapidly even within the time it takes to record a single observation. For more details on how the mitigation of granulation is attempted, why it is so difficult and how this work can contribute, see Section 4.4.

1.5. Measuring Convective Blueshift

The radial velocity shift induced by convection, similar to the RV shift from starspots' flux effect, is not an overall Doppler shift of the entire spectral line. Just as the line profile integrated over the entire stellar disk is deformed by the presence of a starspot on part of the disk, CBS appears even in spatially localized line profiles as they are an integration over the contributions from a range of optical depths. If the convective velocity were constant over the range of optical depths in question, then CBS would be a constant shift of the whole line profile, but the line forming region is part of the convective overshoot region. This means that the convective cells are slowing down as they get closer to the surface, before reversing their direction while forming the observable granulation pattern.

This leads then instead to a deformation of the entire line profile since rising, granular motion dominates the flux balance even below the stellar surface and each point in

flux along the line profile is formed by contributions at different optical depths. The weighing of optical depths for each point in flux along the profile is determined by the contribution functions (see for example Figure 13.2 in [Gray \(2021\)](#)). This means that the line core is formed predominantly at low optical depths, meaning high in the atmosphere where convection has slowed down significantly. Moving along the line wings also moves the weighing of the contributions deeper into the atmosphere, where convective velocity is still higher. With a spectral line at sufficiently high resolution and S/N ($R \gtrsim 300\,000$, $S/N \gtrsim 300$; [Dravins 1987](#)), this then allows to trace the velocity deformation along the line profile by tracing the profile midpoint in wavelength at constant flux values. Connecting the midpoints along the flux axis forms the line bisector, a common and often used diagnostic in spectroscopy. An illustration of a bisector is shown in Figure 1.15 for an empirically derived model and an observed spectral line (see also Figure 2.1 and Section 2.3.3.1 for details). The obvious difference between the two, the curve-back of the observed bisector, is due to the contribution of the redshifted flux from the intergranular lanes which dominates the wings (i.e. at deeper atmospheric layers) and is not captured in the model. This C-shape is characteristic for bisectors of cool stars and its width in velocity a first order approximation for the convection strength of a given star. The most common way

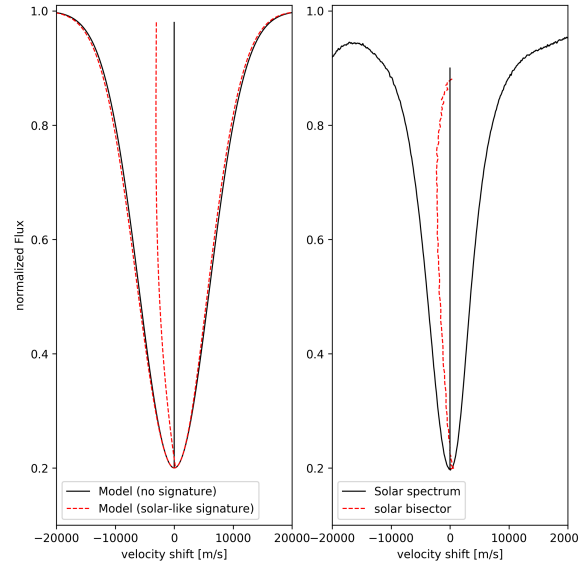


Figure 1.15.: Left: Gaussian model line profile without (black) and with (red dashed) a synthetic CBS signature. Right: Solar Fe 1 line from the [Reiners et al. \(2016\)](#) solar atlas. Both: The line bisector (red dashed) from the model and the real line, amplified 10 times for visibility.

to quantify this width is through the bisector inverse slope (BIS, also sometimes called the bisector velocity span), defined as the difference of the average velocity displacement within the top region of the bisector and the lower half (Queloz et al. 2001). Variations in BIS that correlate with RV have been used to argue successfully for stellar origins of exoplanet candidate signals, although the BIS inherits the difficulties of the bisectors high requirements. It is possible to use the cross correlation method to calculate the equivalent to an average line profile over an entire spectrum, increasing the S/N, and calculate an average BIS from the cross correlation function (CCF), but this relies on the assumption that each line carries the same information without systematic differences (see Section 4.4 for the implications).

Besides the high requirements on resolving power and S/N, the bisector has another downside in that it only traces convective velocity at optical depths corresponding to the values in flux the absorption depth of the analyzed spectral line covers. Shallower lines only trace deeper parts of the atmosphere, while deeply absorbing lines also cover the upper portion. This limits the number of lines that can be used for observations, as anything below fully absorbing lines does not have access to the full information, and therefore increases the chance for random errors due to small number statistics. Fortunately, bisectors from lines of the same species and close in wavelength trace the same velocity field and as such match each other at absorption depths they have in common.

This is especially useful because the lowest points of the bisectors from shallow lines, their footpoints, therefore trace bisectors from deeper lines and can be used to reconstruct them, avoiding the small number issue. Additionally, the bisector footpoint corresponds to the shift of the exact center of the spectral line, its core, which can be fitted directly without the interpolation necessary for the bisector and taking into account the entire core region, making a much more robust measure. Using footpoints of multiple lines allows then for the reconstruction of a more robust pseudo-bisector that is commonly called the third signature of granulation (see Figure 7 from Gray 2009). The first and second signature are considered the macroturbulence broadening and line asymmetry respectively. The third signature carries much of the same information as a deep lines' bisector as the left panel of Figure 1.15 illustrates. The line deformation is calculated from the solar third signature shown in Figure 1.16 (see also Figure 3.3 and Section 3.4 or Figure 2.4 and Section 2.6) and, except for the intergranular component which is not present in the line cores, matches a regular bisector. Figure 1.16 also demonstrates the massive advantage of the third signature technique: It

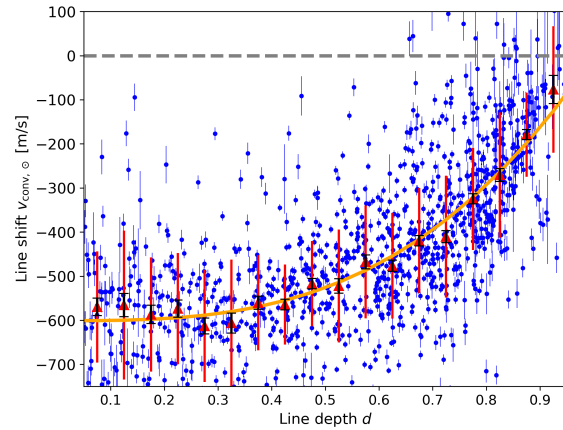


Figure 1.16.: The solar third signature of granulation, based on the Reiners et al. (2016) solar atlas with a custom line list and different signature model.

allows for the use of every spectral line in range of the spectrograph with an unblended core, adding very high statistical robustness to the resulting signature on top of the higher intrinsic robustness from the core fit.

Lastly, the final advantage of the third signature is that it is universally scalable between stars with convective envelopes as its shape does not change. Figure 1.16 shows a solar template, created from ultra-high resolution data (Reiners et al. 2016), which can be shifted and scaled to any other cool star to determine a relative strength of convection without having to fit an entirely new signature. Because the Sun is the brightest observable star the data also has extremely-high S/N, improving the accuracy of the template. Scaling such a high-quality template adds a third level of robustness to the technique and gives easy access to a way to compare CBS strengths of any low and intermediate mass star. The power of this approach is demonstrated in Chapters 2 and 3 while its implications towards stellar activity mitigation are explored in Section 4.4.

2. [Paper] Convective blueshift strengths of 810 F to M solar-type stars

The following chapter was previously published in the journal *Astronomy & Astrophysics* under the same title (Liebing et al. 2021). Credit: F. Liebing et al., A&A, 654, A168, 2021, reproduced with permission ©ESO. Some minor adjustments to the wording of structural references compared to the published version were made to conform with the Thesis format, replacing "paper" and "this work" with "this chapter". The layout was changed from two to single column format and Table 2.5 shortened by 4 rows to accommodate wider binding correction.

The coadded spectra analyzed for this work were provided by Trifon Trifonov (Trifonov et al. 2020). The analysis was carried out and the paper written by F. Liebing. The co-authors S.V. Jeffers, A. Reiners and M. Zechmeister provided their insight to help with the interpretation of the results and gave comments during the editing stage to further improve the clarity of the paper. Final corrections were made under the advise from an anonymous referee and a language editor from the journal.

FL acknowledges the support of the DFG priority program SPP 1992 "Exploring the Diversity of Extrasolar Planets (RE 1664/18). SVJ acknowledges the support of the German Science Foundation (DFG) Research Unit FOR2544 'Blue Planets around Red Stars', project JE 701/3-1 and DFG priority program SPP 1992 'Exploring the Diversity of Extrasolar Planets' (JE 701/5-1). The SIMBAD database¹, hosted at the CDS, Strasbourg, France, was used in this research. This research has made use of NASA's Astrophysics Data System Bibliographic Services². This work has made use of the VALD database³, operated at Uppsala University, the Institute of Astronomy RAS in Moscow, and the University of Vienna. This work has made use of data from the European Space Agency (ESA) mission *Gaia* (<https://www.cosmos.esa.int/gaia>), processed by the *Gaia* Data Processing and Analysis Consortium (DPAC, <https://www.cosmos.esa.int/web/gaia/dpac/consortium>). Funding for the DPAC has been provided by national institutions, in particular the institutions participating in the *Gaia* Multilateral Agreement. The original observations, provided after pre-processing by TT, were collected at the

¹<http://simbad.u-strasbg.fr/simbad/>

²<http://adsabs.harvard.edu/>

³<http://vald.astro.uu.se/>

European Organization for Astronomical Research in the Southern Hemisphere under ESO programmes: 0100.C-0097, 0100.C-0111, 0100.C-0414, 0100.C-0474, 0100.C-0487, 0100.C-0750, 0100.C-0808, 0100.C-0836, 0100.C-0847, 0100.C-0884, 0100.C-0888, 0100.D-0444, 0100.D-0717, 0101.C-0232, 0101.C-0274, 0101.C-0275, 0101.C-0379, 0101.C-0407, 0101.C-0516, 0101.C-0829, 0101.D-0717, 0102.C-0338, 0102.D-0717, 0103.C-0548, 0103.D-0717, 060.A-9036, 060.A-9700, 072.C-0096, 072.C-0388, 072.C-0488, 072.C-0513, 072.C-0636, 072.D-0286, 072.D-0419, 072.D-0707, 073.A-0041, 073.C-0733, 073.C-0784, 073.D-0038, 073.D-0136, 073.D-0527, 073.D-0578, 073.D-0590, 074.C-0012, 074.C-0037, 074.C-0102, 074.C-0364, 074.D-0131, 074.D-0380, 075.C-0140, 075.C-0202, 075.C-0234, 075.C-0332, 075.C-0689, 075.C-0710, 075.D-0194, 075.D-0600, 075.D-0614, 075.D-0760, 075.D-0800, 076.C-0010, 076.C-0073, 076.C-0155, 076.C-0279, 076.C-0429, 076.C-0878, 076.D-0103, 076.D-0130, 076.D-0158, 076.D-0207, 077.C-0012, 077.C-0080, 077.C-0101, 077.C-0295, 077.C-0364, 077.C-0530, 077.D-0085, 077.D-0498, 077.D-0633, 077.D-0720, 078.C-0037, 078.C-0044, 078.C-0133, 078.C-0209, 078.C-0233, 078.C-0403, 078.C-0751, 078.C-0833, 078.D-0067, 078.D-0071, 078.D-0245, 078.D-0299, 078.D-0492, 079.C-0046, 079.C-0127, 079.C-0170, 079.C-0329, 079.C-0463, 079.C-0488, 079.C-0657, 079.C-0681, 079.C-0828, 079.C-0927, 079.D-0009, 079.D-0075, 079.D-0118, 079.D-0160, 079.D-0462, 079.D-0466, 080.C-0032, 080.C-0071, 080.C-0664, 080.C-0712, 080.D-0047, 080.D-0086, 080.D-0151, 080.D-0318, 080.D-0347, 080.D-0408, 081.C-0034, 081.C-0119, 081.C-0148, 081.C-0211, 081.C-0388, 081.C-0774, 081.C-0779, 081.C-0802, 081.C-0842, 081.D-0008, 081.D-0065, 081.D-0109, 081.D-0531, 081.D-0610, 081.D-0870, 082.B-0610, 082.C-0040, 082.C-0212, 082.C-0308, 082.C-0312, 082.C-0315, 082.C-0333, 082.C-0357, 082.C-0390, 082.C-0412, 082.C-0427, 082.C-0608, 082.C-0718, 083.C-0186, 083.C-0413, 083.C-0794, 083.C-1001, 083.D-0668, 084.C-0185, 084.C-0228, 084.C-0229, 084.C-1039, 085.C-0019, 085.C-0063, 085.C-0318, 085.C-0393, 086.C-0145, 086.C-0230, 086.C-0284, 086.D-0240, 087.C-0012, 087.C-0368, 087.C-0649, 087.C-0831, 087.C-0990, 087.D-0511, 088.C-0011, 088.C-0323, 088.C-0353, 088.C-0513, 088.C-0662, 089.C-0006, 089.C-0050, 089.C-0151, 089.C-0415, 089.C-0497, 089.C-0732, 089.C-0739, 090.C-0395, 090.C-0421, 090.C-0540, 090.C-0849, 091.C-0034, 091.C-0184, 091.C-0271, 091.C-0438, 091.C-0456, 091.C-0471, 091.C-0844, 091.C-0853, 091.C-0866, 091.C-0936, 091.D-0469, 092.C-0282, 092.C-0454, 092.C-0579, 092.C-0721, 092.C-0832, 092.D-0261, 093.C-0062, 093.C-0409, 093.C-0417, 093.C-0474, 093.C-0919, 094.C-0090, 094.C-0297, 094.C-0428, 094.C-0797, 094.C-0894, 094.C-0901, 094.C-0946, 094.D-0056, 094.D-0596, 095.C-0040, 095.C-0105, 095.C-0367, 095.C-0551, 095.C-0718, 095.C-0799, 095.C-0947, 095.D-0026, 095.D-0717, 096.C-0053, 096.C-0082, 096.C-0183, 096.C-0210, 096.C-0331, 096.C-0417, 096.C-0460, 096.C-0499, 096.C-0657, 096.C-0708, 096.C-0762, 096.C-0876, 096.D-0402, 096.D-0717, 097.C-0021, 097.C-0090, 097.C-0390, 097.C-0434, 097.C-0561, 097.C-0571, 097.C-0864, 097.C-0948, 097.C-1025, 097.D-0156, 097.D-0717, 098.C-0269, 098.C-0292, 098.C-0304, 098.C-0366, 098.C-0518, 098.C-0518, 098.C-0739, 098.C-0820, 098.C-0860, 098.D-0717, 099.C-0093, 099.C-0138, 099.C-0205, 099.C-0303, 099.C-0304, 099.C-0374, 099.C-0458, 099.C-0491, 099.C-0798, 099.C-0880, 099.C-0898, 099.D-0717, 1101.C-0721, 180.C-0886, 183.C-0437, 183.C-0972, 183.D-0729, 184.C-0639, 184.C-0815, 185.D-0056, 188.C-0265, 188.C-0779, 190.C-0027, 191.C-0505, 191.C-0873, 192.C-0224, 192.C-0852, 196.C-0042, 196.C-1006, 198.C-0169, 198.C-0836, 198.C-0838, 281.D-5052, 281.D-5053, 282.C-5034, 282.C-

5036, 282.D-5006, 283.C-5017, 283.C-5022, 288.C-5010, 292.C-5004, 295.C-5031, 495.L-0963, 60.A-9036, 60.A-9700, and 63.A-9036.

The analysis was carried out using the programming language Python3⁴, and the accompanying software packages: Numpy⁵, Scipy⁶, Astropy⁷, Astroquery⁸, Matplotlib⁹, and PyAstronomy¹⁰(Czesla et al. 2019).

Table 2.4 and the full Table 2.5 are available in electronic form at the CDS via anonymous ftp to [cdsarc.u-strasbg.fr](ftp://cdsarc.u-strasbg.fr) (130.79.128.5) or via <http://cdsweb.u-strasbg.fr/cgi-bin/qcat?J/A+A/654/A168>.

⁴<https://www.python.org/>

⁵<https://numpy.org/>

⁶<https://www.scipy.org/scipylib/>

⁷<https://www.astropy.org/>

⁸<https://astroquery.readthedocs.io>

⁹<https://matplotlib.org/>

¹⁰<https://github.com/sczesla/PyAstronomy>

Contents

2.1. Abstract	39
2.2. Introduction	39
2.3. Convective line shift	41
2.3.1. Flux asymmetries from granulation	41
2.3.2. Impact on line shape	42
2.3.3. Blueshift measuring techniques	42
2.3.3.1. High-resolution techniques: Line bisectors	42
2.3.3.2. Low-resolution techniques: Third-signature scaling	43
2.4. Data	45
2.4.1. HARPS stellar data	45
2.4.2. IAG solar data	47
2.5. HARPS data processing	47
2.5.1. Boundary fit	47
2.5.2. Line selection	48
2.5.3. Telluric contamination	49
2.5.4. Initial radial velocity	49
2.5.5. Measuring line positions	50
2.5.6. Refining radial velocity	50
2.6. Modeling the solar third signature	51
2.7. Third-signature fit for the HARPS sample	53
2.7.1. F, G, and K stars	55
2.7.2. M stars	56
2.8. Discussion	57
2.8.1. Line list effective temperature selection	58
2.8.2. Influence of stellar activity	58
2.8.3. Influence of excitation potential	59
2.8.4. Comparison to other works	60
2.8.5. Extending the data set	62
2.9. Conclusion	62
2.10. Appendix	64

2.1. Abstract

Context. The detection of Earth-mass exoplanets in the habitable zone around solar-mass stars using the radial velocity technique requires extremely high precision, on the order of 10 cm s^{-1} . This puts the required noise floor below the intrinsic variability of even relatively inactive stars, such as the Sun. One such variable is convective blueshift varying temporally, spatially, and between spectral lines.

Aims. We develop a new approach for measuring convective blueshift and determine the strength of convective blueshift for 810 stars observed by the HARPS spectrograph, spanning spectral types late-F, G, K, and early-M. We derive a model for inferring blueshift velocity for lines of any depth in later-type stars of any effective temperature.

Methods. Using a custom list of spectral lines, covering a wide range of absorption depths, we create a model for the line-core shift as a function of line depth, commonly known as the third signature of granulation. For this we utilize an extremely-high-resolution solar spectrum ($R \sim 1\,000\,000$) to empirically account for the nonlinear nature of the third signature. The solar third signature is then scaled to all 810 stars. Through this we obtain a measure of the convective blueshift relative to the Sun as a function of stellar effective temperature.

Results. We confirm the general correlation of increasing convective blueshift with effective temperature and establish a tight, cubic relation between the two that strongly increases for stars above $\sim 5800 \text{ K}$. For stars between $\sim 4100 \text{ K}$ and $\sim 4700 \text{ K}$ we show, for the first time, a plateau in convective shift and a possible onset of a plateau for stars above 6000 K . Stars below $\sim 4000 \text{ K}$ show neither blueshift nor redshift. We provide a table that lists expected blueshift velocities for each spectral subtype in the data set to quickly access the intrinsic noise floor through convective blueshift for the radial velocity technique.

2.2. Introduction

The vast majority of exoplanets that have been discovered to date using the radial velocity (RV) method have been detected using instruments with a precision of 1 m s^{-1} . They have almost exclusively been detected orbiting solar-type stars, defined as stars possessing a convective envelope (i.e., spectral types of late F and below). Expanding the search to lower-mass exoplanets around solar-type stars remains a highly challenging but rapidly progressing field, both technologically and analytically. Examples for instruments that have been successfully employed to this end include CARMENES ¹¹ (Quirrenbach et al. 2016) and HARPS ¹² (Mayor et al. 2003) among many others. The next generation of

¹¹Calar Alto high-Resolution search for M dwarfs with Exoearths with Near-infrared and optical Échelle Spectrographs

¹²High-Accuracy Radial velocity Planetary Searcher

instruments has been designed to reach the 10 cm s^{-1} level of precision; these include ESPRESSO ¹³ (Pepe et al. 2010) and EXPRES ¹⁴ (Jurgenson et al. 2016), which have recently been commissioned, and others such as ELT-HIRES ¹⁵ (Marconi et al. 2016), which are expected further in the future. Instrumentation of this level is required in order to detect Earth-like planets around solar-type stars, which, using the RV method, requires an instrumental precision of 10 cm s^{-1} . However, extreme-precision instrumentation only solves part of the challenge.

Stellar surfaces, particularly those with an underlying convection zone, are not featureless and exhibit strong spatial and temporal variations. Well-known examples for the effects of magnetic activity include starspots and plages that corotate with the star and periodically modulate the RV on the order of several m s^{-1} (Barnes et al. 2015). This is due to asymmetries in the shape of spectral lines, introduced by magnetically active regions deviating from the quiet photospheres temperature, impacting the very precise measurement of the line center required for the RV technique. On a lower level, the statistical nature of stellar surface convection becomes relevant for Earth-twin detections. Granulation, including supergranulation, is one of the defining traits of solar-type stars; this is due to their outer convective zone and varies on timescales of minutes to days. It introduces further RV variations on the order of 10 cm s^{-1} up to 1 m s^{-1} , respectively, eclipsing any potential ultra-short-period, sub-Earth-mass planets and hiding the signal of an Earth-twin under stellar jitter. Even higher jitter levels are introduced through the suppression of convective motion by magnetic activity (e.g., Jeffers et al. 2014; Bauer et al. 2018; Meunier et al. 2010).

Another related jitter source is stellar acoustic oscillations, stochastically excited by turbulent convective motion. For stars such as the Sun, the amplitude of the mode of highest power is $\sim 20 \text{ cm s}^{-1}$ on a timescale of 5 minutes (Kjeldsen & Bedding 1995; Kjeldsen et al. 2008), even when neglecting all other modes. These oscillations can be mitigated by carefully choosing integration or coaddition times to match stellar oscillation frequencies (Chaplin et al. 2019; Dumusque et al. 2011). With all these jitter sources operating on a level comparable to the expected planetary signal but otherwise unrelated timescales, understanding the nature of each individual source and the effect it has on the overall velocity measurement is paramount in order to model and remove their influence (e.g., Meunier et al. 2017a; Miklos et al. 2020).

In this chapter we aim to measure one such contribution, the base level of convective blueshift (CBS), for a sample of >800 stars spanning spectral types from late-F to early-M. We expect a strong dependence of CBS on spectral type for two reasons: The depth of the convection zone increases and the energy flux decreases with decreasing mass. These fundamental changes in convective properties should be reflected in CBS. We begin with a description of the general principle behind convective line shift in Sect. 2.3. Section 2.4.1 details the data set that forms the foundation of this chapter, with Sect. 2.5 explaining

¹³Echelle SPectrograph for Rocky Exoplanets and Stable Spectroscopic Observations

¹⁴EXtreme PREcision Spectrometer

¹⁵Extremely Large Telescope-High spectral RESolution Spectrograph

the preparatory steps required on the data. The origin, processing, and results of the solar reference data are discussed in Sect. 2.6 and the final analysis of the sample stars with their results in Sect. 2.7. The results are discussed in Sect. 2.8 and summarized in Sect. 2.9.

2.3. Convective line shift

2.3.1. Flux asymmetries from granulation

The surfaces of cool stars, meaning those with an outer convective envelope, characteristically show a granulation pattern. It is composed primarily of granules, wide regions wherein hot material rises to the top of the convection zone, cools off, moves to the sides, and sinks back down between the granules in narrow intergranular lanes (Gray & Pugh 2012). These lanes form the secondary part, separating the granules, and appear darker due to the lower temperature of the material therein just as the granules appear brighter from the hotter material. In the case of a spatially unresolved star where only the disk-integrated stellar flux can be measured, the granules contribute more to the overall flux compared to the intergranular lanes due to their higher brightness and much larger covered area, leading to an imbalance in the flux representation. The magnitude of this imbalance changes strongly with stellar effective temperature, metallicity, and age, all of which influence the global convective pattern in terms of relative area covered by granules, absolute granule size and brightness, vertical velocity, and intergranular lane brightness and coverage, as well as the contrast between the two (empirical: Gray 1982, numerical: Beeck et al. 2013a; Magic & Asplund 2014).

Magic & Asplund (2014) show that the dominant granule size increases with temperature and metallicity and significantly decreases with surface gravity. Larger granules in turn are shown to be brighter and hotter and therefore have a higher contrast. The change in peak brightness and temperature with granule size is stronger in hotter or low metallicity stars, but is only minorly affected by surface gravity. Vertical velocity also increases with temperature and metallicity, as well as lower surface gravity, and shows a peaked distribution centered on the mean granule size, with the peak more pronounced in hotter stars.

The flux imbalance is unstable over time due to the randomly evolving distribution of granule size and location. The contrast between granules and lanes is constantly changing, and temporary patterns are rotating into and out of view. This limits the RV precision achievable for all measurements relying only on spectral data without accounting for these processes.

2.3.2. Impact on line shape

In convective granulation, rising material contributes more to the shape and location of a given spectral line than the sinking one. As it moves toward the observer, convection leads to a net blueshift. The magnitude of the shift further depends on the depth of formation of the spectral line, since convective velocity changes with depth, which roughly anticorrelates with the lines absorption depth. Therefore, with convection slowing down toward the stellar surface and deeper lines forming at higher layers, deeper lines tend to be less affected by convective line shift. The wings of deeper lines are then shifted independently from the core, following their contribution function, as if they were shallower lines of their own (Gray 2010a). Shallower lines are affected more strongly by convective shifts due to their deeper formation. This leads to an overall asymmetry in the line profile. The degree of this asymmetry then depends on the actual gradient of the convective velocity field with physical depth and the total absorption depth of the line. Lastly, for spatially resolved spectroscopy, meaning only on the Sun for now, limb angle factors in, as observation closer to the disk edges pass through the atmosphere at a shallower angle, observing longer paths while still high in the atmosphere. This increases the optical depth corresponding to a given physical depth and decreases the range of physical depths observable. The line contribution functions, depending on optical depth, shift upward in the atmosphere, changing the line profiles observed depending on limb angle (Beeck et al. 2013b). The RV method therefore suffers not only from the constant changes in the convective pattern and therefore the base line shift, it is further complicated by the dependence of overall velocity shift on the choice of spectral lines and method of measuring either each line's individual velocity or a combined value. Conversely, what is a problem for exoplanet hunters can be a major source of information for stellar astrophysicists.

2.3.3. Blueshift measuring techniques

Both the line asymmetry and differential central shift can be utilized to trace the convective velocity field inside the stellar photosphere. A single, high-resolution spectral line bisector traces convective velocity through the photosphere by its optical-depth dependent contribution function. The line core behaves similarly and, if measured for a large number of lines with differing central depths, can be used to trace velocity through the photosphere as well, with much lower requirements on data quality (Gray 2010b). Using both approaches simultaneously allows the so-called flux deficit due to the opposing contributions from rising and sinking material to be studied.

2.3.3.1. High-resolution techniques: Line bisectors

One commonly used method to determine the CBS is the line bisector. It is a curve connecting the midpoints of a spectral line along points of equal absorption depth in the red and blue wing. For cool stars the bisector commonly shows a distorted "C" shape, as

shown in the right panel of Fig. 2.1 for a solar Fe I line from the [Reiners et al. \(2016\)](#) solar atlas. The foot of the "C," the core of the line, is formed high up in the atmosphere in the overshoot region where convective velocity has decreased significantly. Further up in line flux the contribution function shifts its maximum to higher optical depths with higher convective velocities, forming the bulging part of the "C" shape. At the top of the wings the intergranular contribution becomes significant and adds a redshifted component, counteracting the granular component, which is decreasing in flux. This turns the bisector back toward lower blueshift, completing the "C" shape, as detailed for example in [Dravins et al. \(1981\)](#) or [Cegla et al. \(2019\)](#). This "curve-back" is also known as the flux deficit and symbolizes the difference between a pure granular or third-signature model (see Sect. 2.3.3.2) to the actual bisector. In effect, the flux deficit extracts and quantifies the intergranular contribution ([Gray 2010b](#)). Figure 2.1, in the left panel, shows as an example one line from the extremely-high-resolution, $R \sim 1\,000\,000$ solar spectrum used in this chapter. A Gaussian model profile on the right demonstrates the third-signature model we created (Eq. 2.1). The contribution of the intergranular lane is not within the scope of this work.

Properties of these bisectors have been used by various groups (e.g., [Queloz et al. 2001](#); [Cegla et al. 2019](#)) to characterize the strength of convection, the presence of starspots, limit the RV jitter and, by selecting the lowest region of the bisector, the convective line shift ([Dravins et al. 1986](#)). It can also be used to delineate the so-called granulation boundary that separates stars with an outer convective envelope from radiative ones. This happens around early-F types on the main sequence with the bisector first loosing the C-shape, straightening out, and then reversing shape ([Gray & Nagel 1989](#)); a process that has been closely examined in [Gray \(2010a\)](#) and could be explained with a shift in location along the wing of the flux deficit.

Using the bisector to determine convective shifts has the advantage that only a handful of lines or even single ones are sufficient to provide an accurate representation of the convective profile. The disadvantages are that it is particularly sensitive to blended lines and line distortions. It also requires spectral lines to be of very high resolution ($R \gtrsim 300\,000$) and high signal-to-noise ($S/N \gtrsim 300$) ([Dravins 1987](#)); otherwise, line asymmetries might be smeared out from the wider instrumental profile or lost in noise and photon binning.

2.3.3.2. Low-resolution techniques: Third-signature scaling

In this chapter, we expanded on a technique to measure the CBS of stars with spectra of a much lower resolution of $R \sim 100\,000$ and comparatively low S/N , typically at ~ 500 for our data, though S/N as low as 100 are sufficient (Sect. 2.10). The technique is significantly less demanding compared to single-line bisector analysis and applicable to stars spanning spectral types late-F to early-M. This was achieved with an extremely-high-resolution solar Fourier-transform-spectrograph (FTS) spectrum that was used to create a high-quality template for the magnitude of CBS. This CBS template was scaled to match measurements from lower-resolution, lower- S/N stellar spectra to obtain a relative CBS

strength. The backbone of this approach is the switch from individual line bisectors to many lines' core shifts, which allows for the accuracy of ultra-high-quality data in the form of an empirical template combined with the greater availability of lower-quality data. This technique hereby takes advantage of two key properties of CBS.

The first advantage comes from utilizing the central shifts for lines of different depths, ideally of the same element and ionization state to avoid additional degrees of freedom, as a tracer for the CBS (Hamilton & Lester 1999). This enables the usage of a much larger sample of lines, especially for fainter stars with generally insufficient levels of S/N for the bisector technique. The relation between the central line shift and line depth is commonly referred to as the "third signature of granulation", with the first and second being the line broadening due to macro-turbulence and the line asymmetry, respectively (Gray 2009). This is of further use if the goal is extreme-precision stellar RV determination using line-by-line measurements. Here, the selection of lines becomes important since different lines, through their different depths, have different intrinsic shifts that also change between stars (Cretignier et al. 2020).

The second advantage of the third-signature technique, when applied to multiple stars, is that it is capable to supply additional information. While the absolute values of CBS of the line cores will change from star to star for similar absorption depths, the basic shape of the third signature is universal (Gray 2009; Gray & Oostra 2018), except for stars above the granulation boundary (around spectral type F0 on the main sequence, just above 7000 K; cooler post main sequence)(Gray 2010a) where the flux deficit, or intergranular lane contribution, deforms the middle part of the third signature instead of the top toward redder shifts. The third signature can be matched between different stars by scaling and shifting the velocities and hence allows a relative convection strength to be determined from the scaling and a relative RV from the shift. To create a template on which to base the signature matching and to provide reference values for blueshift and RV, a single high-resolution, high-S/N spectrum, in our case from the Sun,

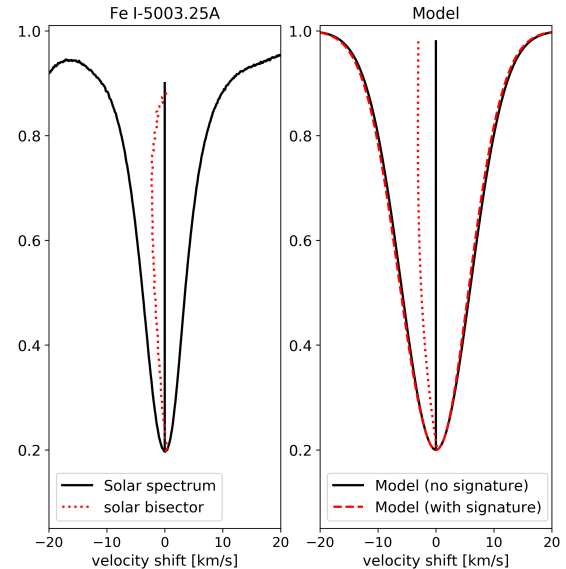


Figure 2.1.: Comparison of a solar and a model spectral line bisector. Left: Solar Fe I line at 5003.25 Å (solid black) with its center marked by a vertical line (solid black) from the IAG solar flux atlas (used as a template in this chapter) and the corresponding line bisector (dashed red). Right: Gaussian model line profile without (solid black) and with a solar-like third signature (dashed red, following Eq. 2.1). Their respective bisectors are shown in the same colors. The model with the signature is shifted to match the line cores. In both panels, to emphasize the slight blueshift, the bisector scale is amplified by a factor of ten.

is sufficient. The derived template for the third signature of granulation is then shifted and scaled to match the data from the other stars. Measuring CBS this way increases the robustness for a given data set due to the much lower requirements on resolving power (Sect. 2.10), the ability to more easily use coaddition to increase the S/N, the generally lower requirement on S/N (Sect. 2.10), and the reduced possibility of third-signature fitting errors due to the exact shape being empirically prescribed instead of assumed or simplified. In turn, this requires much greater care in the definition of the template signature because all uncertainties will be amplified through all other stars' analysis, necessitating the use of FTS solar data rather than HARPS standard stars.

2.4. Data

2.4.1. HARPS stellar data

This chapter is based on data obtained from HARPS, a fiber-fed, cross-dispersed echelle spectrograph installed at the 3.6 m telescope at La Silla, Chile. The instrument itself is housed in a temperature stabilized, evacuated chamber, and covers a wavelength range from 380 nm to 690 nm at a resolving power of $R=115\,000$ over 72 echelle orders. It is capable of reaching a precision of $1\,\text{m s}^{-1}$ (Mayor et al. 2003). The data were composed by Trifonov et al. (2020), who collected and sorted through all publicly available spectra from the HARPS spectrograph.

The full sample consists of 3094 stars. Out of that number, 439 were excluded because they had no matching counterpart in GAIA DR2 (Gaia Collaboration 2018) and 458 were identified as subgiants. The subgiants were excluded to be investigated in more detail in the next chapter. The method used in this chapter (Sect. 2.5) at HARPS resolving power further restricts the usage to stars with a projected rotational velocity of $v \sin i < 8\,\text{km/s}$ (Sects. 2.10, 2.10), which excluded all stars above 6250 K. We used $v \sin i$ values from SIMBAD and Glebocki & Gnacinski (2005) as well as HARPS DRS FWHM values listed in Trifonov et al. (2020) as proxy to exclude stars that did not meet this criterion. Filtering also stars of unknown $v \sin i$ left 810 stars in our final sample for analysis, that span the range from

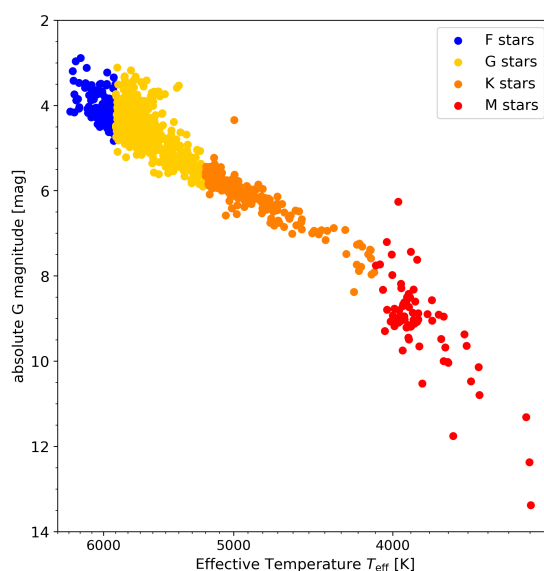


Figure 2.2.: Hertzsprung-Russell diagram of the 810 stars in the HARPS sample, based on GAIA DR2 data.

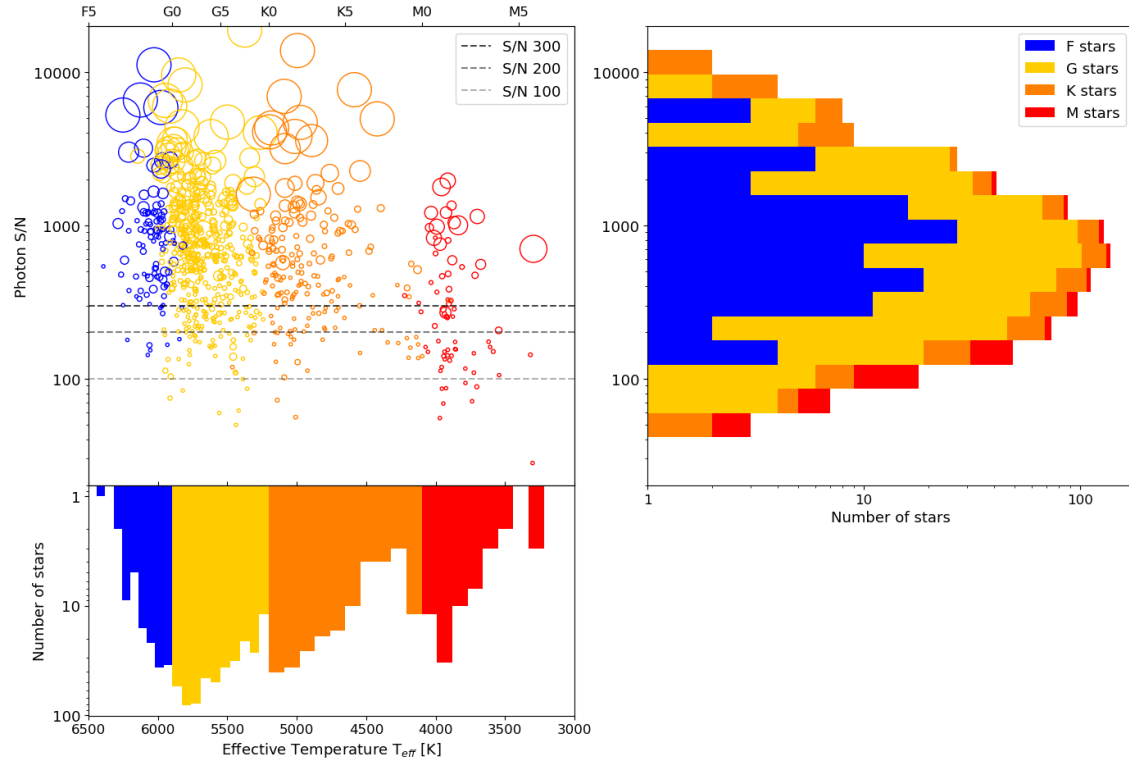


Figure 2.3.: Overview of all sample stars’ signal-to-noise ratio (S/N), temperature, and spectral type. Top left: Distribution of S/N over spectral type within the sample. The marker size corresponds to the number of observations for that star. The M stars show significantly smaller S/N with median below 300 due to both smaller intrinsic brightness and lower average number of coadded spectra. The dashed, horizontal lines mark S/N values of 100, 200, and 300, motivated by the results from Sect. 2.10. Top right: Peak S/N for the coadded spectra in the sample. Bottom left: Distribution of spectral types within the sample.

early-M to late-F types. The location of the 810 sample stars on the Hertzsprung-Russell diagram, based on GAIA DR2 data, is shown in Fig. 2.2.

Trifonov et al. (2020) coadded and analyzed the spectra for each star using the “SpEctrum Radial Velocity AnaLyser” (`serval`, Zechmeister et al. 2018), corrected for nightly offsets, and provided an overhauled RV data set. We used the high-S/N, coadded, template spectra, created by the `serval` pipeline for its template matching approach to RV determination, as well as the final radial velocities. During coaddition, `serval` further corrected any long-term trends in RV, such as binary motion.

The `serval` coadded spectra are given in vacuum wavelength and were converted by us to air wavelengths following the method from Ciddor (1996) as given in Husser et al. (2013). This is necessary because the line-sets’ wavelengths are given in air (Sect. 2.5.2). The S/N ratios obtained by `serval` from the coaddition of the spectra are shown in Fig. 2.3 in the top panels for each star individually (left) and binned by S/N (right, stacks colored to reflect spectral type). On average, 66 spectra were used per coaddition for an

approximate S/N just below 570, with some stars significantly higher. The lower panel of Fig. 2.3 shows the sample size, binned roughly by spectral subtype approximated by and plotted in temperature. The actual spectral subtype used to determine temperature-bin edges was approximated with GAIA (BP-RP) colors, converted to SDSS (g-i)¹⁶, and then interpolated following Covey et al. (2007). The sample misses some late-K type stars and very-high-S/N M-types. The latter is unsurprising due to the low intrinsic brightness of those stars and the former a known deficiency in classical spectral typing that leads to the subtypes of K8 and K9 to be virtually nonexistent. Despite this, the sample is continuous in temperature. A complete list of the stars from the final sample with their parameters can be found in Table 2.5 (full version available at CDS).

2.4.2. IAG solar data

To create the high-precision third-signature model required for the HARPS scale factor determination, we used the IAG solar FTS atlas¹⁷ (Reiners et al. 2016). With a spectral range of 405-2300 nm it covers the entire visible range and, most importantly, the entire range of HARPS data used in this chapter, enabling the use of matching line lists. The solar spectrum was recorded with an FTS over 1190 scans in the VIS range at a resolving power of over $R \sim 1\,000\,000$, exceeding HARPS data by an order of magnitude. This extreme data quality ensures we are only limited by the algorithm itself, variabilities intrinsic to the stars, and remain independent of any specific model assumptions.

2.5. HARPS data processing

To measure the CBS, we normalized the continuum of the spectra and created a preliminary list of spectral lines we used for the third-signature fit. The absolute stellar RV was obtained from the Trifonov et al. (2020) RVBANK as a reference. In an iterative process the preliminary line list and RV were further refined.

2.5.1. Boundary fit

The first step in measuring CBS is to normalize the continuum level, correcting for three effects: The instrumental blaze function, the gradient from the blackbody spectrum, and molecular bands for cool stars. We assumed that both the blackbody contribution and molecular bands could be neglected within single diffraction orders compared to the blaze function. To remove the latter and normalize the continuum, an upper boundary fit was employed, generally following Cardiel (2009); however, we used a squared sine-cardinal

¹⁶https://gea.esac.esa.int/archive/documentation/GDR2/Data_processing/chap_cu5pho/sec_cu5pho_calibr/ssec_cu5pho_PhotTransf.html

¹⁷http://www.astro.physik.uni-goettingen.de/research/flux_atlas/

function to mimic the blaze function. This differs from the usual approach of binning the spectrum within an order by wavelength, estimating a maximum as the local continuum, and interpolating the binned continuum levels. This approach, while functional, is highly susceptible to nonlocal spectral features, for example absorption bands, as well as emission lines, relies on a good choice of interpolation, and neglects previous knowledge about the continuum shape. The cost function, again generally following Cardiel (2009), was minimized with a Nelder-Mead simplex algorithm implementation from the python package `scipy.optimize.minimize`. To account for strong absorption (e.g., Na-D) and strong emission lines (e.g., Ca H+K), the algorithm presented by Cardiel (2009) was modified to further include an asymmetric kappa-sigma clipping on the residuals to exclude such influences. Lastly, by definition of the boundary-fit algorithm, some valid data points still lie above the fit as the fit is only pushed toward the boundary through asymmetric weighting of the residuals, not onto the actual boundary. Therefore, after normalizing the order first with the fit, those points were assumed to represent the true continuum and the entire order was normalized accordingly. An example for one echelle order is given in the Appendix in Fig. 2.23 to illustrate the fit and normalization result.

2.5.2. Line selection

The line list for the third-signature fit must contain lines that are present in all stars from spectral type mid-F to early-M. This ensures that the results remain comparable among themselves and against other choices of lines. The initial lists of atomic and molecular lines were taken from the "Vienna Atomic Line Database"¹⁸ (VALD; Piskunov et al. (1995); Kupka et al. (2000); Ryabchikova et al. (2015)). The parameters that were used are listed in Table 2.1. From the extracted lists we selected only lines with an absorption depth of at least 10%. Furthermore, only lines with a distance of at least 1 picometer to their nearest neighbor were selected. This was enforced by an iterative process that always kept the deeper member of the closest line pairs until all remaining lines were sufficiently separated. In this we assumed that line blends, averaged over all lines, did not significantly affect our results. We investigated possible effects from this by comparing average deviations between measurements in wavelength regions containing more or less blended lines. Fits of the CBS in either case do not show significant differences, indicating line blends are not an issue in this instance. This matches findings by Gray (2009), that line core measurements are much more robust against blends compared to bisectors. They further mention the possibility that the cores of very deep lines may no longer probe the photosphere, but instead reach the chromosphere with its wealth of NLTE and magnetic effects. Our analysis does not find qualitative differences in the scaling behavior of lines up to depths of 0.95, extending Gray (2009) findings by about 0.2 units in depth.

The final reduction of the line list took place after one full analysis run was completed, following the steps outlined in the rest of this section and the main analysis steps given in Sect. 2.7. This step was implemented to further remove lines that appeared more

¹⁸vald.astro.uu.se

Table 2.1.: Parameters used for the VALD extract stellar query.

T_{eff}	$\log g$	v_{mic}	composition	range
3750 K	5.0	1 km s ⁻¹	solar	4000-10000 Å
4500 K	4.5	1 km s ⁻¹	solar	4000-10000 Å
5500 K	4.5	1 km s ⁻¹	solar	4000-10000 Å
6000 K	4.5	1 km s ⁻¹	solar	4000-10000 Å

sensitive to measurement errors, based on the consistency of their results over all stars. Details on this process are given in Appendix 2.10. The line lists for different effective temperatures were compared via their results to ensure the choice of temperature did not affect the results significantly (Section 2.8.1). The prescribed temperature shows no significant impact and the main analysis was based on the 3750 K line set, which, after refinement, comprises 1256 remaining lines, an order of magnitude above the lists used by other groups, for example Meunier et al. (2017b).

2.5.3. Telluric contamination

Besides line blends, contamination by telluric absorption lines can impact the accuracy of line core measurements. We used the atmospheric transmission spectrum included in the ENIRIC package (Figueira et al. 2016), based on TAPAS synthetic spectra (Bertaux et al. 2014), to determine bands of potential contamination and assessed their impact on our overall results. Out of the finalized list of lines, only 6% are in danger of contamination, the majority of them along with the potentially strongest contaminated ones are located toward the red end of the HARPS wavelength range. Similar to line blends, we find no dependence of line scatter on wavelength and excluding the telluric bands does not improve our results. Comparing residuals of the lines in question to lines of similar depth outside the telluric bands again shows no significant differences. From this we determine that telluric contamination can be neglected and continued with the complete reduced line set.

2.5.4. Initial radial velocity

The serval pipeline coadds the spectra using differential RVs. In addition to the values from the HARPS RVBANK, we measured the absolute RV of the coadded spectrum using a binary line mask from the CERES pipeline (Brahm et al. 2017)¹⁹. This mask is based on an M2 star. We cross-correlated the box function created from the wavelengths and weights from the CERES mask with the spectrum utilizing the `scipy.signal.correlate` package, each with their mean subtracted beforehand, and normalized with the integrated area of the box-function. This cross-correlation function (CCF) is calculated

¹⁹https://github.com/rabrahm/ceres/tree/master/data/xc_masks

for each order of the coadded spectrum of each star, represented with a cubic spline interpolation, and sampled on a common velocity grid using `scipy.interpolate.splrep/splev`. The CCFs were averaged over the orders and the minimum determined using a fourth order `InterpolatedUnivariateSpline` again from `scipy.interpolate` and its `derivative.roots` function within $\pm 500 \text{ km s}^{-1}$. This position was taken as the initial RV.

2.5.5. Measuring line positions

As an initial RV guess we used the cross-correlation and RVBANK value. The `serval` coadded spectrum of each star was shifted accordingly and the reduced list of lines from Sect. 2.5.2 applied as initial line positions. The rest of the chapter used the CCF RV correction with the RVBANK values used as validation. Following Reiners et al. (2016), a parabola was fitted within $\pm 1500 \text{ m s}^{-1}$ to the line core and its minimum taken as the center of the line. We refitted the parabola with the new line center until convergence was reached (10^{-5} nm correction step) in case the initial position was too far from the line core. The final minimum was taken for the line position and absorption depth. The precision in depth, following Sect. 2.10, is on the order of $7 \cdot 10^{-3}$, while Sect. 2.10 shows a shift accuracy of better than 40 m s^{-1} for single lines. If the fit got stuck in a local maximum, for instance from remaining blends or insufficient RV correction, the last step was repeated with increasingly larger steps away from the maximum added to the last position. Very large steps between iterations were bounded to 1 pm to prevent fitting errors in shallow, noisy lines that could point the assumed center at far distant wavelengths. Finally, remaining blends that pushed measurements of two lines into the same minimum were taken to be primarily composed of the lesser shifted component with the other removed from the results. Duplicate measurements due to echelle order overlap were averaged in location and depth.

2.5.6. Refining radial velocity

As a last step, the RV was further refined by utilizing the correlation of absorption depth with CBS. Using only the CCF based RV from Sect. 2.5.4 or RVBANK value, a first determination of the CBS was done from the line-by-line RV from Sect. 2.5.5. Since the deepest lines are barely affected by CBS, lines with an absorption depth above 0.9 were then binned in depth and their median RV added to the result from the previous step. Since these lines should show close to zero CBS due to their low depth of formation, they are a good indicator for the overall RV. This cycle of applying RV, measuring CBS, and reevaluating the RV from the deepest lines was repeated until convergence. This additional step was necessary because many lines included in the list are very narrow and therefore require a very good RV correction in order for the initial starting point of the measurements to still lie on their wings and not get shifted to a neighboring line. Using the deep lines to determine the RV is a simple and robust approach.

2.6. Modeling the solar third signature

Before we calculated our third-signature solar template, we first ensured the accuracy of our line center determination. We recomputed the third signature of granulation for the Sun using the list of Fe I lines from [Nave et al. \(1994\)](#), compared the results to [Reiners et al. \(2016\)](#), before the fit was repeated using our custom line list as explained in Sect. 2.5.2.

We followed the general procedure from [Reiners et al. \(2016\)](#): We first measured the line-by-line CBS as the difference between the measured line position and the tabulated rest position. Then the shifts were median-binned by absorption depth and the bin dispersion was characterized with the median absolute deviation (MAD) from `astrophy.stats.mad_std` (Fig. 2.4). The error of the bin median was derived from dividing the MAD by \sqrt{N} , with N the number of lines in the bin, analogous to the standard error of the mean. This accounts for the significantly higher bin dispersion as opposed to the formal uncertainties on the line shifts. The binned data were fitted with a cubic polynomial, similar again to [Reiners et al. \(2016\)](#), using the `scipy.optimize.curve_fit` function in Levenberg-Marquardt mode. This algorithm was used for all other fits as well, unless specifically stated otherwise, and further provided the uncertainties on the fitted parameters.

We assumed the following constraints on our fit: The shallowest lines have formed deep enough inside the convection zone for the velocity to be constant. Hence the third signatures' gradient at zero absorption depth was set to zero, eliminating the linear term. Furthermore, we assumed that within the convection zone the velocity only decreases toward the surface. To that end, we ensured a nonnegative gradient of the function. In practice, this led to a quadratic term that approached zero and it was eliminated as well. These assumptions were enforced to remedy a local minimum in the shallowest lines that occurs in [Reiners et al. \(2016\)](#). This would indicate an outward directed increase in convection velocity, which should only happen at the bottom of the convection zone, far below the line forming region. Our physically motivated constraints avoid this numerical artifact. The resulting polynomial $v_{\text{conv},\odot}(d)$ for the [Nave et al. \(1994\)](#) line list is given in Eq. 2.1.

$$v_{\text{conv},\odot}(d) = 694.325 \cdot d^3 - 518.419, \quad (2.1)$$

$$v_{\text{conv},\odot}(d) = 601.110 \cdot d^3 + 173.668. \quad (2.2)$$

The template third signature of granulation used for the remainder of this chapter was created in two steps: First, we created a base template from full-resolution FTS measurements. Second, the base template was calibrated to the resolving power of the target instrument, in this instance HARPS.

The first step is identical to the approach to Eq. 2.1, switching from the [Nave et al. \(1994\)](#) to the VALD line list, while the later follows Sect. 2.7. It is necessary to account for

the changes in observed line depth introduced through broader instrumental line shapes at lower resolving powers if one expects solar-strength convection to be represented by a solar-relative factor of one or intends to compare results from spectra of different resolving powers. As a relative measure of convection strength using a single instrument, the later step can be skipped. The reason we did not use the iron list from [Nave et al. \(1994\)](#) for the rest of this chapter, though it agrees well for the solar Atlas, is because it was compiled specifically for the Sun and did not provide satisfactory results for stars of different spectral types. While our list still mainly consists of Fe I lines, they are more numerous and diverse, avoiding the over-adaptation to the solar case.

Equation 2.2 gives the base template from the first step, created from very-high-resolution FTS data. We degraded the FTS spectrum to a resolving power approximating 110,000 and performed a fit of the base template that results in calibration values of 0.91 in scale and 21.2 m s^{-1} offset. These corrections were implicitly applied for the remainder of this chapter, whenever the template is mentioned. Additional corrections for different resolving powers can be taken from Fig. 2.21.

Figure 2.4 shows the line measurements using the solar atlas data for the [Nave et al. \(1994\)](#) lines, the binned results, and our fitted polynomials. We confirm our re-computed third-signature template largely matches the results from [Reiners et al. \(2016\)](#) for their line list, except for their local minimum at approximately 0.3 line depth. The signature based on the VALD list deviates for deeper lines and shows a shallower overall shape from the difference in selected lines compared to our fit to the [Nave et al. \(1994\)](#) lines. The [Reiners et al. \(2016\)](#) signature appears slightly steeper. The $R \approx 110,000$ calibrated template is slightly shallower still, as indicated by the smaller than unity calibration factor, clearly demonstrating the necessity of this step for comparable results. The scatter in this work appears slightly smaller on average compared to the results from [Reiners et al. \(2016\)](#) but slightly larger toward the shallower lines.

For the template signature used in the remainder of this chapter, the calibrated, VALD based one, another offset of 726 m s^{-1} was subtracted in all illustrations to adjust the signature such that a fully absorbing line of depth 1.0 corresponds to a CBS of

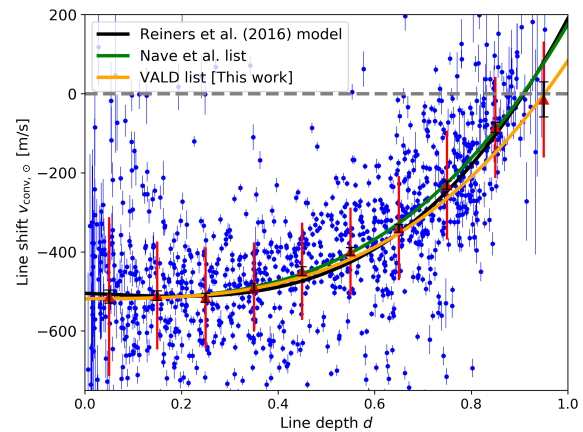


Figure 2.4.: Third signature of granulation extracted from the IAG solar flux atlas. Blue dots with error bars mark the lines measured using the [Nave et al. \(1994\)](#) list, red triangles with bars are bin medians with MAD, black error bars show the error of the median. The black line is the model for the solar third signature from [Reiners et al. \(2016\)](#) based on the [Nave et al. \(1994\)](#) line list and the green line is the model from this chapter (Eq. 2.1) based on the same. The orange line is our VALD-lines based template (Eq. 2.2), shifted to match the intersection of the other two models at depth 0.15.

zero. The reasoning is identical to the residual RV correction from Sect. 2.5.6 and purely cosmetic to make comparisons between panels easier. The origin of this offset is primarily the solar gravitational redshift of 636 m s^{-1} . The remainder is due to the theoretical, fully absorbing line we used as a reference being deeper than the median line used for the 636 m s^{-1} determination.

The remaining scatter can be seen for example in [Reiners et al. \(2016\)](#), [Hamilton & Lester \(1999\)](#), and [Allende Prieto & Garcia Lopez \(1998\)](#), although they used equivalent widths instead of line depths, [Meunier et al. \(2017b\)](#), and [Meunier et al. \(2017c\)](#). A possible correlation with wavelength was explored in, for instance, [Dravins et al. \(1981\)](#) or [Hamilton & Lester \(1999\)](#), although [Allende Prieto & Garcia Lopez \(1998\)](#) disagree with their conclusion. Our investigation into that topic using the present solar data shows a strong decrease in CBS toward longer wavelengths at similar absorption depths (see Appendix 2.10). The dispersion visible for lines deeper than ~ 0.7 is fully explained this way (Fig. 2.17), with shallower lines showing additional dispersion.

2.7. Third-signature fit for the HARPS sample

We followed the same procedure as the second step of the template creation from Sect. 2.6 for the VALD line list to fit the solar template to the HARPS measurements. The line list from Sect. 2.5.2 was applied to each coadded spectrum for each of the stars in the HARPS sample. Then, the line-by-line measurements of v_{conv} were median-binned by depth d and fitted with the template signature from Eq. 2.2 as $v_{\text{conv}} = S \cdot v_{\text{conv},\odot} + v_0$, using a scaling factor S and velocity offset v_0 . The shallowest and deepest bin were excluded (see Fig. 2.5). Uncertainties were provided by the fitting algorithm. From the two parameters only S is of further relevance in this chapter since it encodes the strength of the CBS relative to the Sun. The shift, an RV on the order of a few m s^{-1} and comparable in magnitude to the scatter intrinsic to each stars measurements, is an offset inherent in all lines and therefore unrelated to CBS, which operates on a differential, line-by-line basis. It is therefore assumed to be an uncorrected residual from the RV correction and subtracted from each star for all subsequent plots to provide a common velocity zero point.

In the next sections we describe the results of applying the solar third signature of granulation template to the HARPS sample of 800 stars. The results are plotted in Fig. 2.5 for one sample star each for spectral types late-F, mid-G, early-K, late-K, and early-M as well as the Sun for comparison. These stars were selected based on their fitted solar relative scale factor, from now on referred to simply as scale factor, in order to evenly span the range available from the sample and to illustrate the gradual change in third signature with spectral type. The full list of scale factors for each star are tabulated in Table 2.5, available at CDS, and plotted in Fig. 2.6, showing the gradual increase with effective temperature. The solar panel differs from Fig. 2.4 in that here the VALD filtered list and corresponding template were used, not the Fe I list from [Nave et al. \(1994\)](#), as well as the broadened FTS spectrum.

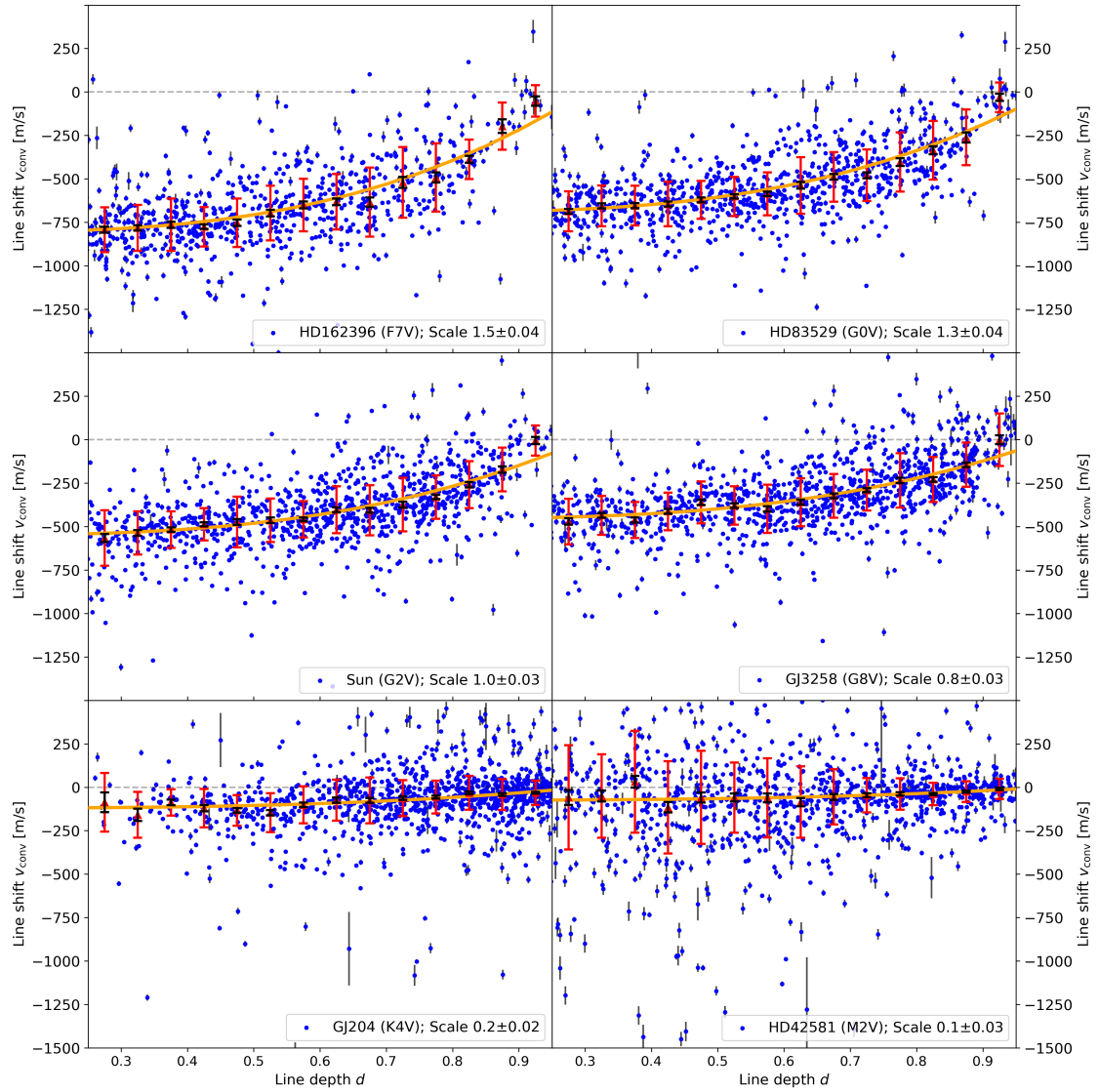


Figure 2.5.: Example third-signature plots derived from HARPS data and solar FTS, convolved to $R=110000$, for spectral types ranging from F7V (top left) to M2V (bottom left), chosen to sample the scale factor range. Shown are shifts v_{conv} for individual lines (blue circles) and results binned by line depth (red triangles with error bars for MAD, black for the error of the median). The best-fit, scaled, solar third signature is shown (orange curve, fitted through the red markers).

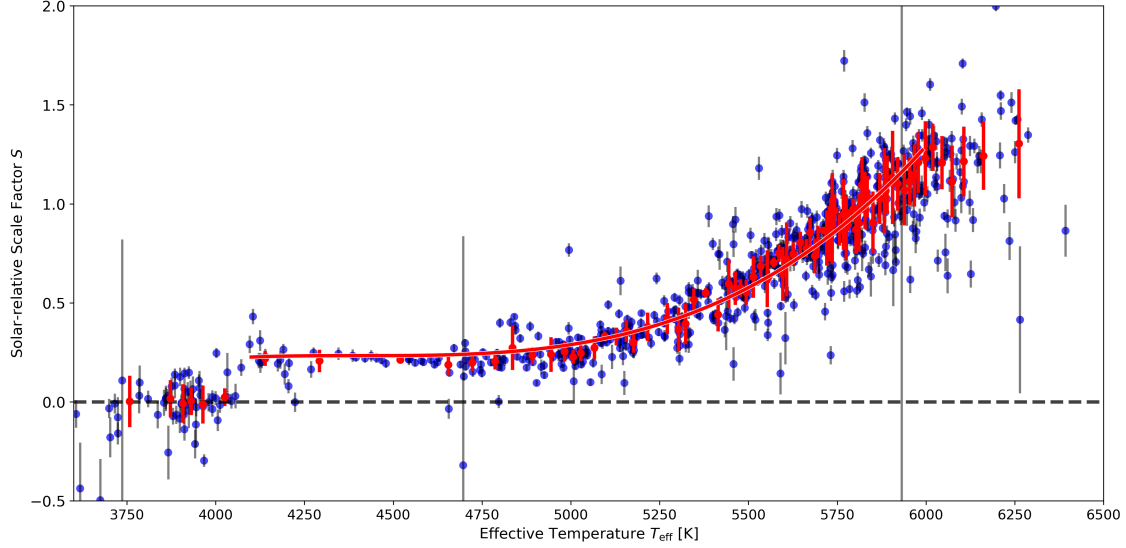


Figure 2.6.: Solar relative scale factor for all main sequence stars in the set (blue circles) plotted against their respective effective temperature. Bins with ten stars each (red circles with error bars) are fitted with a cubic polynomial (red curve, Eq. 2.3).

2.7.1. F, G, and K stars

The results for the F, G, and K dwarfs are shown in Fig. 2.6 where there is a strong, increasing dependence between scale factor and effective temperature, which could also be seen in Fig. 2.5. The main sequence stars increase steeply in scale factor for hotter stars, flatten toward early K-types, and plateau for later K-types. To quantify this relation, the scale factors for the main sequence stars were median-binned by temperature, with the error of the bin median obtained from the MAD as in Sect. 2.6. The binned data were fitted with a cubic polynomial of the form:

$$S(T_{\text{eff}}) = a \cdot \left(\frac{T_{\text{eff}} - 4400 \text{ K}}{1000 \text{ K}} \right)^3 + b. \quad (2.3)$$

The best fit is shown in Fig. 2.6 and the parameters are given in Table 2.2. Table 2.4 lists the fitted scale factors for specific spectral subtypes and corresponding blueshift velocities.

It must be noted that the HARPS sample, despite the calibration of the third-signature model with the values determined in Sect. 2.6, still shows a $\sim 6\%$ smaller CBS at solar temperatures in the fit ($S(5800\text{K}) = 0.94$) than expected. This matches the results from [Meunier et al. \(2017b\)](#), who also see a roughly 6% difference. A comparison to multiple months of HARPS-N Sun-as-a-Star observations ([Dumusque et al. 2021](#)) also show an average scale factor $\sim 5\%$ below unity after calibration. Section 2.8.2 demonstrates that deviations of 10% can be reached by activity influence of sufficient strength and the scatter in the HARPS-N solar observations includes unity within one standard deviation. For

Table 2.2.: Coefficients for the $S(T_{\text{eff}})$ polynomial fit to the solar-relative scale factors over effective temperature, following Eq. 2.3.

List	a	b
all lines	0.265	0.254
refined lines	0.258	0.233
4500 K lines	0.264	0.254
5500 K lines	0.259	0.260
6000 K lines	0.261	0.264

Notes. "All lines" refers to the full list of lines as taken from VALD, only cleaned of too shallow and too close entries (first part of Sect. 2.5.2). The "refined lines" list is cleaned of those lines that do not give consistently good results (second part of Sect. 2.5.2). The other three are subsets of lines that are also included in cleaned VALD list for stars of the corresponding effective temperature.

this reason it is likely that the FTS spectrum that was used in this chapter corresponds to a time of higher observable CBS, explaining the Sun-as-a-Star results showing an average blueshift smaller than that, as opposed to an error in our measurements. This is compounded by higher activity in our HARPS sample compared to the Sun that depresses the average CBS values at solar temperatures. As the breadth of scale factors visible at solar temperatures in the HARPS data is mirrored in solar observations, this seems to further indicate an intrinsic noise floor for CBS determinations (see Sect. 2.8.2 for details).

Previous studies into CBS have not been able to find the plateau spanning roughly from 4100 K to 4700 K. This is due to them having no stars in this temperature range (Meunier et al. 2017c), having low, single-digit numbers (Gray 2009), or, with synthetic data, only examining a very narrow slice in temperature (Chiavassa et al. 2018). As the first study with the required number of stars to cover that range available, we were able to find and report the plateau for the first time. Similarly, the step at 4000 K could not have been found by previous studies for the same reasons.

2.7.2. M stars

Only one M star is shown in Fig. 2.5, which was of very early M type and shows a scale factor slightly above, but consistent with, zero. Looking at all the M-stars available in Fig. 2.6 suggests a CBS of zero, or close to it, in M stars starting at a temperature of 4000 K. This disagrees with the hypothesis from, among others, Kürster et al. (2003) for Barnard's star. They suggest an increase in CBS with increasing plage area, indicating the underlying convective pattern that is magnetically suppressed is producing convective redshift. They provide a possible explanation, based on M-dwarf convection models from Ludwig et al. (2002), in that the decrease in contrast between granules and lanes, combined with a change in vertical flow velocity could lead to a sign change in the balance between granular and intergranular line profile contribution. Our sample includes Barnard's star, though

it was initially rejected for unknown $v \sin i$, and its measurements show a scale factor of -0.15 ± 0.08 , matching the approximation from Kürster et al. (2003), where the convective redshift would be on the order of 33 m s^{-1} , about -0.1 in scale factor. This is, however, on the order of the scatter in our results for earlier M stars, while the scatter for mid-M type could not be characterized due to a lack of usable stars. This uncertainty in the actual strength of convective shift is also seen in findings from Baroch et al. (2020), where they measure the CBS of the M dwarf YZ CMi using the chromatic index and RV variations over one rotation period to model spot and plage distributions. They find a convective redshift on the order of 7 to 237 m s^{-1} or -0.02 to -0.79 in scale factor, encompassing the supposed strength for Barnard's star.

A limitation of our results for M dwarfs is that they show comparatively low S/N, as previously shown in Fig. 2.3, decreasing scale factor accuracy, and show similar absolute scatter at smaller scale factors compared to solar-like stars at lower scale factors. The general trend does not support the redshift hypothesis and remains consistent with zero scale factor, an extension of the K-dwarf plateau after a relatively large step at 4100 K. Furthermore, including the reduced χ^2 of the third-signature fit as a size scale for the data points results in Fig. 2.24. Larger points here represent better fits and the points are color coded by S/N. The stars not disqualified for one of the aforementioned reasons still show the same behavior, consistent with zero scale factor for M-dwarfs. Looking at the earlier star sample similarly does not show significant changes, with the majority of stars indicating a good fit except toward the edges of the range, the hotter of which was showing higher scatter from the start.

In conclusion, our data suggests there to be no general switch to convective redshift for M dwarfs above 3600 K and generally no convective shift with $|S| > 0.1$. Convective blue- or redshifts above that mark would have been detected. We conclude that there is neither a red- or blueshift at temperatures cooler than 4100 K, roughly matching the K-to-M-dwarf transition.

2.8. Discussion

We developed a new technique to measure CBS that uses an empirical, ultra-high-resolution solar template of the third signature of granulation that was scaled to fit measurements from HARPS spectra of over 800 usable stars spanning from F to M spectral type. This scale factor is a robust representation of convection strength relative to the Sun and our results show a clear dependence on effective temperature.

In this section we discuss the effects of our choice of VALD extraction parameters, especially the temperature, the possible influence of stellar activity, and the lines lower excitation potential. A deeper look into the technical performance and limits of the algorithm is given in Appendix 2.10.

2.8.1. Line list effective temperature selection

To understand the influence of a 3700 K based line list, additional lists were extracted from the VALD database (see Table 2.1) for 4500 K, 5500 K, and 6000 K. To reduce computation time, the new lists, after a first vetting following Sect. 2.5.2 without the post-processing from Appendix 2.10, were checked against the original post-processed 3700 K one and only the reoccurring lines used each time. The fitted parameters for the polynomial function (Eq. 2.3) are given in Table 2.2. For each line list shown, the scale factor versus effective temperature relations are indistinguishable. Therefore, the choice of effective temperature for the line list does not have a significant impact. The same analysis was carried out for the solar data to check variations in the initial template with the same result.

2.8.2. Influence of stellar activity

The scatter in the resulting scale factors, as well as the solar templates' deviation from similar temperature HARPS stars as well as HARPS-N solar observations, may be due to different levels of activity between stars of similar spectral type or observation times. This can dampen or enhance CBS or higher activity levels could lead to an increase in noise levels, degrading CBS fit accuracy. To quantify this, we used the $\log R'_{HK}$ indicator values calculated by Boro Saikia et al. (2018) and Marvin et al. (2016, submitted), where we obtained $\log R'_{HK}$ values for 350 stars. In the case of stars with multiple values, we averaged the values. We further provide rotation periods where possible from Lovis et al. (2011) in Table 2.5. The results are color-coded for activity in Fig. 2.7 and listed in Table 2.5. A slight trend toward lower scale factors for higher levels of activity is visible. The absolute residual of the polynomial fit correlates with the activity indicator with a Pearson correlation coefficient of $r=0.02$ with a t-Value of 0.39 (p-Value ~ 0.7), indicating higher activity does not lead to higher scatter. Figure 2.8 shows the signed residual, which has correlation coefficients of $r=-0.32$ and $t=-6.24$. From this we conclude that higher activity inhibits CBS strength (p-Value $< 10^{-5}$). This supports the findings from Meunier et al. (2017b) and Meunier et al. (2017c) who published an

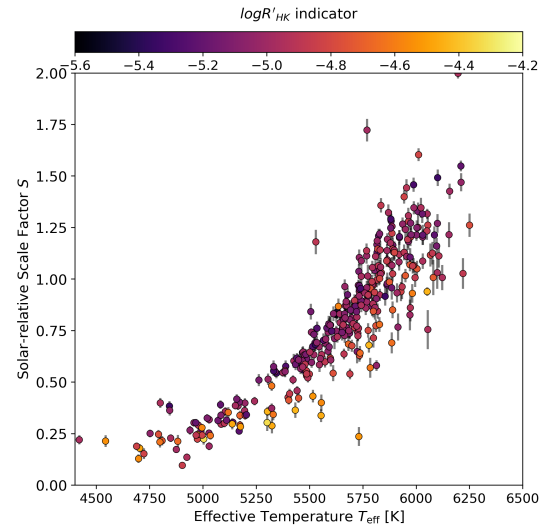


Figure 2.7.: Similar to Fig. 2.6 but color-coded with the activity indicator $\log R'_{HK}$. No relation between scatter and activity is readily apparent, but more active stars tend toward lower scale factors.

anticorrelation between CBS and activity. They further find a link from CBS to metallicity, which seems to provide a competing effect with higher metallicities correlating with smaller CBS at similar activity levels. The metallicity-activity dependence however goes the opposite: high metallicities correlate with lower activity levels, which correlate to higher CBS strengths. The reason for this discrepancy is unknown, though they postulate it might either be due to metallicity changes contaminating the $\log R'_{HK}$ determination or physical changes in the small-scale convection pattern. Inhibition of CBS through higher stellar activity is better understood (see e.g., [Bauer et al. \(2018\)](#)), as magnetic pressure in active regions counteracts convective motion and lowers the net blueshift.

These results do not explain the solar template deviation however. The solar FTS was recorded in 2014, before the HARPS-N observations and, according to sunspot numbers, during a time of higher solar activity ([SILSO World Data Center 2014-2018](#))²⁰. This should correspond to a lower level of CBS, the opposite to the observation. As solar activity in terms of $\log R'_{HK}$ varies very little (HARPS-N solar observations cover -4.96 to -5.04, about the average of the HARPS sample) this translates into negligible CBS suppression, eliminating activity as the source of the discrepancy. Coupled with the HARPS-N observations including unity within one standard deviation and showing strong dispersion even between observations taken on the same day, this indicates a CBS noise floor of $\sim 10\%$ for the Sun, irrespective of activity, and operating on the granulation timescale of ~ 10 minutes. This is in accordance with [Collier Cameron et al. \(2019\)](#), who also see intraday variations in the CCF BIS on the 10% level.

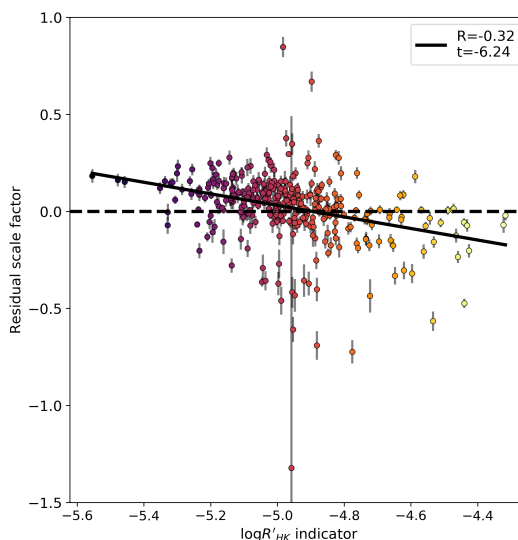


Figure 2.8.: Linear fit (black line) between signed residuals of the scale factor fit and the activity indicator (blue markers). Pearson r and Student t values are shown in the top right.

2.8.3. Influence of excitation potential

[Dravins et al. \(1981\)](#) reported a dependence of CBS on the lower excitation potential of the spectral lines. They postulated that higher temperatures in granules produce stronger excited lines, which then show a correspondingly higher blueshift compared to lower excited lines from intergranular lanes. In their Fig. 3 they showed a plot of excitation potentials for lines of intermediate depth against blueshift, which showed a highly scattered dependence. To investigate if this has any impact on the results obtained in this analysis,

²⁰<http://www.sidc.be/silso/>

we repeated their analysis by restricting our results to the same sample of Fe I lines on the solar FTS spectrum. We did not find any relation between CBS and excitation potential in our data, matching nonfindings by [Gray & Pugh \(2012\)](#) for giants and supergiants.

2.8.4. Comparison to other works

[Meunier et al. \(2017b\)](#) and [Meunier et al. \(2017c\)](#) utilized a simpler approach to measure the strength of CBS in the form of a linear model $v_{\text{conv}}(d)$ for the third-signature fit in place of a cubic polynomial scaled from a high-quality solar template (Eq. 2.2). It was carried out on a similar albeit smaller sample of HARPS observations that spans only 167 and 360 stars, respectively, and extends down to a temperature of 5000 K (4700 K), excluding the later K dwarfs present in this chapter. They also find a decrease in CBS, proxied in their work by the "Third Signature Slope" (TSS), with decreasing effective temperature, though their trend, as shown in Fig. 2.9, recreated from Fig. 5 in [Meunier et al. \(2017c\)](#) and normalized to solar values, appears linear unlike what our results based on Eqs. 2.3 and 2.2 suggest. Overlaying our results reveals a good, though slightly offset, agreement for stars at 5900 K and cooler but deviates strongly for stars above that. This may be explained by the fact that these weaker third signatures (scale factors < 1.0) have a smaller curvature and could be better approximated as linear without significant loss of precision. This no longer holds for stronger third signatures (scale factor > 1.0), where the curvature becomes stronger. In this case it is to be expected that a linear model underestimates the strength of the signature, especially since the shallower lines are still comparatively linear with a smaller slope and make up approximately 2/3 of the depth range before the signature curves up significantly. This is compounded by them only choosing a range of depths 0.4 to 0.8, excluding the deeper, much more curved, part of the third signature we have included in our model (up to depth 0.95). Switching our solar template for a linear model and restricting the fit to their depth range results in a qualitatively similar relation, though the very slight sigmoid shape inherent in their results appears much more pronounced, approaching the form of a logistic function. Differences exist for hotter and cooler stars, appearing as if our TSS results are compressed, and in our solar TSS (TSS_{\odot}), the linear slope of the template, which shows as 575 m s^{-1} instead of 776 m s^{-1} . A potential influence is the choice of line list, which can lead to significant differences if wide applicability is not kept in mind, similar to our rejection of the [Nave et al. \(1994\)](#) line list, which is over-adapted to the Sun. Another likely contributing factor to the deviations are the significantly changing ionization fractions of iron at temperatures above 6000 K. The ionization balance between Fe I and Fe II reverses around 6000 to 7000 K, reducing the vertical atmospheric range in which Fe I lines can form and therefore the contributing velocity components. Limiting those components to the cooler, upper parts of the atmosphere restricts the line contribution to lower velocities and one would expect a smaller observed CBS compared to lines that have a higher temperature flipping point in their species ionization fractions. Qualitatively, the choice between solar and linear template seems to be the cause of the difference in the hotter stars scale factors.

Our results are in agreement with the theoretical models of [Magic & Asplund \(2014\)](#) who predict an increase in convection velocity (and therefore CBS strength over all line depths) and granule brightness, hence a stronger CBS signature, for either hotter or lower surface gravity stars or both, which our results fully support. The increase in scale factor matches the theoretically expected small increase in granule size and significant increase in granule contrast due to increasing effective temperatures compounded by the contribution from the slightly decreasing surface gravity.

We also compare our results to the theoretical results of [Chiavassa et al. \(2018\)](#). Unlike [Meunier et al. \(2017b\)](#) they used purely synthetic spectra to measure CBS with cross-correlation techniques for a wide range of effective temperatures. Their resulting CBS also increases with effective temperature; however, their results appear to underestimate CBS on the parameter range above 5400 K by at least 100 m s^{-1} compared to our CBS values. The results roughly match below 5000 K, but are hindered by dispersion on the order of 200 m s^{-1} and discontinuous coverage. The data are instead clustered in narrow temperature slices. Accounting for those deviations, which they point out themselves, puts their results much closer to ours. The last major deviation is their predicted flattening of CBS for stars above 6000 K. This is potentially compatible with our results since our binned results show the beginnings of a plateau. A definite conclusion is hindered by the lack of usable stars hotter than 6200 K in our sample. As for [Meunier et al. \(2017b\)](#), it is also important to remember that the choice of spectral lines can have a large impact if generality is lost. Unlike in this chapter, [Chiavassa et al. \(2018\)](#) are using only Fe I lines and may be susceptible to the mentioned changes in ionization fractions. Therefore, comparisons of results above 6000 K, namely the plateau in the [Chiavassa et al. \(2018\)](#) data, are not applicable unless one were to also use only Fe I lines, which would not be representative for the stars' actual CBS. [Meunier et al. \(2017b\)](#), while not stating the actual lines they used, have based their list on a catalog of Fe II, on top of Fe I, taking care of that problem, while our list also includes some Fe II lines.

[Basu & Chaplin \(2017\)](#) present a mathematical approach to model observable CBS velocity amplitudes based on approximations for granule coverage and sizes using mixing-length theory and established scaling relations. We applied their results as a scaling relation and inserted stellar values from our sample, which roughly matches our results in

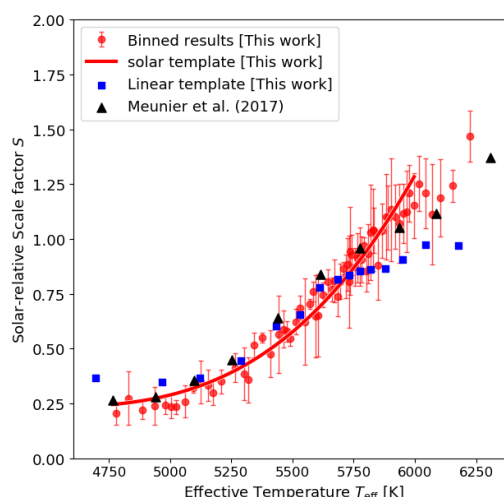


Figure 2.9.: Comparison of the results from [Meunier et al. \(2017c\)](#) (black triangles) with this work (red, solid line and red markers with error bars) and an alternate, linear template (blue squares).

general shape. Depending on where in our sample we calibrated the scaling origin to, it either matches the range 4700-5500 K or the 5400-6000 K, though not both. It also does not reproduce the K-dwarf plateau in either case. A likely cause is their assumption that individual granules contribute the same intensity fluctuations irrespective of spectral type and that the cancellation between granular blueshift and intergranular redshift is also independent of spectral type, which they call rather simplistic themselves. The scaling does predict a near-zero CBS starting at early M-stars for decreasing effective temperature, which is mirrored in our results.

2.8.5. Extending the data set

We show in Sect. 2.7.2 that our results on the convective shift of M dwarfs indicate zero CBS. We could not supplement our HARPS data using high-resolution, higher-S/N observations from the dedicated M-dwarf survey CARMENES ([Quirrenbach et al. 2016](#)), since the instrument does not cover the shorter wavelength range between 450 and 500 nm that a large part of the spectral lines used in this chapter fall into and the expanded red end compared to HARPS does not contain enough usable atomic lines to compensate. A revisit once more HARPS observations are available, increasing coadded S/N especially for later M-dwarfs, is expected to improve the situation.

Additional extension possibilities include stars above ~ 6000 K to observe convective shift behavior close to and above the granulation boundary, investigating claims by [Chiavassa et al. \(2018\)](#) of a plateau in CBS as well as the influence of changes in the ionization fractions. This would need either a sample of low $v \sin i$ F stars or a revision of the line-core fitting procedure.

Similarly, we are working on an investigation of a set of subgiant and giant spectra, extending the work of [Gray \(2009\)](#) toward understanding the CBS behavior of stars that left the main sequence.

2.9. Conclusion

Our new approach to measure CBS that used a ultra-high-resolution solar template applied to high-resolution stellar measurements, has proven to be robust over a large range of effective temperatures, from early-M to early-G or late-F spectral type or 3800 K to 6000 K. Further, we were able to determine limits in terms of S/N and minimal resolving power required to apply our technique, both of which are very reasonable in terms of instrumental requirements.

We used the template and a large sample of coadded HARPS main sequence star spectra to obtain the following results:

- We provide a revised model for the solar third signature of granulation based on an expanded list of lines that is also applicable to other stars, unlike previously used lists that were curated for the Sun.
- We confirm that CBS strength scales strongly with effective temperature above 4700 K and provide a fitted scaling relation. Unlike previous findings, our results scale with the third power of effective temperature. The discrepancy appears to be due to differences between our empirical and previous simplified third-signature models. They agree within the margins expected due to different line lists and said algorithmic differences
- We find that between 4100 K and 4700 K CBS remains constant at 23% solar strength. Previous studies do not sufficiently cover this region to make this determination.
- Between 4100 K and 3800 K, we find that CBS shows a sharp step down and appears to remain constant, though scattered, around zero observable CBS. The topic of CBS in M dwarfs has been highly debated and could not be definitely resolved.
- The preceding results prove the applicability of the third-signature fitting approach, shown by [Gray & Pugh \(2012\)](#) for giants, to main sequence stars, as indicated by [Gray \(2009\)](#).
- We confirm that stellar activity correlates with lower CBS, explaining part of the dispersion in our results.
- We could not find any dependence of CBS on a spectral lines lower excitation potential.
- We provide an expanded third-signature model for the Sun, taking into account wavelength in addition to line depth, demonstrating the strong effect the former has on CBS.
- We provide synthetic and empirically derived limits on our approach to determine CBS strengths as well as corrections to account for the effect of instrumental resolving power.

Further, the technique and its much more reasonable requirements on data quality compared to the classical bisector approach opens up the study of CBS to a significantly increased number of instruments and research groups. It also allows fainter stars, be it from distance or temperature, to be studied without the need to coadd dozens of spectra, reducing the required observation time. The technique also standardizes the way one may talk about CBS strength as the scale factor is agnostic to any otherwise arbitrary choice in reference line, its central wavelength, and absorption depth.

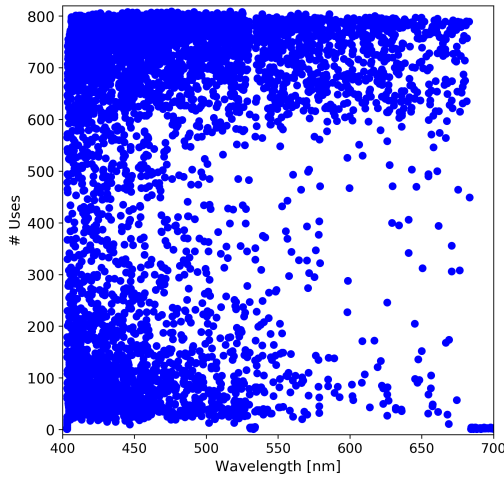


Figure 2.10.: Initial line utilization; number of stars per line over wavelength.

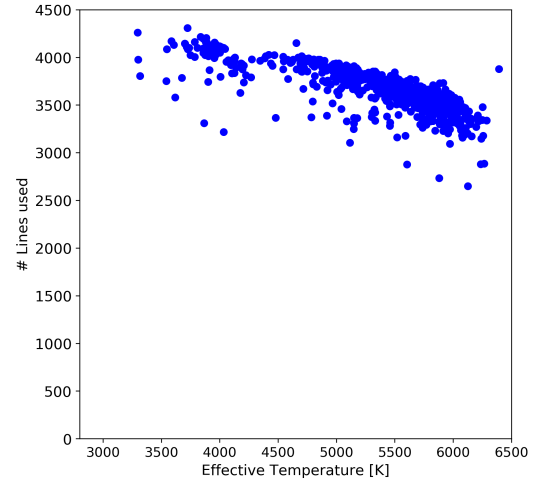


Figure 2.11.: Initial line numbers; number of lines per star over T_{eff} .

2.10. Appendix

Line list refinement

In Sect. 2.5.2 we explain how we created the list of lines used in this chapter. An important part was that the base line list obtained from VALD still contains a large number of lines that are present in a star matching the parameters used for the extraction, but not necessarily in all stars in the intended spectral range from late-F dwarfs to M dwarfs. It also does not guarantee that a specific line, while present, is reliably measurable. For this reason the prefiltered line list was post-processed after the first round of measurements to remove such occurrences. The measuring algorithm developed in this chapter already flags lines that could not be measured accurately. Investigating the line utilization (Fig. 2.10) it is readily apparent that a good part of them is used only rarely, but also that numerous lines are used in nearly all stars. It can also be seen that the blue end, up to about 500 nm contains the majority of usable lines, limiting the use of data from instruments such as CARMENES, which are geared more toward red wavelengths. Figure 2.11 shows the number of lines used per star. One can see that with 3000-4000 lines per star, there is room for vetting the line list. Figure 2.12 illustrates how the vetting step worked by plotting for each line the standard deviation of the residual between the fitted third signature and the measured line position over all stars against the mean residual. It can be seen that many lines are intrinsically less suited for the third-signature determination, showing large deviations over the entire sample. They were identified and excluded by retaining only lines that had a standard deviation that is not zero, meaning that they are used more than once, whose mean residual fell below the 25th percentile, and which had a standard

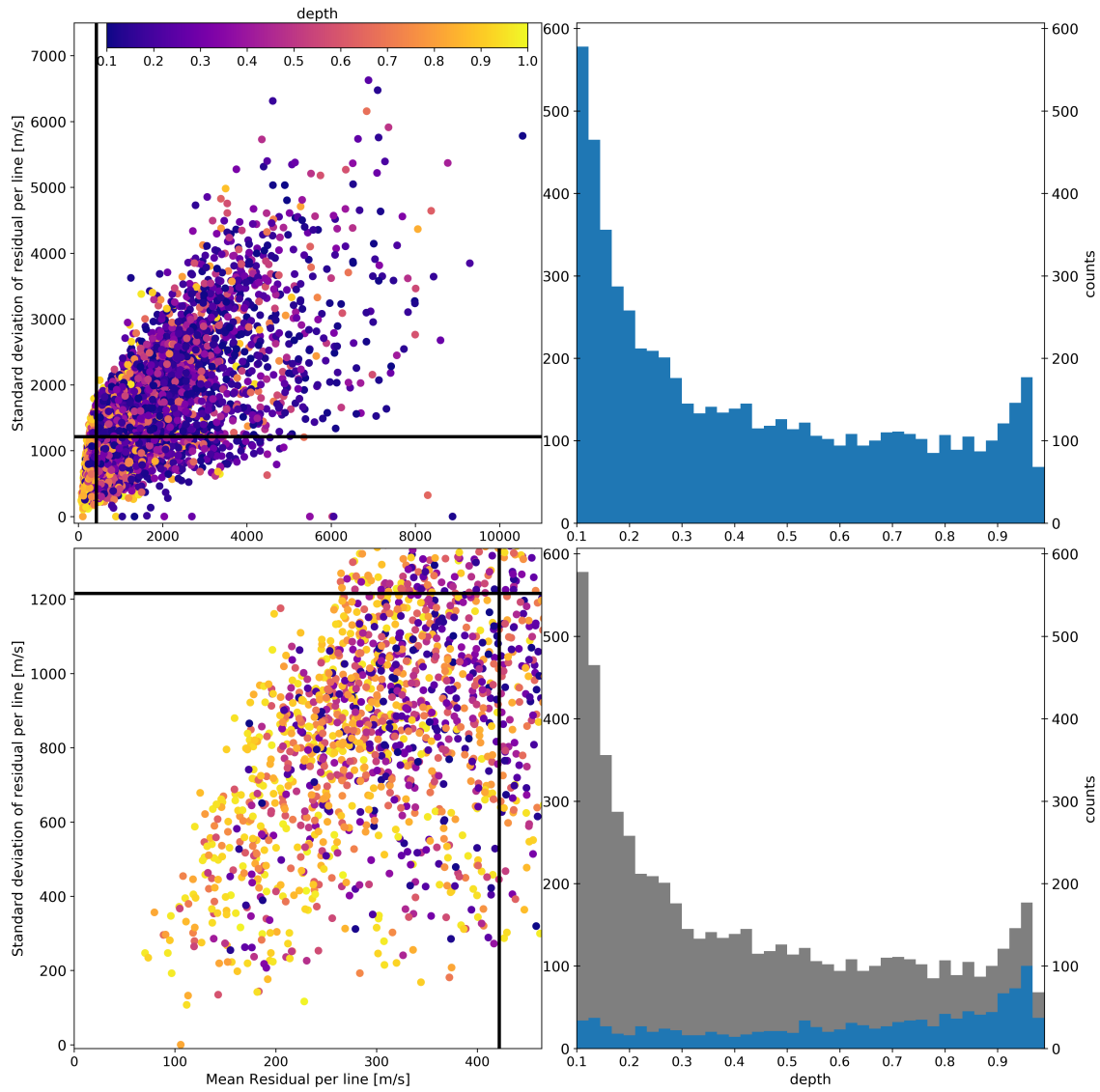


Figure 2.12.: Percentile-based line list vetting. Left panels: Mean and STD of residuals per line over all stars. Marked are 25th percentile for mean and 50th for std. Colors indicate line absorption depth from the VALD 3700 K list. Right panels: Corresponding histograms of line depth counts for the full set of lines (top) and the percentile filtered subset (bottom).

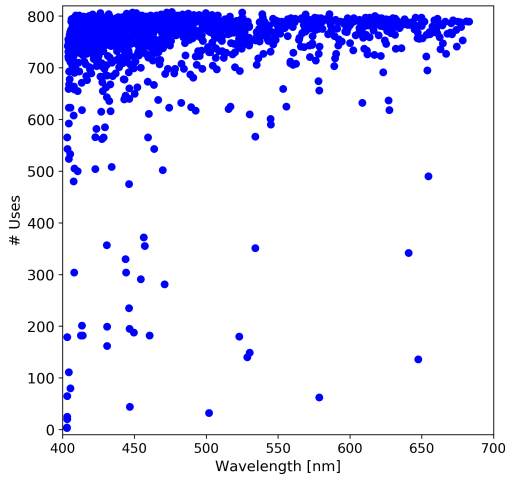


Figure 2.13.: Remaining line utilization; number of stars per line over wavelength.

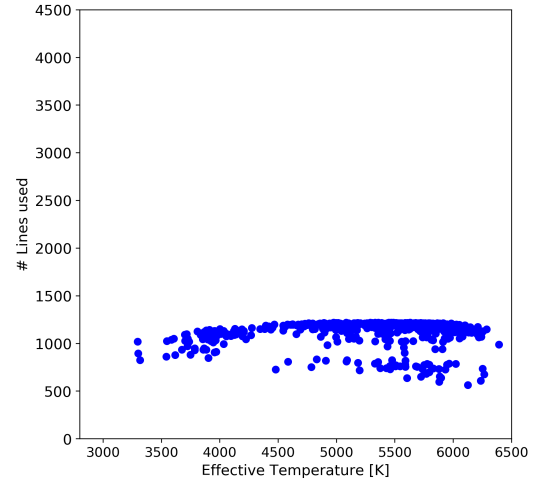


Figure 2.14.: Remaining line numbers; number of lines per star over T_{eff} .

deviation below the 50th percentile. These values were found as a compromise between number of lines retained and quality of the resulting third signatures. Redoing the first two figures (now Fig. 2.13 and 2.14) all the seldomly used lines are gone without impacting the wavelength coverage. For each star the vetting means a reduction in line use by about a factor of two, leaving FGK stars with about 1300 lines each. M-stars are reduced to about 1000 lines.

The removed lines are generally listed as shallow in the VALD 3700 K list, as can be seen by the color coding in Fig. 2.12, which is not surprising since they are harder to measure accurately due to their comparatively higher width relative to their depth. This makes them more susceptible to noise. The mean and standard deviation are correlated with depth at Pearson $r=-0.35$ and -0.30 . Wavelength shows a much weaker, effectively irrelevant, correlation at $r=-0.03$ and 0.001 , respectively. By filtering, the majority of lines involved are no longer located at shallow depths but changed to deep lines. Magnetic sensitivity, that was approximated by the Landé factor, seems to play no role in the filtering at $R=0.04$ and 0.02 for mean and standard deviation, respectively.

Wavelength dependence of CBS

The scatter remaining in Fig. 2.4 can be seen in many works. A commonly explored possibility is the central wavelength of the line as the source. For instance, [Allende Prieto & Garcia Lopez \(1998\)](#) have found no such dependence by plotting line shift against central wavelength, as shown in the left panel of Fig. 2.16 for the data of this work. The problem with this approach is that such a simple plot will generally show no dependence at all. The reason for this is that the line depths are not evenly distributed in wavelength

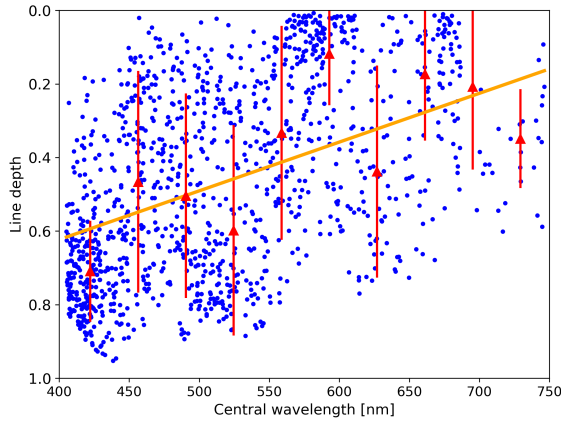


Figure 2.15.: Distribution of line absorption depth with central wavelength (blue dots). The binned data are plotted in red with error bars. A linear fit is shown as an orange curve. The trend toward deep lines in the blue region is readily apparent as is the higher density of lines.

Parameter	Value	Parameter	Value
$a_{m,1}$	2.04	$a_{b,1}$	-123.56
$a_{m,2}$	0.21	$a_{b,2}$	-108.85
$a_{m,3}$	0.34	$a_{b,3}$	-249.90
$a_{m,4}$	0.17	$a_{b,4}$	-610.50

Table 2.3.: Coefficients for the wavelength dependent, solar third-signature model from Eq. 2.4 - 2.6

as shown in Fig. 2.15, but have a tendency for deeper lines to be more numerous toward shorter wavelengths. With deeper lines showing less blueshift, one would therefore expect less blueshift at shorter wavelengths as is also shown in the left panel of Fig. 2.16 for the given distribution of lines and solar template signature. To extract this apparently missing correlation from our solar FTS data, the depth dependence was removed by first binning by depth and then by wavelength. The result is plotted in Fig. 2.16 and shows the required trend to explain the discrepancy. In the following we proceed to quantify how much of the scatter in blueshift for the solar third signature can be attributed to the wavelength effect.

We created a two-dimensional model, linear in wavelength λ and of third order in absorption depth d , with the third order polynomials in depth defining the coefficients of the linear wavelength dependence.

$$v_{\text{conv},\odot}(\lambda, d) = m(d) \cdot \lambda + b(d), \quad (2.4)$$

$$m(d) = a_{m,1} \cdot d^3 + a_{m,2} \cdot d^2 + a_{m,3} \cdot d + a_{m,4}, \quad (2.5)$$

$$b(d) = a_{b,1} \cdot d^3 + a_{b,2} \cdot d^2 + a_{b,3} \cdot d + a_{b,4}. \quad (2.6)$$

Before fitting, the data were binned first in depth with 0.1 units width and then in wavelength with ten bins of 35 nm width spanning 400-750 nm, similar to Fig. 2.16. The model followed Eq. 2.4 - 2.6 with the resulting fit parameters given in Table 2.3. The boundaries on the spread expected from the covered wavelength range are shown in Fig. 2.17, and seem to encapsulate most of the scatter for the deeper lines. The shallow lines still show a much larger scatter, which is not unexpected for previously explained reasons. The wavelength dependent model also agrees with the independent one, if one inputs the

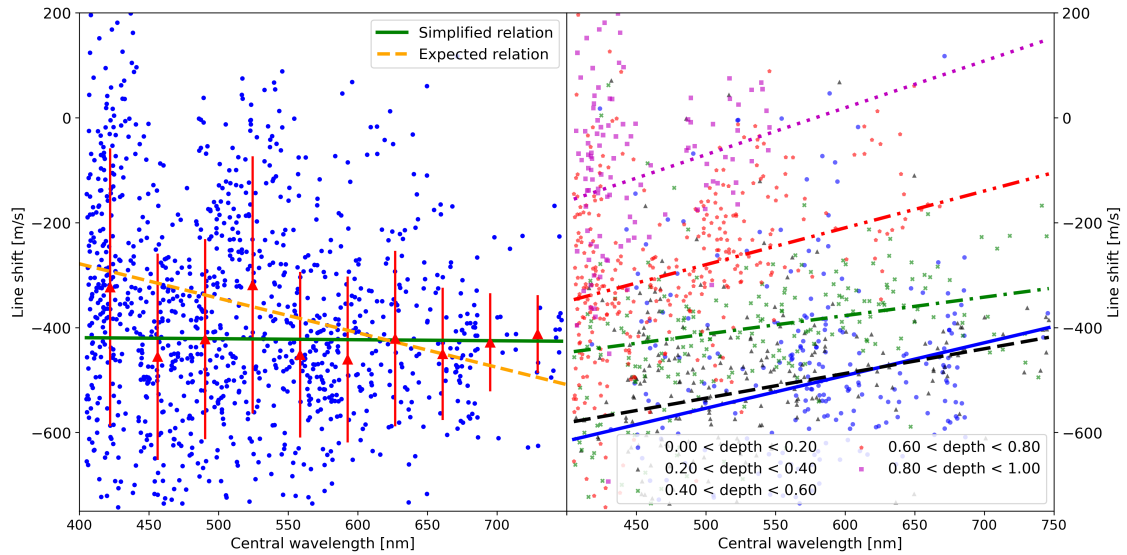


Figure 2.16.: Two approaches to the wavelength dependence of CBS. Left: Simplified attempt at finding the dependence by directly plotting the line shift against the central wavelength (blue dots). Binning the data (red triangles with error bars) and applying a linear fit (green, continuous line) does not reveal any dependence. The orange, dashed line represents the expectation based on Figs. 2.4 and 2.15 assuming lines at 400 nm to have an average depth about 0.7 and at 750 nm of about 0.2. Right: Depth-binned dependence of line shift on central wavelength. By largely removing the influence of line depth through binning, the actual wavelength effect becomes visible. The slopes of the binned wavelength effect compared to the depth distribution effect (left panel, dashed line) reveal an equal but opposite magnitude, accounting for the missing wavelength dependence in the simplified approach (left panel, solid line).

median wavelength of the lines used. In the main part of this chapter, it is the wavelength independent model from Eq. 2.2 that was used, as explained in Sect. 2.6.

Algorithm performance

Accuracy of line center

Determining the third-signature strength depends on line depth and shift, with the latter, as a first moment, being more difficult to determine exactly. For that reason we tested a set of artificial, Gaussian lines, generated for a resolving power of $R = 1,400,000$, a S/N of 340, a central wavelength of 600 nm, and to match a given full-width-at-half-maximum (FWHM) and central depth. The Gaussian noise was applied to 1000 instances of the profile with different random seeds and measurements started at 200 starting points, again randomly distributed with a Gaussian standard deviation of 500 m s^{-1} . The starting points were the same on each of the 1000 instances. Figure 2.18 shows the resulting absolute deviations between the measured center of the line and the actual center, median averaged

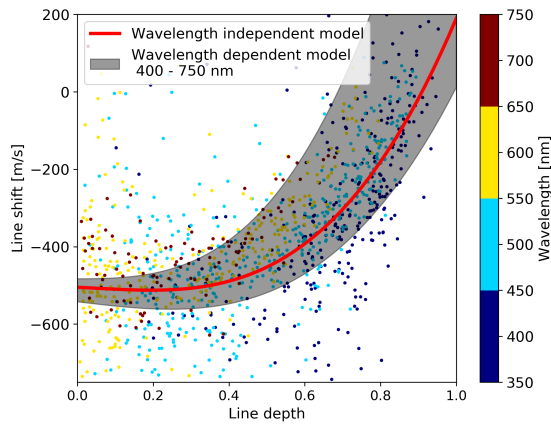


Figure 2.17.: Fitted solar third signature as seen in Fig. 2.4 (red) that does not take the wavelength dependence into account and the revised model (black shaded) that does. Individual lines are color coded according to their wavelength. The lower boundary corresponds to a wavelength of 400 nm and the upper to 750 nm, covering the spectral range of the data. The individual lines' measurements (blue) are shown without their error bars for visibility reasons. The revised model much better captures the spread toward deeper lines.

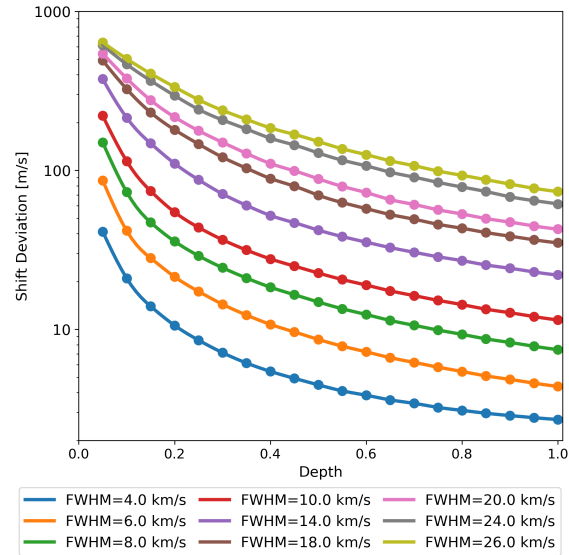


Figure 2.18.: Deviation between the measured center of an artificial, Gaussian absorption line and the true center with Gaussian noise applied and randomized initial measuring points.

over all instances and starting points. The figure shows that for FWHM values that can be expected for the reduced line list, the expected uncertainty in the center of individual lines in the depth range in question is less than 40 m s^{-1} , underlining the need for many lines to be available for measurement. It also means that for fast rotating stars with strongly broadened lines, measuring the line centers becomes harder. This can be taken from Fig. 2.18 by selecting a fixed depth of a line and moving toward higher equivalent widths, that is, upward to higher deviations.

Accuracy of line depth

Reusing the simulated Gaussians from Sect. 2.10 also allows for an assessment of the accuracy of the determined line depths. From Fig. 2.19 it can be seen that the deviations are at worst on the order of 4 per mill. Unlike the central shift, the depth not only becomes less accurate for shallow, wide lines but also for very deep ones. This is due to the fixed width of the fitted region that starts to encompass parts of the line where the parabolic approximation breaks down. This could be mitigated by employing a check for an increase in residual toward the wings, indicating a too wide fitting window, or replacing the parabola with a Gaussian function. Both of those would increase the computational over-

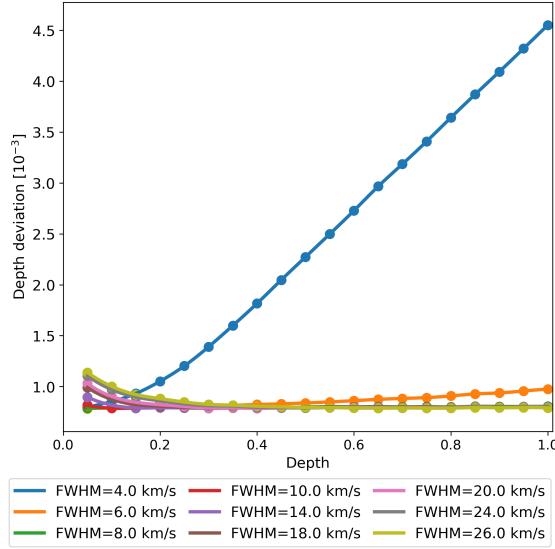


Figure 2.19.: Deviation between the measured depth of an artificial, Gaussian absorption line and the true depth with Gaussian noise applied and randomized initial measuring points.

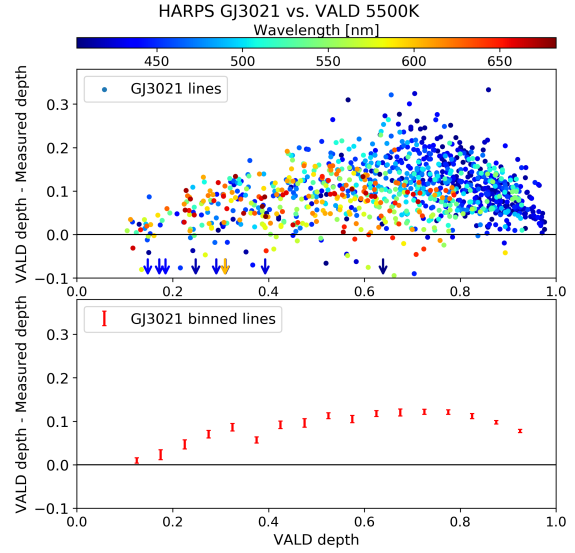


Figure 2.20.: Deviation between VALD line depths and Measured depths from the GJ3021 HARPS spectrum. Top: Deviations of individual lines, color coded for wavelength. Bottom: Binned deviations with uncertainties.

head while the deviations are small and rare enough to be of no consequence compared to all other sources of error.

A similar check was performed using the original VALD extractions listed depths and comparing those to measurements of the closest matching star of our HARPS sample. For the 5500 K case and GJ3021 as the candidate, this is shown in Fig. 2.20. A systematic deviation is clearly visible due to the influence of instrumental and rotational line broadening interacting with the distribution of line equivalent width against absorption depth. Both very shallow and very deep lines show a higher width, relative to their depth, and are less affected by broadening effects, remaining closer to the VALD listed values, while wavelength has no effect. The effect of this systematic is explored in Sect. 2.10, here we focus on the implications of the precision in line depth determination rather than accuracy. Binning the lines in depth following Sects. 2.6 and 2.7 reveals binned uncertainties between $3.7 \cdot 10^{-3}$ and $11.3 \cdot 10^{-3}$ with an average of $7.3 \cdot 10^{-3}$. While significantly less precise than the synthetic expectation, this is still well within the acceptable range when compared to the differential RV uncertainties. After conversion to an RV shift (Eq. 2.2) the depth uncertainty translates to $\lesssim 10 \text{ m s}^{-1}$, on par with the expected uncertainty for the RV determination itself. Similar precision can be found when comparing the three remaining line lists from Table 2.1.

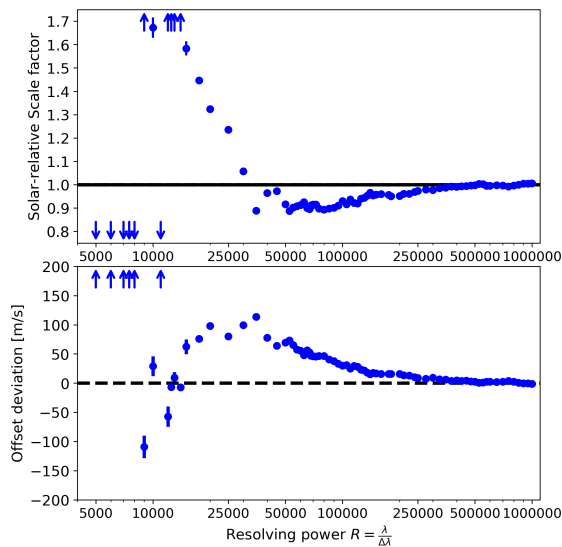


Figure 2.21.: Effect of resolving power, R , on the determined solar scale factor. Top: Scale factor against resolving power, where individual results with different velocity offsets but identical resolving power are median-binned. The horizontal line indicates a scale factor of one, identical to the result from the unconvolved, unshifted FTS. Bottom: Measured velocity offset from the third signature fit, corrected for the synthetic one and binned by R . The dashed line marks zero velocity offset.

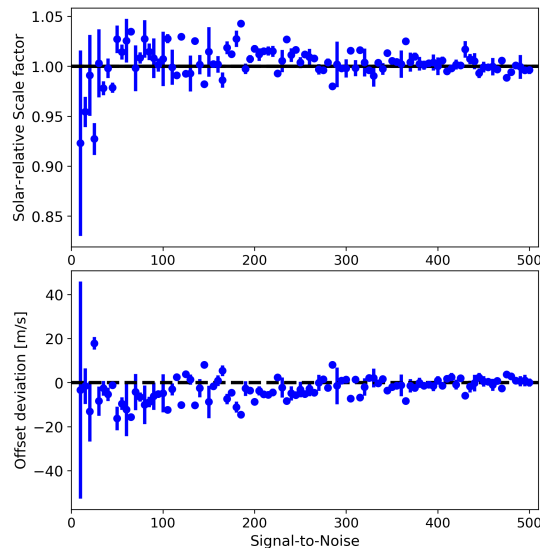


Figure 2.22.: Effect of signal-to-noise ratio on the determined solar scale factor. Top: Scale factor against S/N , individual results with different velocity offsets but identical S/N are median-binned. The horizontal line indicates a scale of one, identical to the result from the undegraded, unshifted FTS. Bottom: Measured velocity offset from the third-signature fit, corrected for the artificial velocity. The dashed line marks zero velocity offset.

Effects of resolving power

While HARPS is already an instrument of tremendous resolving power ($R \gtrsim 100,000$), an FTS has $R > 1,000,000$. Effects due to lower resolving power need to be taken into account (see Sect. 2.6), especially since Sect. 2.10 has shown that narrow lines, relative to their depth, are the best targets but also the first to get smeared out in broadened, low- R spectra. To check the effect this has on the determination of blueshift strength, the FTS solar atlas was convolved with a Gaussian broadening kernel to simulate a lower resolving power and Doppler shifted by values spanning $\pm 100 \text{ m s}^{-1}$ in 25 m s^{-1} steps. The reduced line list that was used for the HARPS data was applied to the convolved and shifted solar spectrum and the third-signature scale factor determined. This was repeated for a range of resolving powers. The results, median averaged over the offsets, can be seen in Fig. 2.21. Resolving powers down to about 50,000 can be corrected for, using correction factors as given in Sect. 2.6, as they have close to no effect on the precision of the results, as opposed to the accuracy. The decrease in observed blueshift is due to originally deeper lines, with correspondingly lower blueshift, appearing shallower, thereby lowering the average blueshift in the measured bins. It can be concluded that HARPS' resolving power does

not pose a problem in this regard; however, attempting the same with lower-resolution instruments (e.g., $R \lesssim 50000$) leads to a different conclusion. Below a resolving power of $R \approx 10000$ the technique breaks down completely.

Effects of stellar rotation

An analogous analysis to Sect. 2.10 was performed for stellar rotation, parameterized by the projected rotational velocity $v \sin i$. We again selected the FTS spectrum degraded to $R \approx 110.000$ and applied rotational broadening from the PyAstronomy package `PyAstronomy.pyasl.asl.rotBroad` for a range of velocities. This reveals a behavior very similar to Fig. 2.21. At $R \approx 110.000$, $v \sin i$ leaves the scale factor largely unaffected up to 6 km s^{-1} . Similar deviations to $R \approx 25.000$ become visible at velocities of 8 km s^{-1} , with intermediate behavior matching as well. In terms of FWHM broadening this is unsurprising, as pure Gaussian broadening at $R \approx 25.000$ and mixed broadening at $R \approx 110.000$ and $v \sin i = 8 \text{ km s}^{-1}$ both result in $\text{FWHM} \approx 14 \text{ km s}^{-1}$, the apparent upper limit of our method.

Effects of signal-to-noise

Analogous to the resolving power investigated in Sect. 2.10, the influence of the signal-to-noise ratio can be quantified. Again, the solar FTS was used as the template but instead of being convolved with a broadening kernel, Poissonian noise was added to a specific S/N and the entire spectrum shifted to given offsets, identical to the test for resolving power. The result is shown in Fig. 2.22. The results in scale and offset are mostly consistent down to $\text{S/N} \sim 50$. Below that threshold the scale factor drops significantly, which could be corrected for, but also loses precision and the results must be considered unreliable. An S/N above 200 on the other hand seems to be fully unproblematic and gives fully consistent results, with $100 < \text{S/N} < 200$ remaining acceptable. This reinforces the reliability of the scale factors for all stars in our sample as only a single star shows questionable $\text{S/N} < 50$ and nine stars are $50 < \text{S/N} < 100$.

Additional figures

In this section of the appendix we provide two figures that expand on points raised in the main text. Figure 2.23 shows an example spectral order to illustrate the workings of our sinc^2 boundary fit. Figure 2.24 expands on Fig. 2.6 by additionally scaling the marker sizes with their corresponding χ^2 values from the third-signature fit and color coding the S/N of the spectra.

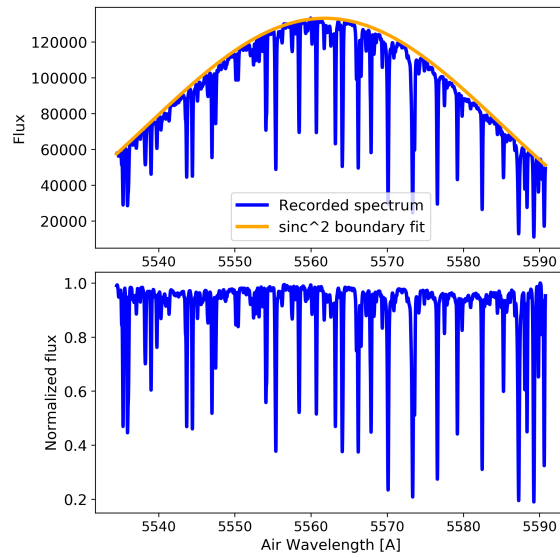


Figure 2.23.: Example for the continuum normalization. Top: Example for a sinc^2 boundary fit (orange curve) to the 50th recorded echelle order (blue curve) from GJ4340. Bottom: Normalized flux.

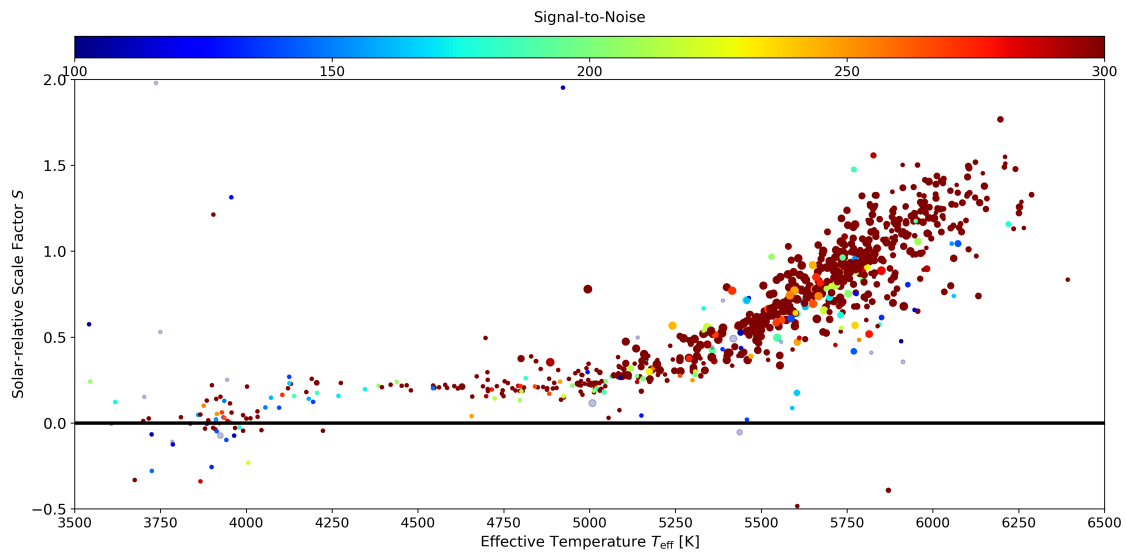


Figure 2.24.: Third-signature scale for reduced line list with points scaled following the fits χ^2 . Smaller points correspond to larger χ^2 values.

Tables

For ease of access and a quicker overview, we list in Table 2.4 the expected CBS strengths and velocities for the range of spectral subtypes from F0 to K8 based on our model from Eq. 2.3. Table 2.5 lists all stars of our sample with basic parameters important to this chapter and the determined CBS strengths and uncertainties. The full Table is available via CDS.

Table 2.4.: Scale factor cheat sheet following Eq. 2.3. Available online at CDS.

Spectral Type	Effective temperature [K]	Scale factor	Velocity [m s^{-1}]
F0	7220	6.019	-2163.1
F1	7030	4.926	-1770.5
F2	6810	3.844	-1381.6
F3	6720	3.455	-1241.6
F4	6640	3.133	-1125.9
F5	6510	2.657	-954.8
F6	6340	2.117	-760.7
F7	6240	1.840	-661.3
F8	6170	1.664	-597.9
F9	6060	1.413	-507.9
G0	5920	1.139	-409.4
G1	5880	1.069	-384.3
G2	5770	0.896	-322.2
G3	5720	0.826	-297.0
G4	5680	0.774	-278.2
G5	5660	0.749	-269.2
G6	5590	0.668	-240.0
G7	5530	0.605	-217.5
G8	5490	0.567	-203.8
G9	5340	0.447	-160.7
K0	5280	0.409	-146.9
K1	5170	0.351	-126.1
K2	5040	0.301	-108.0
K3	4830	0.254	-91.1
K4	4600	0.235	-84.5
K5	4410	0.233	-83.7
K6	4230	0.232	-83.3
K7	4070	0.224	-80.4
K8	4000	0.216	-77.8

Notes. The velocities given assume a line depth of 0.7 (Eq. 2.2), corresponding to a median solar line, in order to match an expected -350 m s^{-1} at 5800 K.

3. [Paper] Convective Blueshift among evolved stars

The following chapter was prepared to be published in the journal *Astronomy & Astrophysics* under the same title but could not be completed in time. Some minor adjustments to the wording of structural references compared to the version intended to be submitted were made to conform with the Thesis format, replacing "paper" and "this work" with "this chapter", references to "paper I" as chapter 2 and sections, figures or equations therein with the correct references. The layout was changed from two to single column format.

The coadded spectra analyzed for this work were provided by Trifon Trifonov (Trifonov et al. 2020). The analysis was carried out and the paper written by F. Liebing. The co-authors S.V. Jeffers, M. Zechmeister and A. Reiners provided their insight to help with the interpretation of the results and gave comments during the editing stage to further improve the clarity of the paper.

FL acknowledges the support of the DFG priority program SPP 1992 "Exploring the Diversity of Extrasolar Planets (RE 1664/18). SVJ acknowledges the support of the German Science Foundation (DFG) priority program SPP 1992 'Exploring the Diversity of Extrasolar Planets' (JE 701/5-1). The SIMBAD database¹, hosted at the CDS, Strasbourg, France, was used in this research. This research has made use of NASA's Astrophysics Data System Bibliographic Services². This work has made use of the VALD database³, operated at Uppsala University, the Institute of Astronomy RAS in Moscow, and the University of Vienna. This work has made use of data from the European Space Agency (ESA) mission *Gaia* (<https://www.cosmos.esa.int/gaia>), processed by the *Gaia* Data Processing and Analysis Consortium (DPAC, <https://www.cosmos.esa.int/web/gaia/dpac/consortium>). Funding for the DPAC has been provided by national institutions, in particular the institutions participating in the *Gaia* Multilateral Agreement. The original observations, provided after pre-processing by TT, were collected at the European Organization for Astronomical Research in the Southern Hemisphere under ESO programmes: 0100.C-0097, 0100.C-0111, 0100.C-0414, 0100.C-0474, 0100.C-0487, 0100.C-0750, 0100.C-0808, 0100.C-0836, 0100.C-0847, 0100.C-0884, 0100.C-0888, 0100.D-0444, 0100.D-0717, 0101.C-0232, 0101.C-0274, 0101.C-0275, 0101.C-0379, 0101.C-0407,

¹<http://simbad.u-strasbg.fr/simbad/>

²<http://adsabs.harvard.edu/>

³<http://vald.astro.uu.se/>

0101.C-0516, 0101.C-0829, 0101.D-0717, 0102.C-0338, 0102.D-0717, 0103.C-0548, 0103.D-0717, 060.A-9036, 060.A-9700, 072.C-0096, 072.C-0388, 072.C-0488, 072.C-0513, 072.C-0636, 072.D-0286, 072.D-0419, 072.D-0707, 073.A-0041, 073.C-0733, 073.C-0784, 073.D-0038, 073.D-0136, 073.D-0527, 073.D-0578, 073.D-0590, 074.C-0012, 074.C-0037, 074.C-0102, 074.C-0364, 074.D-0131, 074.D-0380, 075.C-0140, 075.C-0202, 075.C-0234, 075.C-0332, 075.C-0689, 075.C-0710, 075.D-0194, 075.D-0600, 075.D-0614, 075.D-0760, 075.D-0800, 076.C-0010, 076.C-0073, 076.C-0155, 076.C-0279, 076.C-0429, 076.C-0878, 076.D-0103, 076.D-0130, 076.D-0158, 076.D-0207, 077.C-0012, 077.C-0080, 077.C-0101, 077.C-0295, 077.C-0364, 077.C-0530, 077.D-0085, 077.D-0498, 077.D-0633, 077.D-0720, 078.C-0037, 078.C-0044, 078.C-0133, 078.C-0209, 078.C-0233, 078.C-0403, 078.C-0751, 078.C-0833, 078.D-0067, 078.D-0071, 078.D-0245, 078.D-0299, 078.D-0492, 079.C-0046, 079.C-0127, 079.C-0170, 079.C-0329, 079.C-0463, 079.C-0488, 079.C-0657, 079.C-0681, 079.C-0828, 079.C-0927, 079.D-0009, 079.D-0075, 079.D-0118, 079.D-0160, 079.D-0462, 079.D-0466, 080.C-0032, 080.C-0071, 080.C-0664, 080.C-0712, 080.D-0047, 080.D-0086, 080.D-0151, 080.D-0318, 080.D-0347, 080.D-0408, 081.C-0034, 081.C-0119, 081.C-0148, 081.C-0211, 081.C-0388, 081.C-0774, 081.C-0779, 081.C-0802, 081.C-0842, 081.D-0008, 081.D-0065, 081.D-0109, 081.D-0531, 081.D-0610, 081.D-0870, 082.B-0610, 082.C-0040, 082.C-0212, 082.C-0308, 082.C-0312, 082.C-0315, 082.C-0333, 082.C-0357, 082.C-0390, 082.C-0412, 082.C-0427, 082.C-0608, 082.C-0718, 083.C-0186, 083.C-0413, 083.C-0794, 083.C-1001, 083.D-0668, 084.C-0185, 084.C-0228, 084.C-0229, 084.C-1039, 085.C-0019, 085.C-0063, 085.C-0318, 085.C-0393, 086.C-0145, 086.C-0230, 086.C-0284, 086.D-0240, 087.C-0012, 087.C-0368, 087.C-0649, 087.C-0831, 087.C-0990, 087.D-0511, 088.C-0011, 088.C-0323, 088.C-0353, 088.C-0513, 088.C-0662, 089.C-0006, 089.C-0050, 089.C-0151, 089.C-0415, 089.C-0497, 089.C-0732, 089.C-0739, 090.C-0395, 090.C-0421, 090.C-0540, 090.C-0849, 091.C-0034, 091.C-0184, 091.C-0271, 091.C-0438, 091.C-0456, 091.C-0471, 091.C-0844, 091.C-0853, 091.C-0866, 091.C-0936, 091.D-0469, 092.C-0282, 092.C-0454, 092.C-0579, 092.C-0721, 092.C-0832, 092.D-0261, 093.C-0062, 093.C-0409, 093.C-0417, 093.C-0474, 093.C-0919, 094.C-0090, 094.C-0297, 094.C-0428, 094.C-0797, 094.C-0894, 094.C-0901, 094.C-0946, 094.D-0056, 094.D-0596, 095.C-0040, 095.C-0105, 095.C-0367, 095.C-0551, 095.C-0718, 095.C-0799, 095.C-0947, 095.D-0026, 095.D-0717, 096.C-0053, 096.C-0082, 096.C-0183, 096.C-0210, 096.C-0331, 096.C-0417, 096.C-0460, 096.C-0499, 096.C-0657, 096.C-0708, 096.C-0762, 096.C-0876, 096.D-0402, 096.D-0717, 097.C-0021, 097.C-0090, 097.C-0390, 097.C-0434, 097.C-0561, 097.C-0571, 097.C-0864, 097.C-0948, 097.C-1025, 097.D-0156, 097.D-0717, 098.C-0269, 098.C-0292, 098.C-0304, 098.C-0366, 098.C-0518, 098.C-0518, 098.C-0739, 098.C-0820, 098.C-0860, 098.D-0717, 099.C-0093, 099.C-0138, 099.C-0205, 099.C-0303, 099.C-0304, 099.C-0374, 099.C-0458, 099.C-0491, 099.C-0798, 099.C-0880, 099.C-0898, 099.D-0717, 1101.C-0721, 180.C-0886, 183.C-0437, 183.C-0972, 183.D-0729, 184.C-0639, 184.C-0815, 185.D-0056, 188.C-0265, 188.C-0779, 190.C-0027, 191.C-0505, 191.C-0873, 192.C-0224, 192.C-0852, 196.C-0042, 196.C-1006, 198.C-0169, 198.C-0836, 198.C-0838, 281.D-5052, 281.D-5053, 282.C-5034, 282.C-5036, 282.D-5006, 283.C-5017, 283.C-5022, 288.C-5010, 292.C-5004, 295.C-5031, 495.L-0963, 60.A-9036, 60.A-9700, and 63.A-9036.

The analysis was carried out using the programming language Python3⁴ Version 3.7.6 (Van Rossum & Drake 2009), and the accompanying software packages: Numpy⁵ Version 1.18.1 (Harris et al. 2020), Scipy⁶ Version 1.4.1 (Virtanen et al. 2020), Astropy⁷ Version 4.0 (Astropy Collaboration et al. 2013, 2018), Astroquery⁸ Version 0.4.3 (Ginsburg et al. 2019) and Matplotlib⁹ Version 3.1.3 (Hunter 2007).

Table 3.1 and the full Table 3.2 will be available in electronic form at the CDS and in the mean time upon request to the author.

⁴<https://www.python.org/>

⁵<https://numpy.org/>

⁶<https://www.scipy.org/scipylib/>

⁷<https://www.astropy.org/>

⁸<https://astroquery.readthedocs.io>

⁹<https://matplotlib.org/>

Contents

3.1. Abstract	81
3.2. Introduction	81
3.3. Data and processing	83
3.3.1. Observations	84
3.3.2. Data filtering	86
3.3.3. Stellar evolution phase	86
3.4. Technique	87
3.5. Results	89
3.5.1. Temperature dependence of post-MS CBS strengths	89
3.5.2. Surface gravity dependence of post-MS CBS strengths	91
3.5.3. Comparison with literature results	92
3.5.4. Comparison with analytical models	93
3.5.5. Relation to macroturbulence velocities	94
3.5.6. Convection velocities from 3D MHD	96
3.6. Summary and Conclusion	97
3.7. Appendix	98

3.1. Abstract

Context. With the advent of extreme precision radial velocity surveys, seeking to detect planets at RV semi-amplitudes of 10 cm s^{-1} , intrinsic stellar variability is the biggest challenge towards detecting small exoplanets. To overcome the challenge we must first thoroughly understand all facets of stellar variability. Among those, convective blueshift caused by stellar granulation and its suppression through magnetic activity plays a significant role in covering planetary signals in stellar jitter.

Aims. We determine empirical convective blueshift strengths, an observational proxy for the strength of convection near the stellar surface, for 241 post main sequence stars, covering the subgiant, red giant and asymptotic giant phases. The stellar sample ranges in temperature from 3750 K to 6150 K.

Methods. We use the third signature of granulation scaling technique to fit a solar model for convective blueshift strengths to absorption-line shift measurements from a sample of coadded HARPS spectra. We compare the results to main sequence stars of comparable temperature but with a higher surface gravity.

Results. Our results show that convective blueshift becomes significantly stronger for evolved stars compared to main sequence stars of similar temperature. The difference increases as the star becomes more evolved, reaching a 5x increase below 4300 K for the most evolved stars. Absolute convective blueshift strength remains near constant among the evolved star sample at roughly solar convection strength with a slight increase from the red giant phase onward. The convective blueshift strength further shows a local minimum for subgiant stars, presenting a sweet spot for exoplanet searches around higher mass stars.

3.2. Introduction

Convection in stars that have evolved off the main sequence (MS), namely subgiants (SG), red giants (RG), and stars on the asymptotic giant branch (AGB), is a very important factor in their further evolution as well as for their observed properties and overall observability. That is because, as a star leaves the MS, it strongly increases in radius and so does the proportion of the star that is part of the convection zone ([Hekker & Christensen-Dalsgaard 2017](#)). Consequently, understanding the structure, strength and evolution of convective motion in evolved stars is of very high importance to understand post-MS stellar evolution as a whole. Stellar structure simulations predict strong changes in relative convection zone depth for later evolutionary stages, leading to overall deeper elemental mixing and eventually the so-called dredge-ups where freshly fused elements get transported all the way to the surface. Furthermore, the convective surface structure changes fundamentally ([Mathur et al. 2011](#), [Magic & Asplund 2014](#)). This can be observed as a deviation from the well known solar granulation pattern of thousands or millions of small Granules for

MS stars to only a few, massive Granules ([Schwarzschild 1975](#), [Trampedach et al. 2013](#)), potentially spanning over a quarter of the visible surface on red giants ([Paladini et al. 2018](#)). Observationally, this is of high importance because convective granulation leads to the phenomenon of convective blueshift ([Dravins 1987](#), CBS,). This is a result of the flux imbalance between large, hot Granules and smaller, cooler intergranular lanes. The larger influence of the upwards moving material inside Granules due to their higher spatial and flux weighing overcompensates the contribution of the intergranular lanes. Projected onto the line of sight towards the observer and integrated over the visible stellar disk, this results in an overall blueshift of the observed spectral lines. The strength of CBS varies with time, as the granulation pattern evolves and can differ significantly between stars which have different convection strength and structures.

Besides the obvious interest for stellar evolution and structure research, post-MS stars are of interest to exoplanet researchers as well ([Saunders et al. 2022](#)). For one, the distribution of planets and their orbits around evolved stars allows an insight into the fate of planets when compared to their younger MS counterparts. From the observed differences, it is possible to infer details of the orbital decay due to tidal forces and improve the models for planetary system evolution ([Villaver & Livio 2009](#), [Grunblatt et al. 2018](#)). It is also expected that the key to the discovery of the mechanism behind inflated gas giants may be found within evolved stellar systems ([Lopez & Fortney 2016](#)), because the most prominent explanations give distinguishably different predictions primarily in these surroundings (re-inflation: [Grunblatt et al. 2017](#) vs. delayed cooling: [Batygin & Stevenson 2010](#); to give just two examples). Lastly, the spin-down experienced during the subgiant phase significantly lowers the projected rotational velocity of the evolved stars. This allows to hunt for planets around stars whose fast rotation during the MS phase inhibits or outright prohibits the detection due to rotational spectral broadening and high activity levels with spectroscopic methods ([Lloyd 2013](#)). The question about the relation between planet occurrence rate and host star mass, which appears to show a correlation ([Bowler et al. 2010](#)), heavily depends on this.

Unfortunately, not many planets have been found to date around evolved stars, accounting for only $\sim 3\%$ of all exoplanet candidates (150 [Takarada et al. \(2018\)](#), 135 [Döllinger & Hartmann \(2021\)](#); out of 4900 confirmed planets¹⁰). Two reasons for this are the strong focus on exoplanet searches around solar-like rather than evolved stars and the difficulties involved with high-precision studies of giant stars. While stellar activity and related jitter decreases from spin-down during the subgiant phase, convection, granulation, and related effects become much stronger due to the fundamental changes in stellar structure ([Luhn et al. 2020](#), [Bastien et al. 2013](#)). Similarly, stellar oscillations become much stronger over the post-MS evolution as predicted by the scaling relations from, among others, [Kjeldsen & Bedding \(1995\)](#). From an amplitude of $\sim 20 \text{ cm s}^{-1}$ and a period of ~ 5 minutes for the Sun this can increase to tens of meters per second and multiple days for highly evolved stars, making it a much bigger obstacle than for MS stars ([Chaplin et al. 2019](#)).

¹⁰From the exoplanet.eu catalog

Besides that complication, [Haywood et al. \(2016\)](#) have already classed granulation on its own as the biggest problem for MS planet searches. Its effects can not be mitigated sufficiently through longer integration time or coaddition, can not be recovered through photometric-spectroscopic synergies, or correlations with spectroscopic activity indicators. The latter is due to the correlations between the classical indicators and convective blueshift variations being too weak (see their Fig. 10 for examples). Instead [Haywood et al. \(2016\)](#) suggest the use of the unsigned magnetic flux, which they derived from SDO HMI magnetogram images, as a more direct proxy of the CBS variability. As this quantity is very hard to determine for other stars with a reasonable degree of confidence, and since one is interested in changes in CBS itself, a better approach might be to measure those changes directly, circumventing the need for well correlated proxies. In chapter 2 ([Liebing et al. 2021](#)) we describe a method to do this in a robust and purely empirical way. Using the described technique, we find that CBS in early G-type dwarfs like our Sun is roughly 4-5 times stronger than for mid-K types, increasing with the third power of the stellar effective temperature after a plateau for late K-dwarfs. This leads to a matching strength increase for CBS related effects that is currently preventing the detection of true Earth-twins ([Meunier et al. 2015](#)) and limits our detection capabilities for Earth-mass planets to late type stars. For evolved stars the problem is even more extreme due to their fewer, larger Granules, increased contrast to the intergranular lanes ([Trampedach et al. 2013](#)), and more massive starspots that inhibit convective motion. All this comes together to form a "flicker floor" that increases with decreasing surface gravity ([Bastien et al. 2013](#)). Therefore, a better understanding of convective granulation on evolved stars on an empirical level is paramount to the resolution of all these questions, even more so than for MS stars.

Solving this problem is especially important in the face of the massive amounts of data that have become available from past and current space missions, for instance Kepler/K2 and TESS, and will become available from future missions such as PLATO. While not dedicated towards evolved stars, the observation fields still contain tens of thousands of them that we can not exploit until our current inability to properly account for their intrinsic variability has improved.

With this motivation, we seek to measure the CBS strength for post-MS stars in the sub-giant, red giant, red clump or horizontal branch and asymptotic giant branch phases and thereby provide empirical convection strengths, as we did in [Liebing et al. \(2021\)](#) for MS stars.

3.3. Data and processing

In this chapter we extend our work on the sample of HARPS spectra from chapter 2 ([Liebing et al. 2021](#)) from the main sequence to the previously excluded post-MS regime. To that end, we apply the technique from chapter 2, summarized in Sect. 3.4, to the previously excluded sample of stars and supplement with a sample of spectra from the

PEPSI spectrograph for comparison. Further, we determine the evolutionary stages of the post MS stars from the sample to better interpret the results.

3.3.1. Observations

The primary data set behind this chapter and chapter 2 was compiled by Trifonov et al. (2020), who collected, sorted and filtered all publicly available spectra from the HARPS¹¹ spectrograph, a fibre-fed, cross-dispersed echelle spectrograph with a resolving power of $R=115\,000$. HARPS spans the range between 380 nm and 690 nm over 72 echelle orders. It is housed in a temperature stabilized, evacuated chamber at the 3.6 m telescope at La Silla, Chile and is capable of reaching a precision of $1\,\text{m s}^{-1}$ (Mayor et al. 2003). Trifonov et al. (2020) coadded all spectra belonging to the same object, using the "SpEctrum Radial Velocity AnaLyser" (*serval*, Zechmeister et al. 2018) which also provides radial velocities (RVs) from matching the coadded spectra as templates to the individual observations. Nightly offsets and long-term trends, for example binary motion, were corrected for the individual spectra as well. We made use of the coadded template spectra, after converting them to air wavelengths, for their increased S/N as well as referenced the RV values listed in the *RVBANK* from Trifonov et al. (2020). The individual, coadded spectra were processed, normalized and analyzed identically to chapter 2 (see Sect. 3.4 for a summary, chapter 2 for details). Figure 3.1 shows the MS sample from chapter 2 for comparison together with the post-MS sample analyzed in this chapter in a Hertzsprung-Russel diagram based on *Gaia* DR2 parameters and MIST synthetic photometric fits (Sect. 3.3.3).

The S/N ratios provided by *serval* for the coadded spectra are shown in Fig. 3.2 in the top panels for each star individually (left) and binned by S/N (right, stacks colored to reflect evolutionary phase). On average, 27 spectra were used per coaddition for an approximate S/N of 555, with some stars significantly higher. The sample, binned by

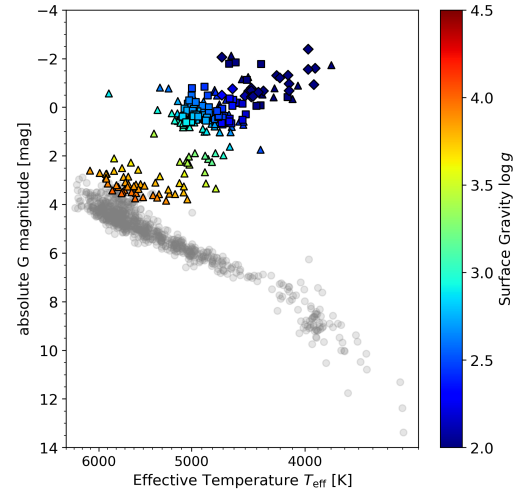


Figure 3.1.: Our sample of HARPS stars (post-MS colored for surface gravity fitted from MIST model, MS stars from chapter 2 in gray) in an Hertzsprung-Russel diagram, based on *Gaia* DR2 data. The marker shapes correspond to the evolutionary phases according to MIST: main sequence (circle), sub- or red giant (triangle), core Helium burning (squares) and asymptotic giant (diamonds).

¹¹High-Accuracy Radial velocity Planetary Searcher

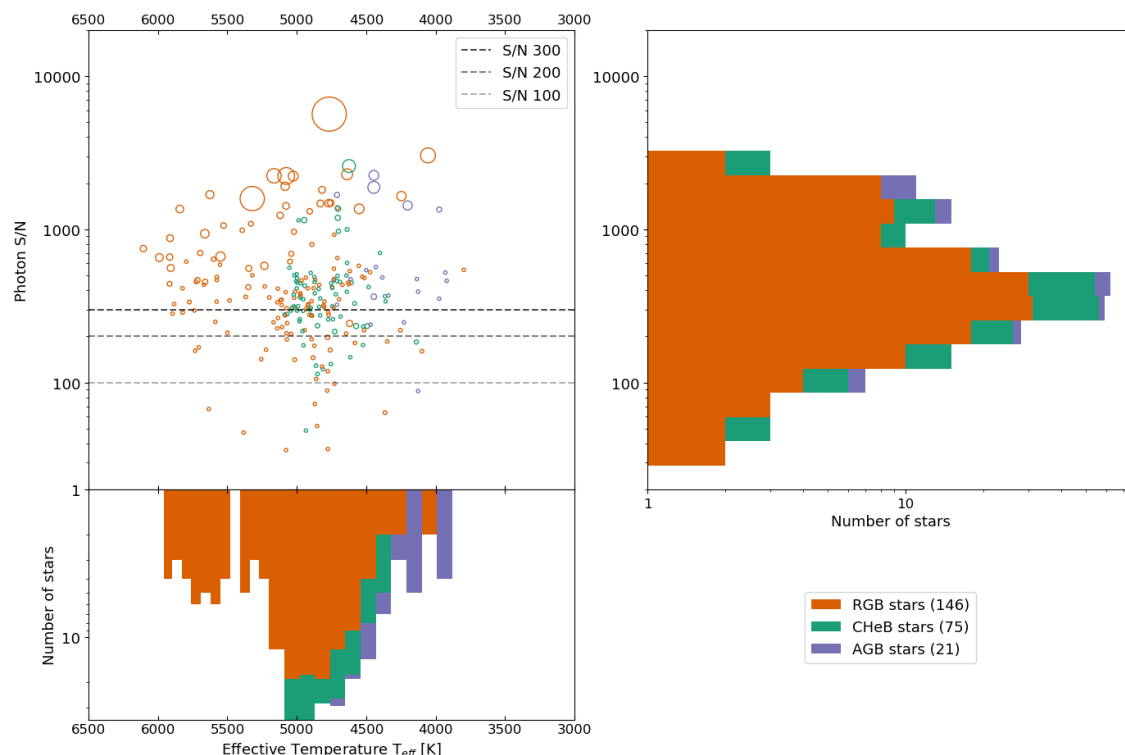


Figure 3.2.: Overview of all final sample stars’ signal-to-noise ratio (S/N) from *serval*, temperature from *Gaia* DR2, and evolutionary phase according to MIST photometry (color coded; the legend shows the number of stars per phase). Top left: Distribution of S/N over temperature within the sample. The circle size corresponds to the number of observations for that star. The dashed, horizontal lines mark S/N values of 100, 200 and 300. Top right: S/N for the coadded spectra in the sample. Bottom left: Distribution of temperatures within the sample.

temperature and color-stacked by evolutionary phase, is shown in the lower panel of Fig. 3.2. Table 2.5 gives a complete list of the stars from the final sample, including their parameters.

In addition, we supplemented our sample with data from the PEPSI¹² spectrograph, published by Strassmeier et al. (2018), for comparison and verification of our results from HARPS (Sect. 3.7). PEPSI is a fibre-fed instrument mounted at the 2 x 8.4 m Large Binocular Telescope (LBT) on Mt. Graham, Arizona, USA that covers the range of 383 - 907 nm at a resolving power of up to 270 000 (Strassmeier et al. 2015). We were able to use the data as provided for our line-by-line measurements, as the spectra are corrected for RV, continuum normalized, stitched and given in air wavelengths, with no further preparation necessary. The data set is visualized in an HR diagram in Fig. 3.10.

¹²Potsdam Echelle Polarimetric and Spectroscopic Instrument

3.3.2. Data filtering

Out of the complete, 3094 star sample, covering all evolutionary stages, 439 were excluded in chapter 2 for lack of a match with *Gaia* DR2 stars (Gaia Collaboration 2018) which were used as a source of consistent stellar parameters, such as effective temperature values. From the remainder, 810 MS stars were identified, based on SIMBAD¹³ surface gravities $\log g$ and *Gaia* G magnitude in conjunction with effective temperature T_{eff} , and analyzed in chapter 2. The database values for $\log g$ were used only for this filtering step, further analyses use the values determined in Sect. 3.3.3. This chapter investigates the 458 stars that were not included in chapter 2 as they were presumed to be post MS. In chapter 2 we found that we needed to exclude stars with a projected rotational velocities of $v \sin i > 8 \text{ km/s}$ due to the effect the combined instrumental and rotational broadening has on our analysis technique, which is summarized in Sect. 3.4. Our $v \sin i$ values were taken primarily from SIMBAD, followed by Glebocki & Gnacinski (2005). As a proxy, we further used HARPS DRS FWHM values from Trifonov et al. (2020). They don't correlate perfectly with $v \sin i$ but provide a first order approximation that allows to exclude a few more fast rotating stars that don't have velocities listed in the other references.

For the PEPSI data, despite the higher resolving power of the instrument compared to HARPS, we have retained the 8 km s^{-1} $v \sin i$ limit because the decrease in instrumental broadening only allows a negligible extension of 200 m s^{-1} to the acceptable projected rotational velocity.

3.3.3. Stellar evolution phase

The preliminary sample for this chapter, after the $v \sin i$ and FWHM filtering of the presumed post-MS sample, comprises 267 stars. The specific phases in the stars' evolution, as well as surface gravities, were determined from fitting synthetic photometric observations to a set of *Gaia* DR2 parameters. We used the "MESA Isochrones & Stellar Tracks" (MIST; Dotter 2016; Choi et al. 2016; Paxton et al. 2011, 2013, 2015) projects synthetic data to fit the evolutionary phase according to their classification. MIST doesn't feature subgiants as a distinct group but they can easily be distinguished from red giants through surface gravity. The phase was fitted using the version 1.2 "UBV(RI)c + 2MASS JHKs + Kepler + Hipparcos + Tycho + Gaia" grid of synthetic photometric data created for $[\text{Fe}/\text{H}] = 0.0$, $v/v_{\text{crit}} = 0.4$. We fitted the photometric grid for the effective temperature, luminosity, and G , BP, and RP magnitudes from *Gaia* DR2 of our sample to obtain the grid point that best matches all these parameters. Besides the surface gravities of the underlying stellar models and the classification of the evolutionary stage, the fit further revealed a set of 25 stars that were excluded in chapter 2 based on low surface gravity values that appear to be incorrect. They were identified from the MIST grid as MS stars and are excluded from the 267 remaining post-MS stars, leaving a set of 242 post-MS stars,

¹³<http://simbad.u-strasbg.fr/simbad/>

spanning subgiants, red giants, horizontal branch and asymptotic giant branch stars. It is this sample of stars that is shown in Figs. 3.1 and 3.2. Closer review of the results in Sect. 3.5 excluded one more star, HD87833, from the set. It had no rotational velocity listed in our two primary sources and the FWHM was acceptable, though Santrich et al. (2013) list it at a $v \sin i$ of 8 km s^{-1} , removing it from our sample. This leaves a final, trusted sample of 241 post-MS stars.

3.4. Technique

To determine the strength of convective blueshift for the stars in the sample, we followed the third-signature scaling approach (Gray 2009). In the following, we provide a short summary of the technique employed here and in chapter 2. For a more in-depth explanation we refer to Sects. 2.6 and 2.7 from chapter 2.

The core of the method is the concept of the third signature of granulation, the relation between a spectral lines' absorption depth and its radial velocity shift through convective motion (Hamilton & Lester 1999). It can be used as an alternative to the classical bisector approach, where connected midpoints of a single spectral line along points of equal absorption depth in the red and blue wing are used to trace convective velocity through the photosphere. The third-signature technique replaces the single line sampled at many depth points with many lines sampled at a single depth point each: Their core. This increases the number of required lines from one into the hundreds, but decreases the required signal-to-noise from $S/N \gtrsim 300$ to ≈ 100 and resolving power from $R \gtrsim 300\,000$ to $R \approx 50\,000$ as fitting a line core is much more robust than interpolating a bisector from the wings. This is especially true on the higher (close to the continuum) and lower (close to the core) end of the line profile due to noise combined with a small spectral slope. The lowered requirements, especially in resolving power, allow for the use of a much larger set of broad-band instruments, more than compensating the increase in line numbers necessary.

An additional advantage of the third-signature technique compared to the bisector approach is its universal nature. Unlike bisectors, which differ significantly even between lines of the same species in the same spectrum, the third signature of any star below the granulation boundary (Gray 2010a; $\sim 7000 \text{ K}$ on the MS; cooler for giants) can be scaled and shifted in velocity using a scaling factor S and offset to match any other star below the granulation boundary (Gray 2009). This allows for the use of a high quality template star, i.e. the Sun, to fit a model for its third signature and then calibrate and scale that template model to other instruments and stars, significantly improving the robustness of CBS determination. The calibration step is required to account for changes in instrumental broadening. In this chapter we use the same template as in chapter 2 for the solar blueshift velocity $v_{\text{conv},\odot}$ as it depends on the line absorption depth d :

$$v_{\text{conv},\odot}(d) = 601.110 \text{ ms}^{-1} \cdot d^3 + 173.668 \text{ ms}^{-1} \quad (3.1)$$

The template is based on the IAG solar flux atlas (Reiners et al. 2016) with a resolving power of $R \sim 1\,000\,000$ and created from a filtered list of spectral lines from the *Vienna Atomic Line Database*¹⁴ (VALD; Piskunov et al. 1995, Kupka et al. 2000, Ryabchikova et al. 2015; For details see chapter 2, Sect. 2.5.2). It is shown in Fig. 3.3, including the (binned) line measurements underlying the fit from the solar spectrum, but vertically shifted by 775 m s^{-1} such that $v_{\text{conv},\odot}(1.0) = 0$ to account for gravitational redshift and the motion of the Earth and telescope. The choice of vertical zero point is arbitrary as CBS is purely differential, without an absolute component. The template further needs calibration for the HARPS resolving power by 0.91 in scale and 21.2 m s^{-1} in offset to account for differences in instrumental broadening. These were implicitly applied at all points for the rest of this chapter.

A big advantage of obtaining CBS strength through third signature scaling instead of for example using the bisector inverse slope or other bisector indicators is that, in addition to the global CBS strength, it provides a velocity profile over all possible line depths. This profile allows for the construction of CBS values for the core of any spectral line of known depth even outside the initial list of measured lines. It further allows to reconstruct the lower parts of the bisector, where the intergranular contribution is weak, and serves as a proxy to the convective velocity profile within the range of optical depths belonging to the line forming region within the stellar photosphere.

For the rest of this chapter we used the same curated VALD line list used in chapter 2 to extract the third signature. All analyses, unless stated otherwise, were carried out the same way as those from chapter 2. We start by normalizing all spectra to the continuum by performing a boundary fit with asymmetric weighting and clipping factors, following a modified version of Cardiel (2009) and using a sinc^2 function to simultaneously account for the instrumental blaze function. We calculate an approximate RV from cross-correlating the normalized spectra with a binary line mask from CERES (Brahm et al. 2017), averaging over the echelle orders and determining the minimum as an initial RV estimate. We then

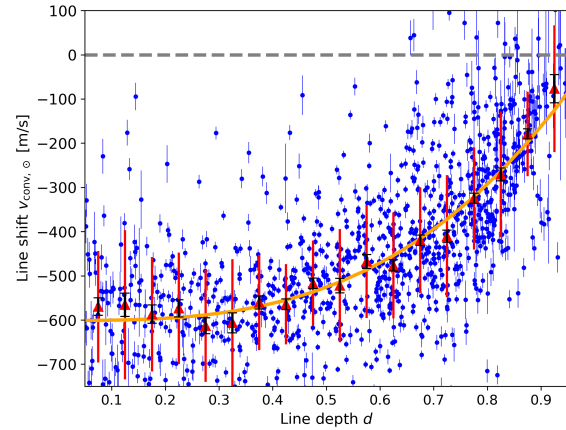


Figure 3.3.: Line shift vs. line depth for the solar template spectrum and the third signature of granulation template used in this chapter. This plot is modified from chapter 2, Fig. 2.5, center-left panel, with adjusted axes but using the same data, binning, and fitted signature. Marked are the 1168 individual spectral line measurements from the VALD list (blue points with errorbars), 18 bin medians (red triangles, errorbars are the median absolute deviation), error of the bin median (black errorbars, analogous to the error of the mean), and the template third signature (orange line, Eq. (3.1)).

¹⁴vald.astro.uu.se

fit the line list, determined in chapter 2, to the spectra, using parabolas to approximate the line core. We repeat the fit until convergence is reached, starting again from the supposed line center determined from the previous step to account for errors in the initial RV guess. After fitting the solar third signature template to the measured line center and depth values, the RV from the CCF is refined such that $v_{\text{conv}}(1.0) = 0$. This places a theoretical, fully absorbing line at zero RV shift under the assumption that it forms at the very top of the convection zone and should, therefore, show no convective velocity. Any deviation from zero would then necessarily be due to uncorrected RV. Measuring the lines and refining the RV is repeated until convergence to the final RV. For the full details we refer to chapter 2, Sects. 2.5 and 2.7.

3.5. Results

Applying the third signature scaling technique as described in Sect. 3.4 to MS stars in chapter 2 revealed a strong correlation between the strength of CBS and effective temperature, monotonously increasing from 20% solar strength plateau for late K dwarfs to 150% for mid to late F dwarfs. Figure 3.4 exemplifies the general results for the post-MS sample of this chapter compared to chapter 2. In a direct comparison between three post-MS stars, selected from this chapters data set, and three MS stars of near identical temperature from chapter 2, we see a significant increase in CBS strength for the post-MS stars compared to their less evolved MS counterparts. The difference between the post-MS stars and their counterparts also appears to grow with decreasing surface gravity, meaning for advancing evolution. The absolute CBS strength appears to dip for the intermediate case.

3.5.1. Temperature dependence of post-MS CBS strengths

The results from the full post-MS sample are given in Fig. 3.5. They match Fig. 3.4 and show the gradual deviation of the post-MS stars from the MS relation discovered in chapter 2. While the MIST stellar evolution grids do not list subgiants as their own stage, they are still easily identifiable through their surface gravity. Subgiants make up the transition between the MS relation and the post-MS "branch" between 5300 K and ~6000 K, leading smoothly into the RGB stars and terminating at AGB stars after passing horizontal branch stars. The entire post-MS sample forms its own "horizontal branch" in scale factor - effective temperature space at roughly solar strength CBS. We approximate the observed relation between Scale factor S and effective temperature T_{eff} with a third order polynomial to bins of ten stars each:

$$t = \frac{T_{\text{eff}} - 4400 \text{ K}}{1000 \text{ K}} \quad (3.2)$$

$$S(t) = 0.963 - 0.275 \cdot t - 0.317 \cdot t^2 + 0.442 \cdot t^3 \quad (3.3)$$

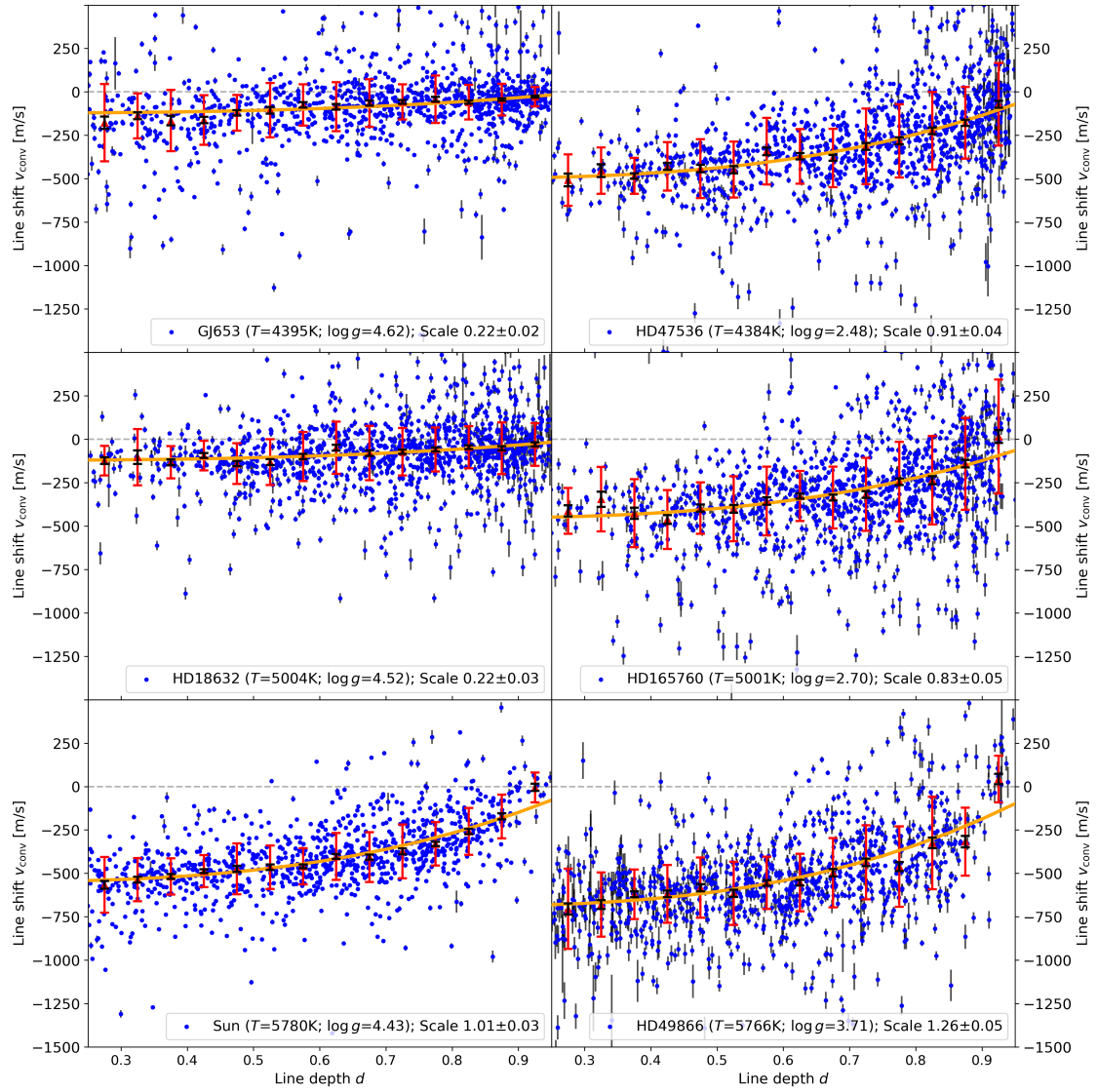


Figure 3.4.: Comparison of the convective blueshift of selected MS (left) and post-MS (right) stars of similar effective temperatures (rows) from the HARPS samples. The more advanced evolutionary stage can be inferred from the significantly decreased surface gravity $\log g$ for the stars on the right. Marked are individual spectral line measurements from the VALD list (blue points with errorbars), bin medians (red triangles, errorbars are the median absolute deviation), error of the bin median (black errorbars, analogous to the error of the mean), and the fitted third signature (orange line, scale factor in legend).

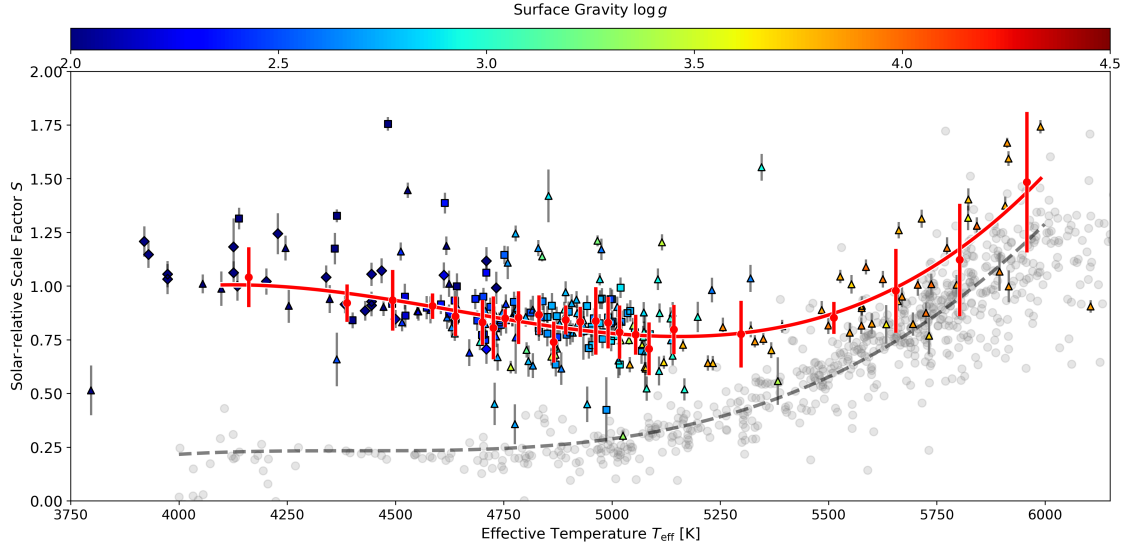


Figure 3.5.: Scale factor vs. effective temperature for the post-MS stars of the HARPS sample. The relation for the post-MS stars is fitted with a cubic polynomial (red line, Eq. (3.3)) to the binned scale factors (red errorbars), while the MS results (gray, dashed line for the fitted relation $S_{\text{HARPS,MS}}(T_{\text{eff}})$, gray markers for individual stars hotter than 4000 K; chapter 2) are included as reference. The surface gravity for each post-MS star (based on MIST fits) is color coded. The marker shapes correspond to the evolutionary phases according to MIST: sub- or red giant (triangle), core Helium burning (squares) and asymptotic giant (diamonds).

The effective temperature of the star is scaled in accordance with chapter 2 and the overall relation is fitted for the temperature region of 4100 K - 6000 K. Above 5800 K the two relations, for MS and post MS, fall together within the margin of error for terminal age main sequence (TAMS) stars, matching the turnoff within the HRD in Fig. 3.1. An overview of the CBS strength expected from the fit is given in Table 2.4 for a selection of effective temperatures within the fitted range.

3.5.2. Surface gravity dependence of post-MS CBS strengths

Plotting the derived scale factors S against the surface gravity $\log g$ instead of temperature shows a similar picture due to the dependence of the two but also clearly shows an intermediate decrease in scale factor for the youngest subgiants, showing a minimum around $\log g \approx 3.2$ (Fig. 3.6). Fitting the relation with a third order polynomial, as with eqn. (3.3), gives:

$$S(\log g) = 0.129 + 1.488 \log g - 0.742 (\log g)^2 + 0.106 (\log g)^3 \quad (3.4)$$

The intermediate dip in S is in agreement with results from Luhn et al. (2020), who investigated RV jitter levels due to activity and granulation. They also found a minimum in RV jitter depending on surface gravity and stellar mass, that separates an "activity

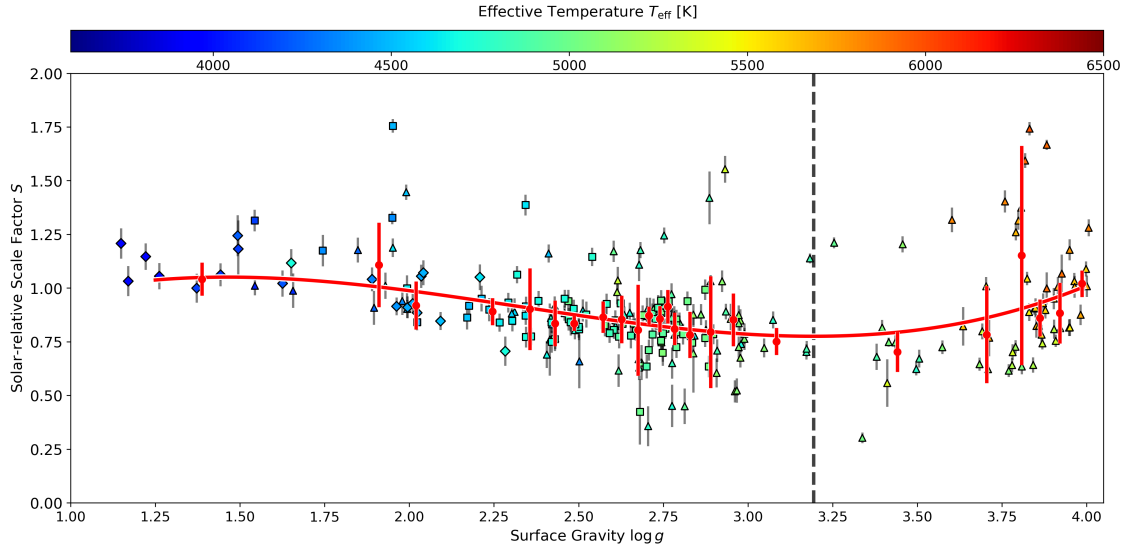


Figure 3.6.: Scale factor vs. surface gravity (based on MIST fits) for the post-MS stars of the HARPS sample. The relation $S_{\text{HARPS,pMS}}(\log g)$ for the post-MS stars is fitted with a cubic polynomial (red line). The effective temperature for each star is color coded. The marker shapes correspond to the evolutionary phases according to MIST: sub- or red giant (triangle), core Helium burning (squares) and asymptotic giant (diamonds). A local minimum in scale factor at $\log g \approx 3.2$ is marked (gray, dashed line).

dominated” and a ”granulation dominated” phase during a stars evolution. For a median mass of 1.78 solar masses in our sample they predict a jitter minimum at $\log g \approx 3.1$ of 5.5 m s^{-1} , coinciding with the minimum observed in our results. This could indicate a ”sweet-spot” where granulation induced RV jitter and CBS are both minimal, reducing the difficulties encountered by high-precision planet searches (Sect. 3.2 for details).

3.5.3. Comparison with literature results

The results for post-MS CBS strengths are in qualitative agreement with the results from [Gray \(2009\)](#), who also shows an increase in CBS for more evolved stars, however they differ on a quantitative level with the [Gray \(2009\)](#) results showing significantly higher scale factors for the most evolved stars. We performed a thorough investigation into the source of this discrepancy as described in Appendix 3.7. We conclude that it is not a matter of instrumental differences, nor directly due to differences in the choice of lines used but due to a different ”standard curve” (Gray) or third-signature model (our term) created from a different set of lines that scales differently with temperature. As such the results only appear to be in disagreement as they are not quantitatively comparable due to the scaling difference of the underlying relation. A similar disparity was found in chapter 2 when comparing our results for MS stars against [Meunier et al. \(2017b\)](#) and [Meunier et al. \(2017c\)](#). They used a linear approximation as their third-signature model, resulting

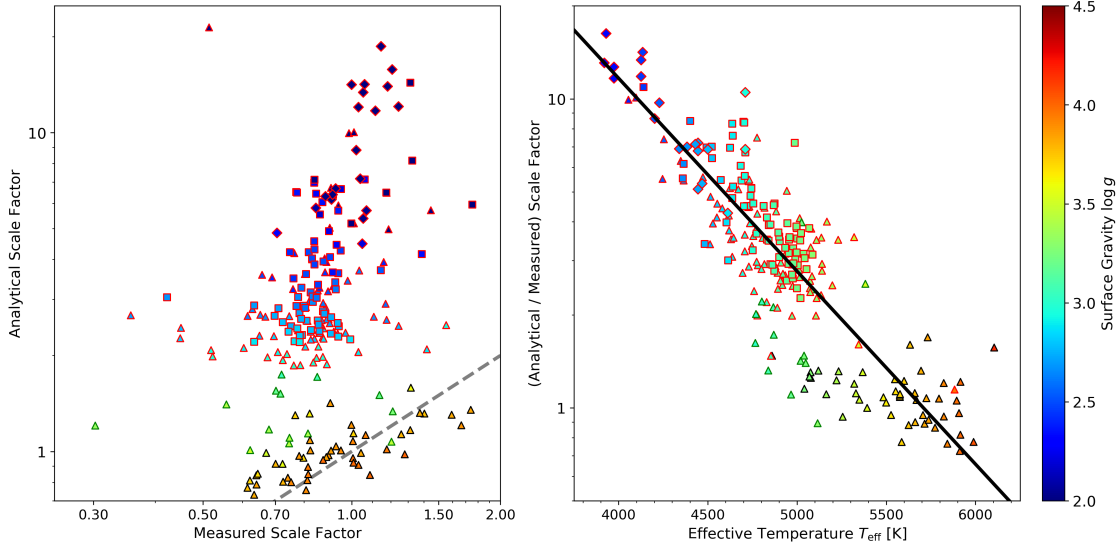


Figure 3.7.: Left: Comparison of scale factors measured from the HARPS post-MS sample against values expected from the [Basu & Chaplin \(2017\)](#) analytical relations. The gray, dashed line shows equality. Right: Ratio of scale factor values expected from the [Basu & Chaplin \(2017\)](#) analytical relations (Eq. 3.5) and measured from the HARPS post-MS sample. The black line was fitted as a correction factor to the analytic values as a function of effective temperature. Both: Markers are colored for surface gravity (based on MIST fits). Black edges indicate $\log g > 3.5$, green $3.5 > \log g > 3.0$ and red $3.0 > \log g$. The marker shapes correspond to the evolutionary phases according to MIST: sub- or red giant (triangle), core Helium burning (squares) and asymptotic giant (diamonds).

in an underestimation of the scaling towards hotter stars due to the strong curvature of the third signature.

3.5.4. Comparison with analytical models

While the discrepancy with the results by [Gray \(2009\)](#) could be resolved, it leaves the question whether our scale factors are under similar limitations. To that end, following chapter 2, we again attempt to match our measurements to the analytical scaling relation for the observed CBS S_{BC} , called $\sigma_{c,v}$ by [Basu & Chaplin \(2017\)](#) (Eq. (4.79) in their work), with effective temperature T , stellar radius R and stellar mass M , shown in Eq. (3.5).

$$S_{BC}(T, R, M) \approx T^{41/9} R^{13/9} M^{-11/9} \quad (3.5)$$

In chapter 2, we were able to match our scale factors either for MS stars below or above 5400 K, though not for the entire range at once as the scaling with temperature for the hotter range appears stronger than analytically expected. The relation also did not reproduce the plateau for K-type MS stars. We concluded that this was due to the underlying

assumption by [Basu & Chaplin \(2017\)](#) that individual Granules contribute the same level of intensity fluctuations irrespective of spectral type. This impression is reinforced after we compare the current results for post-MS stars to the [Basu & Chaplin \(2017\)](#) relation. Using the stellar parameters obtained from the MIST fits (Sect. 3.3.2) and obtaining the radius from the model mass and surface gravity as radius is not a listed parameter, it is possible to match the scale factors for TAMS and young SG stars (Fig. 3.7, left panel).

At a surface gravity $\log g < 3.5$ the scale factors obtained from the analytical relation start to overestimate our empirical measurements and for $\log g < 3.0$ predicts a strong increase with further decreasing surface gravity. We only see a very slight increase in CBS scale factor in our data for that region, which corresponds to the transition between SG and the actual RGB. From the fundamental structural changes experienced during that phase it is unsurprising that the relation breaks under the given assumptions. As with the MS sample, we are of the opinion that this is due to changes in the balance factor between Granules and lanes. Comparing the model from [Basu & Chaplin \(2017\)](#) on the number and therefore size of the Granules with numerical results from [Trampedach et al. \(2013\)](#) shows a good agreement, reinforcing our opinion. Finally, [Trampedach et al. \(2013\)](#) directly show that the intensity contrast increases as the star evolves, explaining the deviation from the analytical model. Since the deviation of our empirical CBS strengths from the analytical expectation appears to be smooth, we can attempt to derive a correction term. The right panel of Fig. 3.7 shows the ratio of the analytical and the empirical strength of CBS (S_{BC} and $S_{HARPS,pMS}$ respectively) for the post-MS (pMS) sample as a linear function of temperature in semi-logarithmic space. Fitting the relationship gives Eq. (3.6), which can be used to empirically correct the analytically derived values from [Basu & Chaplin \(2017\)](#).

$$\log_{10} \left(\frac{S_{BC}}{S_{HARPS,pMS}} \right) = -0.6244 \frac{T_{\text{eff}}}{1000 \text{ K}} + 3.564 \quad (3.6)$$

3.5.5. Relation to macroturbulence velocities

The third signature of granulation was termed as such by [Gray \(2009\)](#) as an extension to the existing first and second signature: The macroturbulent dispersion and spectral line asymmetry respectively. They showed that for their sample of eleven stars the first and third signatures are correlated, with the exception of ι Aurigae which showed an excessively high radial-tangential macroturbulence dispersion (called v_{mac} here, they called it ζ_{RT}). Since we already found a systematic difference to the [Gray \(2009\)](#) scale factors due to differences in the derived third signature (Sec. 3.5.3 and Appendix 3.7) and saw evidence for the same overestimation of non-empirical CBS proxies as they see for ι Aurigae (Sect. 3.5.4), comparing our scale factors to macroturbulent broadening was of high interest.

Doyle et al. (2014) determined v_{mac} values for 28 stars from the Kepler input catalog, accounting for the influences of instrumental broadening as well as microturbulence. The effect of rotational broadening was mitigated by using asteroseismic $v \sin i$ values to disentangle the broadening from macroturbulence. From their results they provide a fitted relation to determine the expected v_{mac} value from effective temperature and surface gravity. Figure 3.8 shows the result of plotting the velocities obtained that way against our scale factors. The picture is similar to Fig. 3.7 with subgiant scale factors correlating well with v_{mac} and more evolved stars expected to show a much higher velocity than the scale factors indicate. While the extent is larger, possible due to the larger number of stars in our sample highlighting the deviation, this mirrors the result from ι Aurigae in Gray (2009), where v_{mac} was directly determined, rather than from a parameterized relation. It must be noted that the relation from Doyle et al. (2014) was only calibrated to MS stars, although the values obtained are within the region of those obtained by Gray (2009). The origin of this discrepancy in behavior among the more evolved stars is unclear at this point. The agreement between the magnitudes of v_{mac} in the two works and the consistency with the behavior observed in Sect. 3.5.4 indicates it is likely that the relation remains applicable to the giant regime as far as macroturbulence is concerned. Gray & Pugh (2012) also found a similar behavior with respect to macroturbulence while remaining consistent in velocity magnitude for an extended sample of giant and supergiants stars. A potential source is the fact discussed in both works that the macroturbulence velocity determined depends strongly on the depth of the lines under observation, for the same reason that CBS does. While the scale factor intrinsically accounts for this through the depth-dependent third signature model, the v_{mac} values are only strictly correct for the line and star combination it is determined from because the line changes depth between stars. Even averaging multiple lines, as was done by Doyle et al. (2014), may only partially mitigate this for small numbers of lines as was seen in Appendix 3.7 as they can still show systematically different behavior compared to another set of lines. It is therefore possible that changes to the formation heights of the lines utilized lead to a change in v_{mac} not present in our scale factor by shifting the sensitivity to deeper layers of the photosphere for more evolved stars. The explicit depth-dependence of the third signature avoids this effect. Alternatively, as raised for discussion in Gray & Pugh (2012), it is conceivable that for evolved stars the assumption behind the definition of macroturbulent broadening as a measure of convection (and proxy for CBS) breaks down. Macroturbulence measures a form of "convective broadening" that is dominated for the solar-like case by the granular blueshift. The changes in contrast and areal coverage mentioned in Sect. 3.5.4 could lead to an increase of the intergranular redshift contribution which would increase convection broadening from additional redshifted components while decreasing the line core shift by countering the granular velocity more strongly, effectively decoupling the first and third granulation signature for evolved stars.

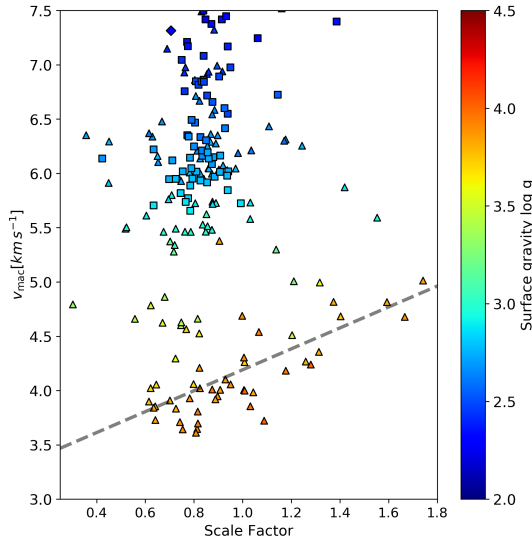


Figure 3.8.: Comparison of macrodispersion, determined from the [Doyle et al. \(2014\)](#) fit, and our HARPS pMS scale factors. The gray, dashed line shows a linear fit to the subgiants with $\log g < 3.6$. Markers are colored for surface gravity (based on MIST fits). The marker shapes correspond to the evolutionary phases according to MIST: sub- or red giant (triangle), core Helium burning (squares) and asymptotic giant (diamonds).

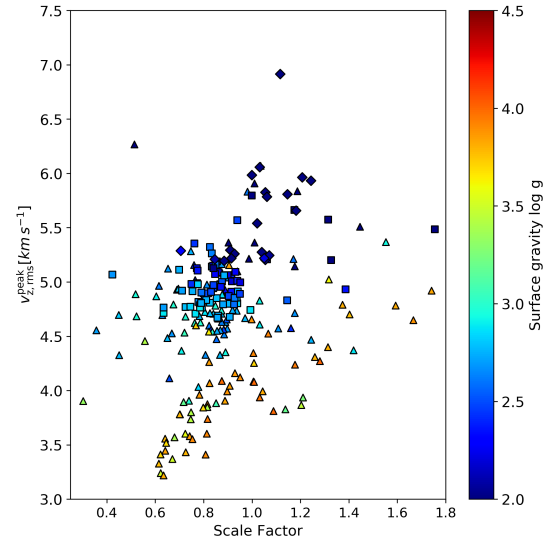


Figure 3.9.: Comparison of horizontally averaged, peak vertical velocities from [Magic et al. \(2013\)](#) fits to STAGGER 3D MHD model atmospheres. Markers are colored for surface gravity (based on MIST fits). The marker shapes correspond to the evolutionary phases according to MIST: sub- or red giant (triangle), core Helium burning (squares) and asymptotic giant (diamonds).

3.5.6. Convection velocities from 3D MHD

After identifying two alternatives to the scale factors determined in this chapter that systematically deviate in similar and potentially related ways, a third option is to investigate the actual convection velocity of the material within the convection zone. These velocities can be extracted from 3D MHD simulations such as from [Magic et al. \(2013\)](#). From their STAGGER grid of 3D MHD model atmospheres they provide the horizontally averaged, peak vertical velocities $v_{z,rms}^{peak}$ together with a functional fit dependent on metallicity, temperature and surface gravity. Assuming solar metallicity for our stars for simplicity, since the influence is significantly weaker than for the other two parameters, we obtain Figure 3.9. Once again we see the structure of more evolved stars clustering above the well correlated subgiants, although this time the tail pointing upwards is missing in favor of a denser cluster. The correlation between the scale factor and $v_{z,rms}^{peak}$ for the subgiants also appears less strict than for the previous two comparisons with those that show weaker CBS turning slightly downwards. It should be noted that $v_{z,rms}^{peak}$ denotes the peak velocity within the atmosphere model which extends below the photosphere and as such will overestimate the maximal possible velocity component within the line forming region. [Magic et al. \(2013\)](#) mention this but claim that the peak velocity still scales in accordance with the global

velocity magnitudes. On the other hand they state that surface gravity has an effect on the symmetry of the velocity curve, changing the velocities encountered at given optical depths by shifting the peak to higher optical depths. This may lead to lower velocities within the line forming region, albeit the peak velocity keeps increasing. Furthermore, they use an rms value as their horizontal average thereby excluding the cancellation between rising and sinking material and introducing a bias compared to only the granular regions. Similar to the fixed cancellation factor in Sect. 3.5.4 and the decoupling of convective broadening from the core shift in Sect. 3.5.5, this would lead to an overestimation of observable CBS velocities within evolved stars where the convective pattern changes drastically to a more even distribution between rising and falling material. A more definitive answer to this question could be reached by employing radiative transfer simulations on the atmosphere models to investigate the actual formation depths of spectral lines but this far exceeds the scope of the present work.

3.6. Summary and Conclusion

We investigated 242 post-MS stars, using the third-signature scaling technique, to determine the largest cohesive sample of CBS strengths to date. The technique has previously proven to be robust over a large range of temperatures for MS stars while combining the quality advantage of an ultra-high quality solar template with the increased ease of obtaining lower quality spectra. We expanded on the results from chapter 2 in several ways.

- We confirmed that the technique is applicable reliably and without issues for stars past the MS, extending the confirmed range of universal scaling of the third signature.
- Our results qualitatively confirm findings by [Gray \(2009\)](#), that post-MS stars show increased CBS compared to MS stars of similar temperature.
- Quantitative differences are due to the choice of line lists and the resulting fundamentally different third-signature template, which demonstrates a different scaling behavior.
- We were able to determine that post-MS stars form a "horizontal branch" in scale factor versus effective temperature space. This gradually increases the CBS strength difference towards cooler temperatures, lower surface gravity and further evolved stars, as the MS stars continue to decrease in CBS.
- We found that subgiants gradually turn off of the MS relation towards the "horizontal branch" of the post-MS stars after a slight minimum around $\log g \approx 3.2$.
- This minimum may indicate a "sweet-spot" for planet searches as it coincides with a minimum in RV jitter ([Luhn et al. 2020](#)).

- The near constant scale factor indicates that CBS changes very little between evolved stars which disagrees with findings from analytical scaling (Basu & Chaplin 2017), macroturbulent broadening (Doyle et al. 2014) and MHD convection velocities (Magic et al. 2013). It is likely that this is due to the disconnect between line core shifts, susceptible to a fine balance between granular blue and intergranular redshift that the three proxies are insensitive towards.

With this chapter we have demonstrated again the ease of use and generality of the third-signature scaling technique. It is very robust and applicable on a wide range of not only effective temperature but also evolutionary stage and, after a simple calibration for differences in instrumental broadening, the instrument used to record the data. This establishes the applicability to a very wide range of use cases, encompassing the entirety of stars with convective envelopes recorded at medium resolution or higher.

3.7. Appendix

Further investigations

We found that quantitatively our results for the scale factor and those from Gray (2009) differ by up to a factor of three ($S \sim 0.27$ versus $S \sim 0.72$ for the late K dwarf ϵ Eridani). We investigated this difference first by looking for stars included in his sample as well as ours. This left us with ϵ Eridani and τ Ceti, both MS stars and both showing significantly lower scale factors in our analysis, though τ Ceti deviates only by a factor of two (0.56 versus 1.01). We endeavored to exclude an instrumental source for the difference, albeit that Gray (2009) cites a resolving power of his spectra comparable to HARPS, and analyzed a number of published PEPSI spectra from Strassmeier et al. (2018) (HR diagram for the sample in Fig. 3.10). The results, as shown in Fig. 3.11, agree with our HARPS sample within the margin of error, both for MS and post-MS stars, reinforcing the systematic difference to Gray (2009).

Besides the instrument, which we have shown to not be the source, another difference lies in the choice of spectral lines. Where we use a general list, not specifically curated to any degree and only vetted to optimize third-signature fit quality among the entire sample over all spectral types, with a total of over 1000 lines, Gray (2009) uses a list of 15 lines of Fe I that are easy to measure in the Sun. As we pointed out in chapter 2, from our own experience, care must be taken to ensure a list of lines is generally applicable and not overly adapted to any specific type of star, lest the results become unreliable once applied to an unsuited star. To check if this was the case here, we repeated our analysis with the line list provided by Gray (2009), but retaining our third-signature model (Eq. 3.1). The results are shown in Fig. 3.12. Besides a generally larger scale factor that could be calibrated for (solar fit at $S \sim 2.1$), they agree again with our results from chapter 2. While the uncertainties are larger, as is the scatter of individual stars, this eliminates the line list as a source for the deviation as well, especially as the Gray (2009) MS stars also match

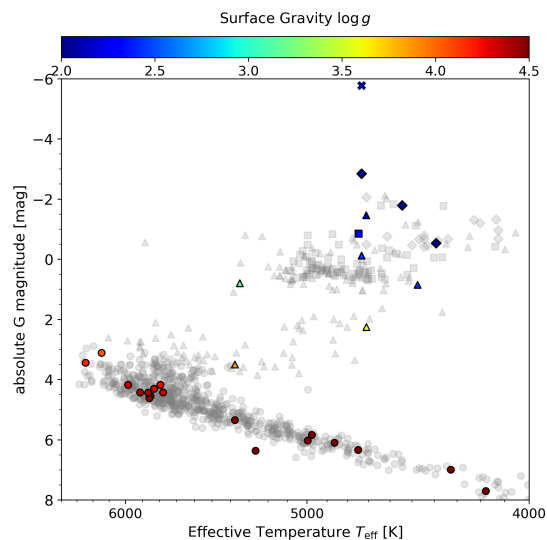


Figure 3.10.: Hertzsprung-Russell diagram for our control sample of PEPSI stars based on *Gaia* DR2 data and colored for surface gravity (based on MIST fits). The HARPS MS/post-MS sample from chapter 2 and this chapter is included as reference (gray markers). Three PEPSI stars are not shown due to missing *Gaia* parallaxes. The marker shapes correspond to the evolutionary phases according to MIST: main sequence (circle), sub- or red giant (triangle), core Helium burning (squares), asymptotic giant (diamonds), extended asymptotic giant (stars), and thermally pulsing asymptotic giant (crosses).

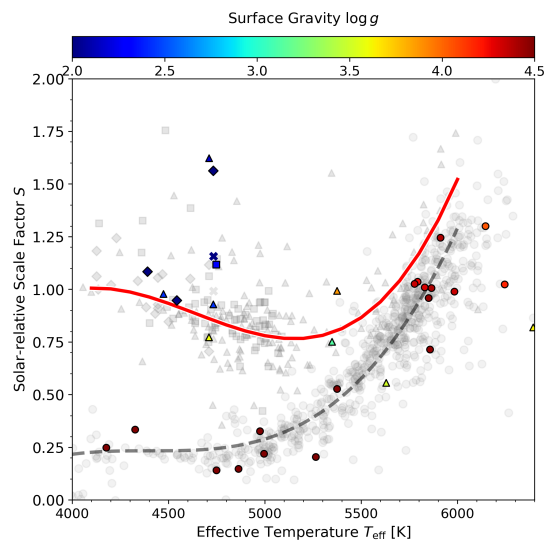


Figure 3.11.: Scale factor results for the PEPSI control sample (colored for MIST surface gravity). Both MS and post-MS scales are in agreement with the main HARPS sample models (gray and red curves for the fitted models, gray markers for individual stars from the samples of chapter 2 and this chapter). The marker shapes correspond to the evolutionary phases according to MIST: main sequence (circle), sub- or red giant (triangle), core Helium burning (squares), asymptotic giant (diamonds), extended asymptotic giant (stars), and thermally pulsing asymptotic giant (crosses).

our MS relation after recalibration. This further matches our experience with the results from [Meunier et al. \(2017b\)](#) and [Meunier et al. \(2017c\)](#), where general agreement was reached with the results in chapter 2, despite a significant difference in line list.

As a last option we compared our solar-based third-signature model to the one used by [Gray \(2009\)](#) and [Gray & Oostra \(2018\)](#). We applied a correction to our model in the form of an RV shift to account for the different treatment of barycentric motion and solar gravitational redshift and compared the two models. However, the difference in absolute RV shift is not the source of the differences in the results as an absolute shift is already a fitted parameter for the third signature scaling and, unlike the CBS strength itself, not a differential shift. As such it does not change the determined CBS strength and can not account for the difference in results. A direct comparison of the two models in Fig. 3.13 reveals a clear difference in that the [Gray \(2009\)](#) model curves up, towards weaker CBS, for significantly shallower lines. Shifting that model by 20 percentage points towards deeper lines and adjusting absolute RV results in an almost perfect match to our model

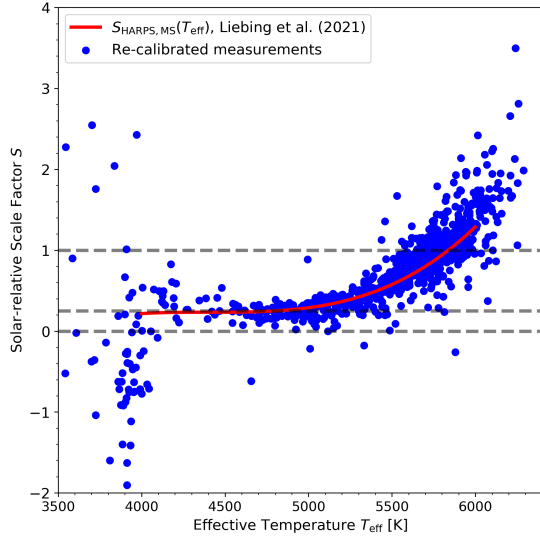


Figure 3.12.: Scale factor vs. effective temperature for the HARPS MS sample from chapter 2, using the 15 lines from Gray (2009) and our solar 3rd signature, pre-scaled by a factor of 2.1 to account for the systematic difference due to the line choice. The resulting re-calibrated scale factors (blue dots) are indistinguishable from the fit to the results from chapter 2 (red line, Eq. (2.3) from chapter 2). The dashed lines mark scale factors of zero, one (solar strength) and 0.25 (K dwarf plateau from chapter 2).

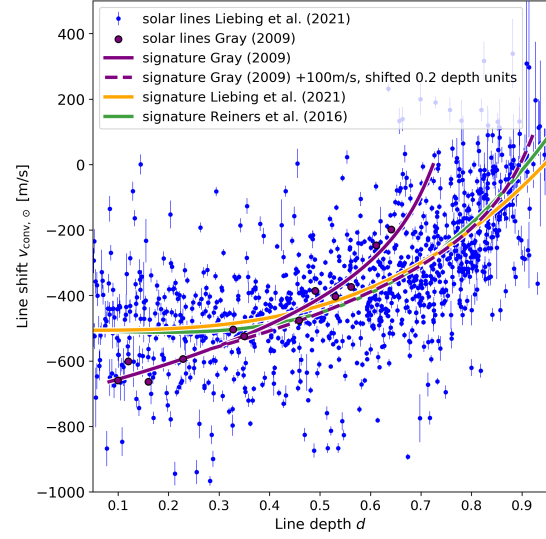


Figure 3.13.: Comparison of the Gray (2009) line measurements and standard curve $F/F_c(v)$ for the Sun with our equivalent third signature $v_{\text{conv},\odot}(d)$ determined in chapter 2 (Eq. 3.1, see also Fig. 3.3 of this chapter) and the Reiners et al. (2016) signature.

and the one from Reiners et al. (2016). We speculate however, that this offset is not due to actual differences in the spectra or measurements of the line depths, but rather a result of the choice of lines leading to a sub-optimal third-signature template. Directly comparing measurements using our technique but the line list from Gray (2009) against the extracted line data from Fig. 7 from Gray (2009) for the Sun (a $R \sim 100\,000$ degraded IAG atlas in our case) reveals a good agreement among the two and to the "standard curve" from their work. The fact that our template model requires a scaling of 2.1, rather than 1.0 as one would expect for a fit to solar lines, indicates that the choice of lines is not representative for the overall third signature shape and CBS strength of the Sun. This is shown in Fig. 3.13, where we compare Gray (2009) line measurements and standard curve with our equivalent line-by-line results from chapter 2. We clearly see the discrepancy in standard curve / third signature template is purely due to the choice of spectral lines, as all the lines chosen by Gray (2009) are within the range covered by our own choice of line list. As such, the results are not in actual disagreement, despite the difference in similar sounding values, but are simply not directly comparable.

We have shown in chapter 2 that there is a degeneracy between observed line depth, influ-

enced by line broadening effects, and resulting scale factor. This resulted in the necessity to calibrate the template to the resolving power of the instrument, to account for instrumental broadening, that would otherwise lead to a similar offset in measured solar CBS scale factor. This further explains the growing discrepancy in published scale factors between this chapter and [Gray \(2009\)](#) for decreasing effective temperatures for τ Ceti and ϵ Eridani as the underlying signature is fundamentally different and therefore scales differently as well, in this instance much slower. As such our results and those of [Gray \(2009\)](#) appear to both be valid within their context and simply not directly comparable. This again matches our observations from chapter 2 against [Meunier et al. \(2017b\)](#) and [Meunier et al. \(2017c\)](#), where a linear third signature model led to similar issues, though at higher scale factors, as there the model underestimates the true third signature curvature.

Tables

For ease of access and a quicker overview, we list in Table [3.1](#) the expected CBS strengths and velocities for the range of 4100 K - 6000 K based on our model from Eq. [3.3](#). Table [3.2](#) lists all stars of our sample with basic parameters important to this chapter and the determined CBS strengths and uncertainties. The full Table is available via CDS.

Table 3.1.: Scale factor cheat sheet following Eq. 3.3.

Effective temperature [K]	Scale factor	Velocity [m s^{-1}]
4100	1.005	-361.3
4200	1.002	-360.1
4300	0.987	-354.7
4400	0.963	-346.2
4500	0.933	-335.3
4600	0.899	-323.1
4700	0.864	-310.6
4800	0.831	-298.6
4900	0.802	-288.1
5000	0.780	-280.2
5100	0.767	-275.6
5200	0.767	-275.5
5300	0.781	-280.7
5400	0.813	-292.2
5500	0.865	-311.0
5600	0.940	-337.9
5700	1.041	-374.0
5800	1.169	-420.2
5900	1.329	-477.5
6000	1.521	-546.8

Notes. The velocities given assume a line depth of 0.7 (Eq. 3.1), corresponding to a median solar line.

Star	DR2 ID	T_{eff}	G_{mag}	$\log g$	Phase	$v \cdot \sin i$	#Spectra	S/N	#Lines	χ^2_p	Scale S	σ_S
HD56618	5606936597846401024	3797	-1.73	0.90	RGB	—	5	544	923	0.92	0.51	0.12
HD41047	2889305249701803008	3920	-1.60	1.15	AGB	—	9	462	1095	0.03	1.21	0.07
HD12524	4944212458182232064	3930	-0.93	1.22	AGB	—	9	523	1118	0.24	1.15	0.06
HD61772	3029166186779364864	3974	-2.39	1.17	AGB	—	35	1347	1141	0.07	1.03	0.07
HD45669	5278749385021344768	3974	-1.56	1.26	AGB	—	7	353	1109	0.03	1.06	0.06
HD130694	6219380139468557312	4055	-0.89	1.54	RGB	—	194	3039	1165	0.03	1.01	0.04
BD-184705	4119382783830154240	4098	-0.33	1.66	RGB	—	13	160	1053	0.27	0.99	0.08
TYC5126-2775-1	4252502954347971584	4126	-0.68	1.50	AGB	4.50	8	88	1013	0.05	1.18	0.13
HD50778	2952868119981800448	4126	-0.96	1.44	AGB	3.60	7	392	1122	0.01	1.06	0.05
HD28028	4871775051596979200	4135	-1.32	1.37	AGB	—	7	474	1121	0.04	1.00	0.07
TYC8963-1543-1	5336820469612710912	4139	-0.42	1.54	CHeB	—	21	184	1084	0.48	1.31	0.05
HD170053	4477460391998885888	4202	-1.21	1.63	AGB	—	102	1433	1172	0.04	1.02	0.06
BD+101802	600784874384342400	4229	-1.30	1.49	AGB	—	3	247	1034	0.53	1.24	0.10
HD45398	3104552174309523968	4246	-0.78	1.85	RGB	—	105	1648	1169	0.02	1.18	0.06
BD-184710	4119382852549575168	4254	-0.40	1.90	RGB	—	16	220	1091	0.11	0.91	0.08
HD122430	617743296478425088	4340	-0.67	1.89	AGB	2.59	7	370	1157	0.03	1.04	0.05
CD-546003	5887641435423836160	4348	-0.52	1.98	RGB	—	7	185	1104	0.04	0.94	0.06
HD96789	5340186143451129856	4360	-1.77	1.74	CHeB	—	7	339	1122	0.31	1.17	0.07
COROT102387834	3317885502001094656	4364	1.75	2.50	RGB	—	17	64	1007	5.29	0.66	0.12
HD10615	4715993838992279552	4365	-0.07	1.95	CHeB	—	9	366	1158	0.02	1.33	0.03
HD47536	5583831735369515008	4384	-0.62	1.96	AGB	1.81	11	485	1182	0.03	0.91	0.04
HD85859	5659110864115635200	4401	-0.06	2.02	CHeB	—	10	703	1145	0.04	0.84	0.04
HD65695	306899225306100736	4430	-0.45	2.02	AGB	2.00	10	568	1189	0.07	0.88	0.05
HD110014	3676091134604409856	4445	-0.78	2.04	AGB	3.90	111	2253	1187	0.01	1.05	0.05
HD178484	4261348186123153408	4445	-0.42	2.01	AGB	—	146	1880	1201	0.03	0.93	0.05
HD1690	2430036837596487680	4445	-0.68	2.00	AGB	3.02	44	363	1141	0.07	0.91	0.05
HD132944	5887670572485812224	4468	-0.66	2.04	AGB	—	8	239	1101	0.08	1.07	0.06
HD206642	6585580939594718208	4472	-1.24	1.99	RGB	—	3	525	1163	0.06	0.90	0.04
HD78004	5330160246630987776	4483	-1.13	1.95	CHeB	—	4	420	1173	0.87	1.75	0.03
CD-4911415	5949577646955571200	4492	0.30	2.18	CHeB	—	34	234	1137	0.06	0.92	0.04
HD171759	6419476											

4. Summary and Conclusion

In this thesis, multiple sources of stellar variability, primarily in the form of stellar activity, were investigated. The nature of stellar oscillations was introduced in Section 1.4.1. Their behavior over a vast range of stellar types, from the low and intermediate mass main sequence to red giants, was explored and workable mitigation procedures presented. The effects of starspots, particularly their flux effect, was explained in Section 1.4.2. Realistic surface maps for spotted stars of different types and activity levels, incorporating size distributions and contrast ratios, were created to model line profile changes and resulting RV variations. The role of magnetic suppression of convective blueshift was detailed, starting from the phenomenon of stellar convection, the formation of the granulation pattern, emergence of CBS and the difficulties in its mitigation due to faculae. The main part of this Thesis is formed by the development of a technique to directly and robustly measure the strength of convective blueshift without having to rely on proxies or model assumptions. Instead a purely empirical approach was taken using a template derived from solar observations that was then applied to two samples of stars observed by HARPS: One of main sequence stars and another of more evolved subgiant, red giant and asymptotic giant stars. The results obtained during the template creation process and from the two stellar samples are summarized and discussed in this chapter. Beyond that, the results are put into context regarding points raised in the introduction, particularly Sections 1.3 and 1.4.3, and potential use cases for these directly obtained CBS strengths are explored.

4.1. A solar template for stellar convection

Following the approach outlined in Section 1.5, a template for the third signature of granulation was determined from an ultra-high resolution ($R \sim 1\,000\,000$) Fourier transform spectrum of the Sun, published as a solar atlas by [Reiners et al. \(2016\)](#). To this end, an iteratively cleaned list of spectral line positions was composed, starting from a VALD list of absorption lines for a 3750 K, $\log g = 5.0$ star (for the cleaning procedure, see Section 4.2).

Each spectral line position in the list was fitted with a parabola to find the line center within the solar spectrum and determine its depth relative to the continuum. The fitting procedure operates on an iterative basis, refining the initial guess from the list of rest wavelengths by repeatedly fitting parabolas to the center of the previous guess and using the minimum position as the starting point for the next step. This allows for the use of a

narrower fitting window, preventing potential contamination from asymmetric line wings, while not requiring the initial guess to be exact to within the window width. Instead, the clamped refinement steps allow the fit to slide into the line core even if it originated up the wings due to inaccuracies of the initial RV correction and converge to the actual minimum, as long as the initial guess falls within the line profile.

The accuracy for the procedure was verified by re-computing the positions of the lines used in [Reiners et al. \(2016\)](#), showing a near identical match, and by employing synthetic lines with Gaussian profiles and Poisson noise applied. The synthetic test showed a precision in depth of better than 1% and a positional accuracy of 40 m s^{-1} . The determined line shifts were plotted against the depths to obtain the solar third signature. The data was binned by absorption depth and fitted with a third order polynomial to obtain the solar template used from here on. To account for instrumental broadening and the corresponding decrease in observed line depths, this high quality template was calibrated against measurements of the solar atlas after it was degraded to the resolution of the HARPS instrument ($R \sim 100\,000$). From a general analysis of degraded atlas data it was determined that this would be possible down to a resolving power as low as 50 000 at no significant loss of precision. Below that, precision decreases until the results break down around $R \sim 10\,000$. Similarly, rotational broadening can affect the results if the star rotates faster than about 8 km s^{-1} at HARPS resolving power, corresponding to an overall broadening FWHM of 14 km s^{-1} that forms the upper boundary of the methods' applicability. Testing the solar spectrum under additional Poisson noise revealed a lower bound of $S/N \sim 100$ before precision starts to degrade.

Besides this broadband third signature, the quality of the solar data allowed for the determination of chromatic changes to the third signature. A clear decrease of CBS with wavelength was found, once the depth dependence was removed through binning. Previously disputed in the literature, a chromatic model was created based on the data that explains nearly the entire scatter observed for deeper lines. It was shown that previous disproofs of CBS chromaticity did not take into account the wavelength dependent distribution of line depths, where shorter wavelengths feature more deep lines with less CBS. For the Sun the two effects happen to cancel out within the visible range.

4.2. Convection along the main sequence

From a sample of 3094 stars observed by the HARPS spectrograph, a sample of 810 main sequence stars was identified. Stars that could not be matched to the *Gaia* DR2, had no rotational velocity listed in SIMBAD, rotate faster than 8 km s^{-1} , exceeded the HARPS DRS FWHM of 9 km s^{-1} or were classed as post-MS based on a combination of $\log g$, T_{eff} and G_{mag} were discounted. The spectral type of the MS stars was estimated from *Gaia* color indices and the coadded spectra normalized to the continuum with an asymmetrically weighted, kappa-sigma clipped fit of a sinc^2 function to correct for the instrumental blaze function while excluding very strong absorption lines and Ca H+K emissions from

the fit without the need for masking or multi-step processes. The absolute radial velocity of each star was determined as a first approximation from a cross-correlation of the spectrum with a binary line mask. The CCF of each echelle order were added and the minimum in velocity space taken as the initial RV. The third signature measurements were performed as summarized in Section 4.1, using the list of lines from VALD after correcting for the determined RV. The solar template was scaled and shifted in velocity to match the binned line-by-line measurements from the HARPS stars, instead of redefining a third order polynomial for every star. This retains the quality of the solar data in the accurate shape of the template signature. Under the assumption that a fully absorbing line should show a CBS of zero, as it is formed at the very top of the convection zone, the RV is refined to account for any discrepancy and the measurement repeated until no more refinement is necessary. After the RV has converged for all stars, all spectral lines' residual from the third signature scaling fit are averaged over all stars in the sample to determine their efficacy in determining the third signature strength and all lines removed from the list that don't belong to the 25th percentile in mean residuals, i.e. that give systematically higher residuals, and the 50th percentile in standard deviation of the residual, i.e. which show strong variations in their efficacy for third signature determination. The solar template is recreated with this refined list, showing only minor changes, and the scale factors of the template for the HARPS sample redetermined. The line list was evaluated for its susceptibility to magnetically sensitive lines and telluric contamination, both of which could be refuted. Similarly, the original choice of a VALD extraction at 3700 K could be shown to have had no significant effect.

It could be shown that third signature scaling works well over a large range of temperatures, from 3800 K until 6000 K, and extends over the entire range of observed line depths. M stars show scale factors compatible with zero CBS strength, while K dwarfs form a plateau at 23% solar strength CBS with a sharp step in-between. Above 4700 K, CBS scales with the third power of the effective temperature. It could be shown that CBS is anti-correlated with chromospheric activity, while no dependence on excitation potential could be found. Stars within the sample around the solar temperature fall below the expected scale factor of unity by about 5%, though a similar effect could be found in HARPS Sun-as-a-star observations, indicating that the solar FTS spectrum may have been recorded at a time of intrinsically higher solar CBS. Literature values of solar CCF BIS values support this, as they show intrinsic variations of roughly 10%, indicating a noise floor at this level. Further comparing the results to the literature showed good agreement with computational models, though analytical scaling relations seem to suffer from the assumption that the cancellation between intergranular redshift and granular blueshift is independent of spectral type. Discrepancies to empirical measurements of CBS strength by [Meunier et al. \(2017c\)](#) appear to be due to differences in the adopted third signature model, where a simplified, linear model underestimates the scaling of CBS for hotter stars due to the increasing curvature of the third signature.

4.3. Convection among evolved stars

Among the stars discarded from the sample in Section 2, as summarized in Section 4.2, were 241 evolved stars that otherwise met the criteria for a successful analysis, spanning the subgiant, red giant and asymptotic giant phases. The phases were determined by fitting synthetic photometric data from the MIST project to *Gaia* DR2 parameters, namely the effective temperature, luminosity and G, RP, and BP magnitudes. The grids further provided estimates for surface gravity and stellar mass. The technique employed was identical to the MS sample, excluding the refinement of the line list and instead using the final list from Section 4.2 and the calibrated template from 4.1. Scaling the template to the evolved stars spectra showed an up to 5 times increase in CBS strength for the coolest, most evolved stars in the sample, RG and AGB stars at 4000 K, while the least evolved subgiants are barely turning off the MS relation derived previously. Between those points CBS is nearly constant around solar strength with a small minimum around 5200 K and $\log g \sim 3.2$, corresponding to the transition between subgiants and red giants and matching a minimum in photometric granulation flicker previously observed in the literature. The results were compared to the literature (Gray 2009), again highlighting the need for a representative third signature model, this time due to a highly restricted choice of spectral lines causing a difference in scaling behavior rather than a simplified model. Analytic scaling relations for observed CBS again could not explain the entire range of scale factors within our sample, strongly deviating for the more evolved stars. As the deviation appeared smooth, a temperature dependent correction factor, accounting for the changes in surface granulation structure not caught by the analytical model, could be determined. Comparing the determined scale factors to macroturbulent dispersion and 3D MHD derived convection velocities revealed a similar picture. This is likely again due to changes in the balancing between granular and lane contributions, which could lead to an increase in velocity dispersion and macroturbulent broadening while the core shift decreases. During the investigation of the differences between the results of this work and the literature, a sample of PEPSI MS and post-MS spectra was investigated. The results agree with the HARPS sample within the margin of error, demonstrating that the choice of instrument has no effect on the results.

4.4. Using directly measured convective blueshift for activity mitigation

In this work, a highly robust and broadly applicable method to directly measure the strength of convective blueshift was developed. It was tested on ultra-high quality solar FTS data, coadded stellar spectra from the HARPS and PEPSI instruments and the HARPS-N Sun-as-a-star series of observations and has proven reliable in all cases. This section will go into details how this, together with the findings from Chapters 1.4.1 - 1.4.3, ties into the overarching goal of finding ways to mitigate the influence of stellar

variability on the detection of small exoplanets via the RV method. One potential path towards that is sketched, starting with the underlying theory before tying into the results of this work.

Stellar oscillations (Section 1.4.1) are simultaneously the most complicated to understand phenomenon and the one easiest to mitigate. Their narrow width in frequency space combined with the predictable scaling with stellar parameters means they can be mitigated simply by binning in time. This can be achieved either by carefully choosing the integration time on a star by star basis if a minimum of observing time is important, specifically matching to the stars' parameters (obtainable for example by asteroseismology), or a longer window that would be sufficient for a wider range of stars. The integration times required for most stars to achieve sufficient S/N already fall into the second category however. Alternatively, coadding successive observations to achieve sufficient total integration time is another option for bright or evolved stars (Chaplin et al. 2019).

The much wider range of the power spectrum of granulation (see Section 1.4.3) significantly lowers the efficacy of binning as a mitigation strategy. Meunier et al. (2015) show that even a full hour of integration is insufficient to decrease granulation rms below 40 cm s^{-1} for the Sun. When combined with oscillations, granulation provides a lower bound for the RV jitter that can be reached by binning within reasonable observational constraints (Dumusque et al. 2011) and effectively prevents the detection of Earth-twins unless more sophisticated methods to capture the momentary contribution from granular jitter are employed.

Similarly, the mitigation of the effect of rotational modulation of flux effects (Section 1.4.2) is more difficult than one may expect as the exact distribution of starspots is unknown, can not be recovered sufficiently and changes over time in unpredictable ways. This, like granulation, therefore requires proxies that correlate well with the momentary, activity driven velocity modulation but not any potential Keplerian variations and which can be measured simultaneous to the RV, ideally from the same data. One way is through concurrent photometry. The simplest approach would be to calculate periodograms for the lightcurve and the RV time series and compare the two. Any peak in the RV periodogram without an equivalent in the lightcurve would need to be due to non-stellar origins and could indicate an exoplanet. Removing common periodicities from the RV time series, called pre-whitening, should then result in an isolated, strengthened planetary signal. This approach has the problem that spot evolution leads to signals that are not strictly periodic, changing in amplitude and phase over time, whereas simple periodograms assume a time-constant sinusoidal signal. Removing such quasi periodic signals approximated as pure sinusoids would then introduce harmonics and potentially bias the genuine signal (Tuomi et al. 2014). A more sophisticated model, that correlates observations at the point in time they were made, rather than as an a posteriori ensemble, is the FF'-method (Aigrain et al. 2012). In this method, a high-precision lightcurve is used to model the RV variations caused by the flux effect using the brightness variations caused by the surface features rotating over the visible stellar disk. The name derives from the methods multiplication of the flux time series F , varying proportional with the fraction of the visible

disk covered by starspots, and its time derivative. This can be imagined as each individual starspot causing a sinusoidal variation in brightness that maximizes when its projected area is largest, i.e. when it crosses the disk center. The modulation of the rotational broadening, which is the core of the flux effect, however is largest while the spot crosses the limb of the star where the projected velocity is largest and thereby offset from the flux curve itself by 90 degrees. For sinusoids this is the equivalent of a derivative and the overall flux effect, depending on both the projected area and the magnitude of the covered velocity contribution, is proportional to the product FF' of the flux timeseries and its derivative. The model further allows for the inclusion of convective blueshift suppression since the areas contributing to the flux effect also cause the CBS suppression. Unlike rotation, CBS is observed strongest at the disk center where the full velocity is projected along the line of sight. As such the CBS term in the FF' framework is proportional to F^2 . The biggest limitation of this approach is that it implicitly tries to reconstruct the surface distribution of starspots, which was shown in Section 1.4.2 to be impossible for symmetric features. It also relies on the assumption that all RV variations have an observable, photometric counterpart that can be used as a proxy. [Meunier et al. \(2010\)](#) have shown that this is not true for plage regions. While they cover a much larger area compared to spots, thereby contributing more to the overall CBS suppression, their low contrast and opposite sign leaves them effectively invisible in photometry and gives the FF' method no way to recover their effect on the RV variations.

An expansion on the FF' framework that also avoids the complication of having to obtain simultaneous photometry in the first place was proposed by [Rajpaul et al. \(2015\)](#). They replaced the observed flux timeseries with a Gaussian process (GP) that is intended to represent the fraction of the surface that is covered in any magnetically active region instead of just the spot covering. They also expand the FF' formalism to include the chromospheric activity indicator $\log R'_{\text{HK}}$, allowing them to theoretically capture plage contributions to CBS suppression as proxy for the facular coverage, and the bisector inverse slope (BIS), a measure of the spectral line asymmetry that is sensitive to the flux and CBS contributions, as functions of the GP. Using GP regression with a quasi-periodic kernel on the three spectroscopic observables RV, $\log R'_{\text{HK}}$ and BIS, together with a Keplerian mean function, allowed them to recover a synthetic planetary signal from the model spectrum of a spotted, rotating star. The planetary period was equal to the rotation period but at a fifth the strength, an amplitude of only 28 cm s^{-1} , representing a worst-case. The stellar model used by [Rajpaul et al. \(2015\)](#) however did not actually contain facular regions, thereby not demonstrating if the GP is capable of correctly accounting for their contribution, and only incorporating four large, equatorial spots. In [Rajpaul et al. \(2021\)](#) they demonstrate their method on the Kepler-37 system and manage to detect Kepler-37d in RV at a semi-amplitude of 1.22 m s^{-1} , comparable to the precision of the instrument itself. Though still insufficient for an Earth-twin observation, they managed to demonstrate the feasibility of their approach in principle.

Results by [Haywood et al. \(2016\)](#) are casting doubts on whether the framework by [Rajpaul et al. \(2015\)](#) would be able to achieve similar success with an Earth-twin and an instrument that is stable at the 10 cm s^{-1} level however. Using SDO HMI magnetograms to accurately

model the solar surface and derive a synthetic RV time series together with HARPS observations of the solar spectrum reflected off of the asteroid Vesta they were able to constrain the level of correlation between activity indicators derived from the spectrum or the solar surface and the RV variability. While the RV derived from the magnetograms agreed well with the observed values, it was found that classical spectral indicators like $\log R'_{\text{HK}}$ and BIS are not very strongly correlated to the overall velocity variations (Spearman correlation coefficient < 0.4). From this it appears unlikely that these specific indicators would enable activity mitigation to the level of an Earth-twin and while [Haywood et al. \(2016\)](#) propose a much better indicator, the unsigned and disk integrated magnetic flux, they obtained this value from the spatially resolved magnetograms of the Sun. Since those are unobtainable for other stars at this point and modeling of Zeeman broadening is not very precise ([Petit et al. 2021](#) show an uncertainty of 15%), this also does not solve the problem of a better proxy for CBS suppression.

Instead of searching for a proxy to represent the variation of CBS, this work has instead shown a way to reliably determine the strength of CBS directly, without need for a proxy that only indirectly relates to the underlying process. One of the reasons the $\log R'_{\text{HK}}$ indicator does not work well is that it is sensitive to chromospheric activity, therefore plages, while CBS suppression is a photospheric effect affected by faculae. The two phenomena are linked as they are formed by the same magnetic field lines and sometimes even used interchangeably in the literature but in the end the two are not identical. As such, the CBS strength should correlate much better with overall RV variations while still being a spectroscopic indicator, therefore not requiring additional observations or instrumentation. While the technique has only been attempted for solar time series and coadded stellar templates so far, the analysis of the limits of the technique indicates it should also work under the lower S/N from stellar time series except for the fainter stars.

4.5. Outlook

A couple of additional steps are still required in order to evaluate the worth of the CBS strength in velocity variability mitigation. While the methods robustness could be shown in this work for large numbers of coadditions, both in numbers of stars and spectra per star, application on spectral time series is limited to HARPS Sun-as-a-star data with correspondingly high S/N for now. A thorough verification process, similar to [Haywood et al. \(2016\)](#), needs to still be performed with the HARPS solar data at the core as well as synthetic modeling following the idea of [Rajpaul et al. \(2015\)](#) but employing a more sophisticated stellar model that does not forego plage/faculae contributions and allows for realistic active region distributions. Ideally, the underlying spectroscopic models would be based on 3D magneto-hydrodynamic models of stellar photospheres in order to have perfect control over all parameters, especially the effects of limb angle. This route would further allow for the resolution of the question why evolved stars appear to decouple in line core shift and more traditional CBS proxies. Alternatively, spatially resolved solar

observations could be used as basis spectra for the integrated model, although this would restrict the testable parameter space, rely on all possible surface features being observable on the Sun and require a very large amount of observations.

Bibliography

- AIGRAIN, S., PONT, F. & ZUCKER, S. (2012) A simple method to estimate radial velocity variations due to stellar activity using photometry. *MNRAS*, **419**(4), 3147–3158.
- ALLENDE PRIETO, C. & GARCIA LOPEZ, R. J. (1998) Fe i line shifts in the optical spectrum of the Sun. *A&AS*, **129**, 41–44.
- ANGLADA-ESCUDE, G. & BUTLER, R. P. (2012) The HARPS-TERRA Project. I. Description of the Algorithms, Performance, and New Measurements on a Few Remarkable Stars Observed by HARPS. *ApJS*, **200**(2), 15.
- ASTROPY COLLABORATION, PRICE-WHELAN, A. M., SIPŐCZ, B. M. ET AL. (2018) The Astropy Project: Building an Open-science Project and Status of the v2.0 Core Package. *AJ*, **156**(3), 123.
- ASTROPY COLLABORATION, ROBITAILLE, T. P., TOLLERUD, E. J. ET AL. (2013) Astropy: A community Python package for astronomy. *A&A*, **558**, A33.
- BARANNE, A., QUELOZ, D., MAYOR, M. ET AL. (1996) ELODIE: A spectrograph for accurate radial velocity measurements. *A&AS*, **119**, 373–390.
- BARNES, J. R., JEFFERS, S. V., JONES, H. R. A. ET AL. (2015) Starspot Distributions on Fully Convective M Dwarfs: Implications for Radial Velocity Planet Searches. *ApJ*, **812**(1), 42.
- BAROCH, D., MORALES, J. C., RIBAS, I. ET AL. (2020) The CARMENES search for exoplanets around M dwarfs. Convective shift and starspot constraints from chromatic radial velocities. *A&A*, **641**, A69.
- BASTIEN, F. A., STASSUN, K. G., BASRI, G. & PEPPER, J. (2013) An observational correlation between stellar brightness variations and surface gravity. *Nature*, **500**(7463), 427–430.
- BASU, S. & CHAPLIN, W. J. (2017) *Asteroseismic Data Analysis - Foundations and Techniques*. Princeton University Press.
- BATYGIN, K. & STEVENSON, D. J. (2010) Inflating Hot Jupiters with Ohmic Dissipation. *ApJ*, **714**(2), L238–L243.
- BAUER, F. F., REINERS, A., BEECK, B. & JEFFERS, S. V. (2018) The influence of convective blueshift on radial velocities of F, G, and K stars. *A&A*, **610**, A52.

- BEECK, B., CAMERON, R. H., REINERS, A. & SCHÜSSLER, M. (2013a) Three-dimensional simulations of near-surface convection in main-sequence stars. I. Overall structure. *A&A*, **558**, A48.
- BEECK, B., CAMERON, R. H., REINERS, A. & SCHÜSSLER, M. (2013b) Three-dimensional simulations of near-surface convection in main-sequence stars. II. Properties of granulation and spectral lines. *A&A*, **558**, A49.
- BERDYUGINA, S. V. (2005) Starspots: A Key to the Stellar Dynamo. *Living Reviews in Solar Physics*, **2**(1), 8.
- BERTAUX, J. L., LALLEMENT, R., FERRON, S., BOONNE, C. & BODICHON, R. (2014) TAPAS, a web-based service of atmospheric transmission computation for astronomy. *A&A*, **564**, A46.
- BOGDAN, T. J., GILMAN, P. A., LERCHE, I. & HOWARD, R. (1988) Distribution of Sunspot Umbral Areas: 1917–1982. *ApJ*, **327**, 451.
- BORO SAIKIA, S., MARVIN, C. J., JEFFERS, S. V. ET AL. (2018) Chromospheric activity catalogue of 4454 cool stars. Questioning the active branch of stellar activity cycles. *A&A*, **616**, A108.
- BOWLER, B. P., JOHNSON, J. A., MARCY, G. W. ET AL. (2010) Retired A Stars and Their Companions. III. Comparing the Mass-Period Distributions of Planets Around A-Type Stars and Sun-Like Stars. *ApJ*, **709**(1), 396–410.
- BRAHM, R., JORDÁN, A. & ESPINOZA, N. (2017) CERES: A Set of Automated Routines for Echelle Spectra. *PASP*, **129**(973), 034002.
- BRESSAN, A., MARIGO, P., GIRARDI, L. ET AL. (2012) PARSEC: stellar tracks and isochrones with the PAdova and TRieste Stellar Evolution Code. *MNRAS*, **427**(1), 127–145.
- CARDIEL, N. (2009) Data boundary fitting using a generalized least-squares method. *MNRAS*, **396**, 680–695.
- CARROLL, B. W. & OSTLIE, D. A. (2014) *An introduction to modern astrophysics*. Pearson.
- CEGLA, H. M., WATSON, C. A., SHELİYAG, S., MATHIOUDAKIS, M. & MOUTARI, S. (2019) Stellar Surface Magnetoconvection as a Source of Astrophysical Noise. III. Sun-as-a-Star Simulations and Optimal Noise Diagnostics. *ApJ*, **879**(1), 55.
- CHAPLIN, W. J., CEGLA, H. M., WATSON, C. A., DAVIES, G. R. & BALL, W. H. (2019) Filtering Solar-Like Oscillations for Exoplanet Detection in Radial Velocity Observations. *AJ*, **157**(4), 163.
- CHAPMAN, G. A. & MEYER, A. D. (1981) Observations of the wavelength dependence of the average contrast of sunspots. In *The Physics of Sunspots*, edited by L. E. Cram & J. H. Thomas.

- CHIAVASSA, A., CASAGRANDE, L., COLLET, R. ET AL. (2018) The STAGGER-grid: A grid of 3D stellar atmosphere models. V. Synthetic stellar spectra and broad-band photometry. *A&A*, **611**, A11.
- CHOI, J., DOTTER, A., CONROY, C. ET AL. (2016) Mesa Isochrones and Stellar Tracks (MIST). I. Solar-scaled Models. *ApJ*, **823**(2), 102.
- CHRISTENSEN-DALSGAARD, J. (2002) Helioseismology. *Reviews of Modern Physics*, **74**(4), 1073–1129.
- CIDDOR, P. E. (1996) Refractive index of air: new equations for the visible and near infrared. *Appl. Opt.*, **35**, 1566.
- CLARET, A. & BLOEMEN, S. (2011) Gravity and limb-darkening coefficients for the Kepler, CoRoT, Spitzer, uvby, UBVRIJHK, and Sloan photometric systems. *A&A*, **529**, A75.
- COLLIER CAMERON, A. (1997) Eclipse mapping of late-type close binary stars. *MNRAS*, **287**(3), 556–566.
- COLLIER CAMERON, A., MORTIER, A., PHILLIPS, D. ET AL. (2019) Three years of Sun-as-a-star radial-velocity observations on the approach to solar minimum. *MNRAS*, **487**(1), 1082–1100.
- COVEY, K. R., IVEZIĆ, Ž., SCHLEGEL, D. ET AL. (2007) Stellar SEDs from 0.3 to 2.5 μm : Tracing the Stellar Locus and Searching for Color Outliers in the SDSS and 2MASS. *AJ*, **134**(6), 2398–2417.
- CRETIGNIER, M., DUMUSQUE, X., ALLART, R., PEPE, F. & LOVIS, C. (2020) Measuring precise radial velocities on individual spectral lines. II. Dependence of stellar activity signal on line depth. *A&A*, **633**, A76.
- CZESLA, S., SCHRÖTER, S., SCHNEIDER, C. P. ET AL. (2019) PyA: Python astronomy-related packages.
- DEMIRCAN, O. & KAHRAMAN, G. (1991) Stellar Mass / Luminosity and Mass / Radius Relations. *Ap&SS*, **181**(2), 313–322.
- DÖLLINGER, M. P. & HARTMANN, M. (2021) A Sanity Check for Planets around Evolved Stars. *ApJS*, **256**(1), 10.
- DOTTER, A. (2016) MESA Isochrones and Stellar Tracks (MIST) 0: Methods for the Construction of Stellar Isochrones. *ApJS*, **222**(1), 8.
- DOYLE, A. P., DAVIES, G. R., SMALLEY, B., CHAPLIN, W. J. & ELSWORTH, Y. (2014) Determining stellar macroturbulence using asteroseismic rotational velocities from Kepler. *MNRAS*, **444**(4), 3592–3602.
- DRAVINS, D. (1987) Stellar granulation. I - The observability of stellar photospheric convection. *A&A*, **172**, 200–224.

- DRAVINS, D., LARSSON, B. & NORDLUND, A. (1986) Solar Fe II line asymmetries and wavelength shifts. *A&A*, **158**, 83–88.
- DRAVINS, D., LINDEGREN, L. & NORDLUND, A. (1981) Solar granulation - Influence of convection on spectral line asymmetries and wavelength shifts. *A&A*, **96**, 345–364.
- DUMUSQUE, X., CRETIGNIER, M., SOSNOWSKA, D. ET AL. (2021) Three years of HARPS-N high-resolution spectroscopy and precise radial velocity data for the Sun. *A&A*, **648**, A103.
- DUMUSQUE, X., UDRY, S., LOVIS, C., SANTOS, N. C. & MONTEIRO, M. J. P. F. G. (2011) Planetary detection limits taking into account stellar noise. I. Observational strategies to reduce stellar oscillation and granulation effects. *A&A*, **525**, A140.
- EASTMAN, J., GAUDI, B. S. & AGOL, E. (2013) EXOFAST: A Fast Exoplanetary Fitting Suite in IDL. *PASP*, **125**(923), 83.
- EINSTEIN, A. (1915) Zur allgemeinen Relativitätstheorie. *Sitzungsberichte der Königlich Preussischen Akademie der Wissenschaften (Berlin)*, 778–786.
- FIGUEIRA, P., ADIBEKYAN, V. Z., OSHAGH, M. ET AL. (2016) Radial velocity information content of M dwarf spectra in the near-infrared. *A&A*, **586**, A101.
- FRIEDMANN, A. (1922) Über die Krümmung des Raumes. *Zeitschrift für Physik*, **10**, 377–386.
- GAIA COLLABORATION (2018) VizieR Online Data Catalog: Gaia DR2 (Gaia Collaboration, 2018). *VizieR Online Data Catalog*, I/345.
- GINSBURG, A., SIPÓCZ, B. M., BRASSEUR, C. E. ET AL. (2019) astroquery: An Astronomical Web-querying Package in Python. *AJ*, **157**, 98.
- GLEBOCKI, R. & GNACINSKI, P. (2005) VizieR Online Data Catalog: Catalog of Stellar Rotational Velocities (Glebocki+ 2005). *VizieR Online Data Catalog*, III/244.
- GRAY, D. F. (1982) Observations of spectral line asymmetries and convective velocities in F, G and K stars. *ApJ*, **255**, 200–209.
- GRAY, D. F. (2009) The Third Signature of Stellar Granulation. *ApJ*, **697**, 1032–1043.
- GRAY, D. F. (2010a) An Explanation of Reversed Spectral-line Bisectors. *ApJ*, **721**(1), 670–674.
- GRAY, D. F. (2010b) Empirical Decoding of the Shapes of Spectral-Line Bisectors. *ApJ*, **710**(2), 1003–1008.
- GRAY, D. F. (2021) *The Observation and Analysis of Stellar Photospheres*. 4th edn., Cambridge University Press.

- GRAY, D. F. & NAGEL, T. (1989) The granulation boundary in the H-R diagram. *ApJ*, **341**, 421–426.
- GRAY, D. F. & OOSTRA, B. (2018) The Solar-flux Third Granulation Signature. *ApJ*, **852**, 42.
- GRAY, D. F. & PUGH, T. (2012) The Third Signature of Granulation in Bright-giant and Supergiant Stars. *AJ*, **143**, 92.
- GRUNBLATT, S. K., HUBER, D., GAIDOS, E. ET AL. (2017) Seeing Double with K2: Testing Re-inflation with Two Remarkably Similar Planets around Red Giant Branch Stars. *AJ*, **154**(6), 254.
- GRUNBLATT, S. K., HUBER, D., GAIDOS, E. ET AL. (2018) Do Close-in Giant Planets Orbiting Evolved Stars Prefer Eccentric Orbits? *ApJ*, **861**(1), L5.
- HAMILTON, D. & LESTER, J. B. (1999) A Technique for the Study of Stellar Convection: The Visible Solar Flux Spectrum. *PASP*, **111**, 1132–1143.
- HARRIS, C. R., MILLMAN, K. J., VAN DER WALT, S. J. ET AL. (2020) Array programming with NumPy. *Nature*, **585**(7825), 357–362, URL <https://doi.org/10.1038/s41586-020-2649-2>.
- HAYWOOD, R. D., COLLIER CAMERON, A., UNRUH, Y. C. ET AL. (2016) The Sun as a planet-host star: proxies from SDO images for HARPS radial-velocity variations. *MNRAS*, **457**(4), 3637–3651.
- HEKKER, S. & CHRISTENSEN-DALSGAARD, J. (2017) Giant star seismology. *A&A Rev.*, **25**(1), 1.
- HERRERO, E., RIBAS, I., JORDI, C. ET AL. (2016) Modelling the photosphere of active stars for planet detection and characterization. *A&A*, **586**, A131.
- HUBBLE, E. (1929) A Relation between Distance and Radial Velocity among Extra-Galactic Nebulae. *Proceedings of the National Academy of Science*, **15**(3), 168–173.
- HUBBLE, E. P. (1925) Cepheids in Spiral Nebulae. *Popular Astronomy*, **33**, 252–255.
- HUBER, D., BEDDING, T. R., STELLO, D. ET AL. (2011) Testing Scaling Relations for Solar-like Oscillations from the Main Sequence to Red Giants Using Kepler Data. *ApJ*, **743**(2), 143.
- HUNTER, J. D. (2007) Matplotlib: A 2D graphics environment. *Computing in Science & Engineering*, **9**(3), 90–95.
- HUSSER, T.-O., KAMANN, S., DREIZLER, S. ET AL. (2016) MUSE crowded field 3D spectroscopy of over 12 000 stars in the globular cluster NGC 6397. I. The first comprehensive HRD of a globular cluster. *A&A*, **588**, A148.

- HUSSER, T.-O., WENDE-VON BERG, S., DREIZLER, S. ET AL. (2013) A new extensive library of PHOENIX stellar atmospheres and synthetic spectra. *A&A*, **553**, A6.
- JEFFERS, S. V., BARNES, J. R., JONES, H. R. A. ET AL. (2014) Is it possible to detect planets around young active G and K dwarfs? *MNRAS*, **438**(4), 2717–2731.
- JURGENSON, C., FISCHER, D., MCCracken, T. ET AL. (2016) EXPRES: a next generation RV spectrograph in the search for earth-like worlds. In *Ground-based and Airborne Instrumentation for Astronomy VI*, vol. 9908 of *Society of Photo-Optical Instrumentation Engineers (SPIE) Conference Series*.
- KJELDSSEN, H. & BEDDING, T. R. (1995) Amplitudes of stellar oscillations: the implications for asteroseismology. *A&A*, **293**, 87–106.
- KJELDSSEN, H. & BEDDING, T. R. (2011) Amplitudes of solar-like oscillations: a new scaling relation. *A&A*, **529**, L8.
- KJELDSSEN, H., BEDDING, T. R., ARENTOFT, T. ET AL. (2008) The Amplitude of Solar Oscillations Using Stellar Techniques. *ApJ*, **682**(2), 1370–1375.
- KREIDBERG, L. (2018) Exoplanet Atmosphere Measurements from Transmission Spectroscopy and Other Planet Star Combined Light Observations. In *Handbook of Exoplanets*, edited by H. J. Deeg & J. A. Belmonte, p. 100.
- KUPKA, F. G., RYABCHIKOVA, T. A., PISKUNOV, N. E., STEMPELS, H. C. & WEISS, W. W. (2000) VALD-2 – The New Vienna Atomic Line Database. *Baltic Astronomy*, **9**, 590–594.
- KÜRSTER, M., ENDL, M., ROUESNEL, F. ET AL. (2003) The low-level radial velocity variability in Barnard’s star (= GJ 699). Secular acceleration, indications for convective redshift, and planet mass limits. *A&A*, **403**, 1077–1087.
- LEMAÎTRE, G. (1927) Un Univers homogène de masse constante et de rayon croissant rendant compte de la vitesse radiale des nébuleuses extra-galactiques. *Annales de la Sociéte; Scientifique de Bruxelles*, **47**, 49–59.
- LIEBING, F., JEFFERS, S. V., REINERS, A. & ZECHMEISTER, M. (2021) Convective blueshift strengths of 810 F to M solar-type stars. *A&A*, **654**, A168.
- LLOYD, J. P. (2013) The Mass Distribution of Subgiant Planet Hosts. *ApJ*, **774**(1), L2.
- LOPEZ, E. D. & FORTNEY, J. J. (2016) Re-inflated Warm Jupiters around Red Giants. *ApJ*, **818**(1), 4.
- LOVIS, C., DUMUSQUE, X., SANTOS, N. C. ET AL. (2011) The HARPS search for southern extra-solar planets. XXXI. Magnetic activity cycles in solar-type stars: statistics and impact on precise radial velocities. *arXiv e-prints*, arXiv:1107.5325.
- LUDWIG, H. G., ALLARD, F. & HAUSCHILDT, P. H. (2002) Numerical simulations of surface convection in a late M-dwarf. *A&A*, **395**, 99–115.

- LUGER, R., AGOL, E., FOREMAN-MACKEY, D. ET AL. (2019) starry: Analytic Occultation Light Curves. *AJ*, **157**(2), 64.
- LUHN, J. K., WRIGHT, J. T., HOWARD, A. W. & ISAACSON, H. (2020) Astrophysical Insights into Radial Velocity Jitter from an Analysis of 600 Planet-search Stars. *AJ*, **159**(5), 235.
- MAGIC, Z. & ASPLUND, M. (2014) The Stagger-grid: A grid of 3D stellar atmosphere models - VI. Surface appearance of stellar granulation. *arXiv e-prints*, arXiv:1405.7628.
- MAGIC, Z., COLLET, R., ASPLUND, M. ET AL. (2013) The Stagger-grid: A grid of 3D stellar atmosphere models. I. Methods and general properties. *A&A*, **557**, A26.
- MARCONI, A., DI MARCANTONIO, P., D'ODORICO, V. ET AL. (2016) EELT-HIRES the high-resolution spectrograph for the E-ELT. In *Ground-based and Airborne Instrumentation for Astronomy VI*, vol. 9908 of *Society of Photo-Optical Instrumentation Engineers (SPIE) Conference Series*.
- MARVIN, C. J., REINERS, A., ANGLADA-ESCUDE, G., JEFFERS, S. V. & BORO SAIKIA, S. (2016, submitted) Absolute Ca II H & K and H Alpha flux measurements of low-mass stars: extending R'_{HK} to M dwarfs. *A&A*.
- MATHUR, S., HEKKER, S., TRAMPEDACH, R. ET AL. (2011) Granulation in Red Giants: Observations by the Kepler Mission and Three-dimensional Convection Simulations. *ApJ*, **741**(2), 119.
- MAYOR, M., PEPE, F., QUELOZ, D. ET AL. (2003) Setting New Standards with HARPS. *The Messenger*, **114**, 20–24.
- MAYOR, M. & QUELOZ, D. (1995) A Jupiter-mass companion to a solar-type star. *Nature*, **378**(6555), 355–359.
- MEUNIER, N., DESORT, M. & LAGRANGE, A. M. (2010) Using the Sun to estimate Earth-like planets detection capabilities . II. Impact of plagues. *A&A*, **512**, A39.
- MEUNIER, N., LAGRANGE, A.-M. & BORGNIET, S. (2017a) A new method of correcting radial velocity time series for inhomogeneous convection. *A&A*, **607**, A6.
- MEUNIER, N., LAGRANGE, A. M., BORGNIET, S. & RIEUTORD, M. (2015) Using the Sun to estimate Earth-like planet detection capabilities. VI. Simulation of granulation and supergranulation radial velocity and photometric time series. *A&A*, **583**, A118.
- MEUNIER, N., LAGRANGE, A.-M., MBEMBA KABUIKU, L. ET AL. (2017b) Variability of stellar granulation and convective blueshift with spectral type and magnetic activity. I. K and G main sequence stars. *A&A*, **597**, A52.
- MEUNIER, N., MIGNON, L. & LAGRANGE, A.-M. (2017c) Variability in stellar granulation and convective blueshift with spectral type and magnetic activity . II. From young to old main-sequence K-G-F stars. *A&A*, **607**, A124.

- MIKLOS, M., MILBOURNE, T. W., HAYWOOD, R. D. ET AL. (2020) Testing the Spectroscopic Extraction of Suppression of Convective Blueshift. *ApJ*, **888**(2), 117.
- MORRIS, B. M., BOBRA, M. G., AGOL, E., LEE, Y. J. & HAWLEY, S. L. (2020) The stellar variability noise floor for transiting exoplanet photometry with PLATO. *MNRAS*, **493**(4), 5489–5498.
- NAVE, G., JOHANSSON, S., LEARNER, R. C. M., THORNE, A. P. & BRAULT, J. W. (1994) A new multiplet table for Fe I. *ApJS*, **94**, 221–459.
- PALADINI, C., BARON, F., JORISSEN, A. ET AL. (2018) Large granulation cells on the surface of the giant star π^1 Gruis. *Nature*, **553**(7688), 310–312.
- PANJA, M., CAMERON, R. & SOLANKI, S. K. (2020) 3D Radiative MHD Simulations of Starspots. *ApJ*, **893**(2), 113.
- PAXTON, B., BILDSTEN, L., DOTTER, A. ET AL. (2011) Modules for Experiments in Stellar Astrophysics (MESA). *ApJS*, **192**(1), 3.
- PAXTON, B., CANTIello, M., ARRAS, P. ET AL. (2013) Modules for Experiments in Stellar Astrophysics (MESA): Planets, Oscillations, Rotation, and Massive Stars. *ApJS*, **208**(1), 4.
- PAXTON, B., MARCHANT, P., SCHWAB, J. ET AL. (2015) Modules for Experiments in Stellar Astrophysics (MESA): Binaries, Pulsations, and Explosions. *ApJS*, **220**(1), 15.
- PENZIAS, A. A. & WILSON, R. W. (1965) A Measurement of Excess Antenna Temperature at 4080 Mc/s. *ApJ*, **142**, 419–421.
- PEPE, F. A., CRISTIANI, S., REBOLO LOPEZ, R. ET AL. (2010) ESPRESSO: the Echelle spectrograph for rocky exoplanets and stable spectroscopic observations. In *Ground-based and Airborne Instrumentation for Astronomy III*, vol. 7735 of *Proc. SPIE*.
- PETIT, P., FOLSOM, C. P., DONATI, J. F. ET AL. (2021) Multi-instrumental view of magnetic fields and activity of ϵ Eridani with SPIRou, NARVAL, and TESS. *A&A*, **648**, A55.
- PISKUNOV, N. E., KUPKA, F., RYABCHIKOVA, T. A., WEISS, W. W. & JEFFERY, C. S. (1995) VALD: The Vienna Atomic Line Data Base. *A&AS*, **112**, 525.
- QUELOZ, D., HENRY, G. W., SIVAN, J. P. ET AL. (2001) No planet for HD 166435. *A&A*, **379**, 279–287.
- QUIRRENBACH, A., AMADO, P. J., CABALLERO, J. A. ET AL. (2016) CARMENES: an overview six months after first light. In *Ground-based and Airborne Instrumentation for Astronomy VI*, edited by C. J. Evans, L. Simard & H. Takami, vol. 9908 of *Society of Photo-Optical Instrumentation Engineers (SPIE) Conference Series*.

- RAJPAUL, V., AIGRAIN, S., OSBORNE, M. A., REECE, S. & ROBERTS, S. (2015) A Gaussian process framework for modelling stellar activity signals in radial velocity data. *MNRAS*, **452**(3), 2269–2291.
- RAJPAUL, V. M., BUCHHAVE, L. A., LACEDELLI, G. ET AL. (2021) A HARPS-N mass for the elusive Kepler-37d: a case study in disentangling stellar activity and planetary signals. *MNRAS*, **507**(2), 1847–1868.
- REINERS, A., MROTZEK, N., LEMKE, U., HINRICHS, J. & REINSCH, K. (2016) The IAG solar flux atlas: Accurate wavelengths and absolute convective blueshift in standard solar spectra. *A&A*, **587**, A65.
- RYABCHIKOVA, T., PISKUNOV, N., KURUCZ, R. L. ET AL. (2015) A major upgrade of the VALD database. *Phys. Scr*, **90**(5), 054005.
- SANTRICH, O. J. K., PEREIRA, C. B. & DRAKE, N. A. (2013) Chemical analysis of giant stars in the young open cluster NGC 3114. *A&A*, **554**, A2.
- SAUNDERS, N., GRUNBLATT, S. K., HUBER, D. ET AL. (2022) TESS Giants Transiting Giants. I.: A Noninflated Hot Jupiter Orbiting a Massive Subgiant. *AJ*, **163**(2), 53.
- SCHWARZSCHILD, M. (1975) On the scale of photospheric convection in red giants and supergiants. *ApJ*, **195**, 137–144.
- SILSO WORLD DATA CENTER (2014-2018) The International Sunspot Number. *International Sunspot Number Monthly Bulletin and online catalogue*.
- SKILLING, J. & BRYAN, R. K. (1984) Maximum Entropy Image Reconstruction - General Algorithm. *MNRAS*, **211**, 111.
- SOLANKI, S. K. (1999) Spots and Plages: the Solar Perspective. In *Solar and Stellar Activity: Similarities and Differences*, edited by C. J. Butler & J. G. Doyle, vol. 158 of *Astronomical Society of the Pacific Conference Series*.
- SOLANKI, S. K. (2003) Sunspots: An overview. *A&A Rev.*, **11**(2-3), 153–286.
- SOLANKI, S. K. & UNRUH, Y. C. (2004) Spot sizes on Sun-like stars. *MNRAS*, **348**(1), 307–315.
- STRASSMEIER, K. G., ILYIN, I., JÄRVINEN, A. ET AL. (2015) PEPSI: The high-resolution échelle spectrograph and polarimeter for the Large Binocular Telescope. *Astronomische Nachrichten*, **336**(4), 324.
- STRASSMEIER, K. G., ILYIN, I. & WEBER, M. (2018) PEPSI deep spectra. II. Gaia benchmark stars and other M-K standards. *A&A*, **612**, A45.
- TAKARADA, T., SATO, B., OMIYA, M. ET AL. (2018) Planets around the evolved stars 24 Boötis and γ Libra: A 30 d-period planet and a double giant-planet system in possible 7:3 MMR. *PASJ*, **70**(4), 59.

- TOPKA, K. P., TARBELL, T. D. & TITLE, A. M. (1997) Properties of the Smallest Solar Magnetic Elements. II. Observations versus Hot Wall Models of Faculae. *ApJ*, **484**(1), 479–486.
- TOUT, C. A., POLS, O. R., EGGLETON, P. P. & HAN, Z. (1996) Zero-age main-sequence radii and luminosities as analytic functions of mass and metallicity. *MNRAS*, **281**(1), 257–262.
- TRAMPEDACH, R., ASPLUND, M., COLLET, R., NORDLUND, Å. & STEIN, R. F. (2013) A Grid of Three-dimensional Stellar Atmosphere Models of Solar Metallicity. I. General Properties, Granulation, and Atmospheric Expansion. *ApJ*, **769**(1), 18.
- TRIFONOV, T., TAL-OR, L., ZECHMEISTER, M. ET AL. (2020) Public HARPS radial velocity database corrected for systematic errors. *A&A*, **636**, A74.
- TUOMI, M., ANGLADA-ESCUDE, G., JENKINS, J. S. & JONES, H. R. A. (2014) Filtering out activity-related variations from radial velocities in a search for low-mass planets. *arXiv e-prints*, arXiv:1405.2016.
- VAN ROSSUM, G. & DRAKE, F. L. (2009) *Python 3 Reference Manual*. CreateSpace, Scotts Valley, CA.
- VILLAVER, E. & LIVIO, M. (2009) The Orbital Evolution of Gas Giant Planets Around Giant Stars. *ApJ*, **705**(1), L81–L85.
- VIRTANEN, P., GOMMERS, R., OLIPHANT, T. E. ET AL. (2020) SciPy 1.0: Fundamental Algorithms for Scientific Computing in Python. *Nature Methods*, **17**, 261–272.
- WINN, J. N. (2010) Transits and Occultations. *arXiv e-prints*, arXiv:1001.2010.
- WOLSZCZAN, A. & FRAIL, D. A. (1992) A planetary system around the millisecond pulsar PSR1257 + 12. *Nature*, **355**(6356), 145–147.
- ZECHMEISTER, M., REINERS, A., AMADO, P. J. ET AL. (2018) Spectrum radial velocity analyser (SERVAL). High-precision radial velocities and two alternative spectral indicators. *A&A*, **609**, A12.

Acknowledgements

I want to thank everyone who has supported me in one way or another over the course of my PhD. Without all of you this thesis would not have been possible.

Many thanks to Stefan for keeping an open ear and staying reassuring when things got tough, going back all the way to the days of my Bachelor thesis. My thanks also go to Ansgar and Sandra, first for giving me the chance at this project in the first place and for staying supportive throughout it all, especially during the years of the pandemic. Special thanks to Sandra for always encouraging me to persevere and stay my course, pushing me to do my best whenever necessary and staying in contact as an invaluable advisor even after she was no longer officially part of the TAC. On a similar note, I thank Mathias for volunteering on short notice as a replacement TAC member, lending his insights wherever possible and helping to translate what passes as orthography for me into legibility. Massive thanks to all of you for all the time you invested having discussions with me, both complicated and mundane, and checking over what felt like a never ending avalanche of paper drafts to point out improvements and streamline my tendency towards overly flowery sentences.

I would also like to thank my family, particularly my parents, for their support throughout all my studies, Bachelor, Master, and PhD, for keeping me sane throughout the isolation from the pandemic and for always believing that I could eventually reach this point.

This project was funded by the German Research Foundation (DFG) through the priority program SPP 1992 "Exploring the Diversity of Extrasolar Planets (RE 1664/18).

Curriculum vitae

Florian Liebing, M.Sc.
Gesundbrunnen 6a, 37079 Göttingen
florian.liebing@uni-goettingen.de

Date of Birth: 21.09.1994
Place of Birth: Seesen, Germany
Nationality: German

Education

10/2018 - 05/2022	PhD , Astrophysics (Georg-August University of Göttingen) Thesis: <i>How does stellar convection impact the detection of small planets at high radial velocity precision?</i>
10/2016 - 08/2018	M.Sc. , Physics (Georg-August University of Göttingen) Thesis: <i>Simulation and detection limits of reflected starlight with CARMENES</i>
10/2013 - 09/2016	B.Sc. , Physics (Georg-August University of Göttingen) Thesis: <i>Automated search for emission line objects in MUSE datacubes</i>
06/2013	Abitur , (Max-Planck Gymnasium Göttingen)

Publications

First Author:

1. **Liebing, F.**, Jeffers, S. V., Reiners, A., Zechmeister, M. "Convective blueshift strengths of 810 F to M solar-type stars" *Astronomy and Astrophysics*, vol. 654, 2021. doi:10.1051/0004-6361/202039607.

Co-Author:

1. Beuermann, K., Breitenstein, P., Debski, B., Diese, J., Dubovsky, P. A., Dreizler, S., Hessman, F. V., Hornoch, K., Husser, T. -O., Pojmanski, G., Wolf, M., Woźniak, P. R., Zasche, P., Denk, B., Langer, M., Wagner, C., Wahrenberg, D., Bollmann, T., Habermann,

F. N., Haustovich, N., Lauser, M., **Liebing, F.**, Niederstadt, F. “The quest for companions to post-common envelope binaries. II. NSVS14256825 and HS0705+6700”, *Astronomy and Astrophysics*, vol. 540, 2012. doi:10.1051/0004-6361/201118105.

2. Backhaus, U., Bauer, S., Beuermann, K., Diese, J., Dreizler, S., Hessman, F. V., Husser, T. -O., Klapdohr, K. -H., Möllmanns, J., Schönecke, R., Dette, J., Dubbert, J., Miosga, T., Rochus Vogel, A. L., Simons, S., Biriuk, S., Debrah, M., Griemens, M., Hahn, A., Möller, T., Pawlowski, M., Schweizer, M., Speck, A. -L., Zapros, C., Bollmann, T., Habermann, F. N., Haustovich, N., Lauser, M., **Liebing, F.**, Niederstadt, F., Hoppen, K., Kindermann, D., Küppers, F., Rauch, B., Althoff, F., Horstmann, M., Kellerman, J. N., Kietz, R., Nienaber, T., Sauer, M., Secci, A., Wüllner, L. “The quest for companions to post-common envelope binaries. I. Searching a sample of stars from the CSS and SDSS”, *Astronomy and Astrophysics*, vol. 538, 2012. doi:10.1051/0004-6361/201118104.